Micro/Nanoscale Modeling of Anisotropic Mechanical Properties of Polymer/Layered-Silicate Nanocomposites

by

Nuo Sheng

B.S., Tsinghua University, China (1995)

Submitted to the Department of Mechanical Engineering
In partial fulfillment of the requirements for the degree of

Master of Science in Mechanical Engineering

at the

MASSUCHUSETTS INSTITUTE OF TECHNOLOGY

August 2002
[September 2002]

Author .....
Department of Mechanical Engineering
August 9, 2002

Certified by .....
Mary C. Boyce
Professor of Mechanical Engineering
Thesis Supervisor

Certified by .....
David M. Parks
Professor of Mechanical Engineering
Thesis Supervisor

Accepted by .....
Ain A. Sonin
Chairman, Departmental Committee on Graduate Students

Micro/Nanoscale Modeling of Anisotropic Mechanical Properties of Polymer/Layered-Silicate Nanocomposites

by

Nuo Sheng

Submitted to the Department of Mechanical Engineering
on August 9, 2002, in partial fulfillment of the
requirements for the degree of
Master of Science in Mechanical Engineering

Abstract

Polymer nano-clay composites have been observed to exhibit dramatic enhancements in mechanical properties with relatively low filler loadings (1-4 percent volume fraction). These property enhancements have been speculated to be a result of the change in polymer morphology and properties within the polymer/particle interfacial regions, due to the nanometer length scale and the large interface area/unit volume of the nano-particles. In this work, the potential contribution of composite-level effects on the observed enhancements is explored. Two-dimensional models of various representative volume elements (RVEs) of the underlying structure of the polymer nano-clay composite are constructed. These models are characterized by clay particle volume fraction and micro/nano scale morphological features such as clay particle aspect ratio (length/thickness, L/t), clay particle distribution (random vs. regular patterns) and clay particle orientation distribution. Macroscopic moduli of these RVEs are predicted as a function of these geometrical parameters as well as particle and matrix stiffness parameters through FEM simulations. Effective properties of intercalated clay particles have been estimated in terms of characteristic clay structural parameters (interlayer spacing and number of layers), with additional information from molecular dynamics simulations of silicate layer stiffness. The predictions of macroscopic stiffness from these two-dimensional micromechanical models, based on structure-dependent particle volume fraction and properties, are consistent with experimental observations. Furthermore, studies of the local stress/strain fields show that the stiffness enhancement comes through the efficient load transfer mechanism in the high aspect ratio fillers, modulated by the strain shielding effect in the matrix. These results suggest that physically-based composite level interpretations may explain the stiffness enhancement mechanism of polymer nanocomposites to a large degree. The adopted methodology offers promise for study of related properties in polymer/layered-silicate nanocomposites.

Thesis Supervisor: Mary C. Boyce

Tile: Professor of Mechanical Engineering

Thesis Supervisor: David M. Parks

Tile: Professor of Mechanical Engineering

Acknowledgements

I would like to thank my advisors Prof. Mary C. Boyce and Prof. David M. Parks for their guidance and support during the period of my master study and research in MIT.

I also would like to express my appreciation to the help and cooperation from the DURINT group members, especially Prof. Gregory Rutledge and Dr. Hojun Lee. Some of the data and results of their research are included in this thesis.

Thanks to my colleague graduate students in 1-321 and 1-107, who helped me learning ABAQUS and working with the Instron machine and thanks to Ray and Una for making everything a little easier.

Contents

Chapter 1

Introduction

Polymer materials are often reinforced by stiff fillers to improve mechanical properties. The efficiency of reinforcement depends on the filler aspect ratio, the filler mechanical properties, and the adhesion between the matrix and the filler. As early as 1974, Maine and Shepherd (Maine and Shepherd, 1974) had suggested that single clay layers would serve as an ideal reinforcing material due to their high aspect ratio and also due to the filler length scale being comparable to the polymer chain structure (the thickness of a single silicate layer is 1-100 nm), provided that they could be separated and dispersed into the matrix properly. Two years later, a two-step synthesis of a 'nylon 6/clay nanocomposite' was reported by Fujiwara and Sakamoto (1976). Although this method has been recognized as the actual origin of the polymer/clay nanocomposite technology, it was not economically suitable for industrial production because of its extraordinarily high cost. The real breakthrough came almost twenty years later. In 1993, the Toyota research group reported the accomplishment of the '*in situ* polymerization' method and demonstrated the unprecedented mechanical properties of nylon 6/clay nanocomposites (Kojima, Usuki, Kawasumi, Okada, Fukushima, Kurauchi, and Kamigaito). They showed that a doubling of both the tensile modulus and tensile strength is achieved with as little as 4.7-weight percentage clay. Furthermore, the property enhancements extend to relatively high temperatures and, indeed, act to substantially increase "transition temperatures" over that of the parent homopolymer (an increase of 80C in the heat

distortion temperature has been observed). Table 1.1 lists mechanical properties of nylon 6/clay nanocomposite with 4.7-weight percentage montmorillonite given in the original paper of the Toyota Central Lab.

Table 1.1: Mechanical properties of nylon 6/clay nanocomposite (Kojima, Usuki, Kawasumi, Okada, Fukushima, Kurauchi, and Kamigaito, 1993)

Properties		Nylon 6	Nylon 6/clay nanocomposite
Tensile strength (MPa)	23°C	68.6	97.2
	120°C	26.6	32.3
Tensile modulus (GPa)	23°C	1.11	1.87
	120°C	0.19	0.61
Flexural strength (MPa)	23°C	89.3	143
	120°C	12.5	32.7
Flexural modulus (GPa)	23°C	1.94	4.34
	120°C	0.29	1.16
Izod impact strength (J/m)		20.6	18.1
Charpy impact strength (kJ/m)		6.21	6.06
HDT (1.82 MPa) (°C)		65	152

Over the last decade, polymer/clay nanocomposites have been observed to exhibit dramatic enhancement of many physical properties in addition to the mechanical properties, including barrier (Yano, Usuki, Okada, Kurauchi and Kamigaito, 1993; Messersmith and Giannelis, 1994, 1995), flammability resistance (Gilman, 1999), and ablation performance (Vaia, Price, Ruth, Nguyen and Lichtenhan, 1999).

These property enhancements have been speculated to be linked to the nanometer length scale of the local polymer morphology surrounding the particles acting to percolate

throughout the matrix. In this thesis, we explore the connections between the underlying material structure and the anisotropic mechanical properties through a series of micro/nano-scale models of the nano-clay-particle-filled polymer. In particular, we explore the potential contribution of composite-level effects on the observed macroscopic stiffness of clay-filled thermoplastics. Predictions of the macroscopic anisotropic moduli as functions of particle volume fraction, particle aspect ratio, particle dispersion (patterned vs. random) and particle/matrix mechanical properties are presented. The FE simulation results are compared to predictions using traditional composite theories as well as uniaxial tensile experimental data. The potential impact of local polymer morphology on the behavior is also discussed.

This thesis contains 7 chapters that focus on different aspects: 1. a brief review on the microstructure of polymer-clay nanocomposites and the existing micromechanics composite theories; 2. details regarding the finite element micromechanical model, including the parameters, boundary conditions and average properties; 3. micromechanical model results under axial loading and the mechanisms of stiffness enhancement; 4. the structure of the intercalated clay particle and an estimation of its effective properties; 5. comparison of the micromechanical model predictions with axial tensile experimental data, using formula for the effective clay particle developed in part 4; 6. micromechanical model results under other modes of loading; 7. conclusions and the directions of future work.

1.1. Hierarchical Morphology of Polymer/Layered-Silicate Nanocomposites

The morphology of polymer/layered-silicate composites has a hierarchical structure. The dispersion of the clay in the matrix is typically described in terms of *intercalation* vs. *exfoliation*. In the *intercalated* structure, the primary clay particles are penetrated by polymer chains and consequently expand, with a typical interlayer spacing of the order of 1-4 nm; in contrast, the perfectly-exfoliated morphology consists of single silicate layers dispersed in a polymer matrix. In practice, however, many systems fall between these two idealized morphologies. Kinetic aspects associated with Brownian motion and shear alignment of the layers, as well as processing histories, will produce positional and orientational correlations between the plates. These kinetic factors contribute to the development of a hierarchical morphology exhibiting nano-, meso-, and micro-level features. A summary of the morphology of polymer-layered silicate composites, and of corresponding microscopy and scattering techniques to determine such hierarchical morphology, was given by Vaia (2000). Vaia proposed additional descriptors, such as ordered, disordered, and partial, to give a more accurate description of nanocomposite morphologies, rather than merely intercalated or exfoliated, as illustrated in Figure 1.1.

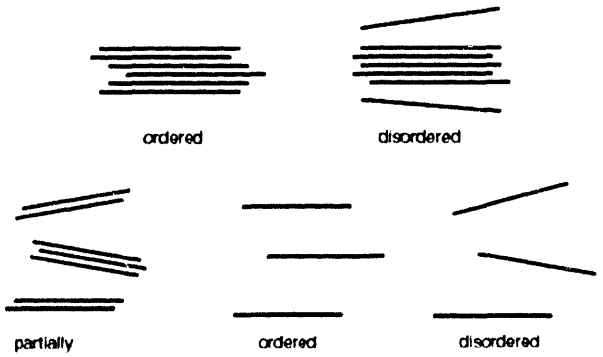

Figure 1.1 General classifications of nanocomposite morphologies (Vaia, 2000).

Characteristic parameters of various length scales are necessary in order to capture the special hierarchical morphology of nanocomposites. Recently Okamoto and coworkers (Nam, Maiti, Okamoto, Kotaka, Hasegawa and Usuki, 2001) have successfully characterized the hierarchical structure of intercalated polypropylene/clay nanocomposites (PPCN) using WAX, SAX, TEM, polarized optical microscopy and light scattering. Figure 1.2 shows a schematic of such a structure and illustrates the parameters of various hierarchies.

Among the parameters, the micro/meso/nano-scale measures and representative values of each of these scales for 4-wt % PPCN (Nam, Maiti, Okamoto, Kotaka, Hasegawa and Usuki, 2001) are listed as following:

L_{clay} [*130~180 nm*]
Length of the dispersed clay particles;

ξ_{clay} [*40~60 nm*]
Correlation length between the dispersed layers (inter-particle spacing);

t_{clay} [*7~9 nm*]
Thickness of the dispersed clay particles;

$d_{(001)}$ [*3nm*]
Inter-layer spacing of the (001) plane in intercalated multi-layer clay particle;

$d_{lamellae}$ [*7nm*]
Average lamellae thickness of polymer matrix crystallite (if semi-crystalline);

$L_{lamellae}$ [*15nm*]
Long-period lamellae thickness of polymer matrix crystallite (if semi-crystalline).

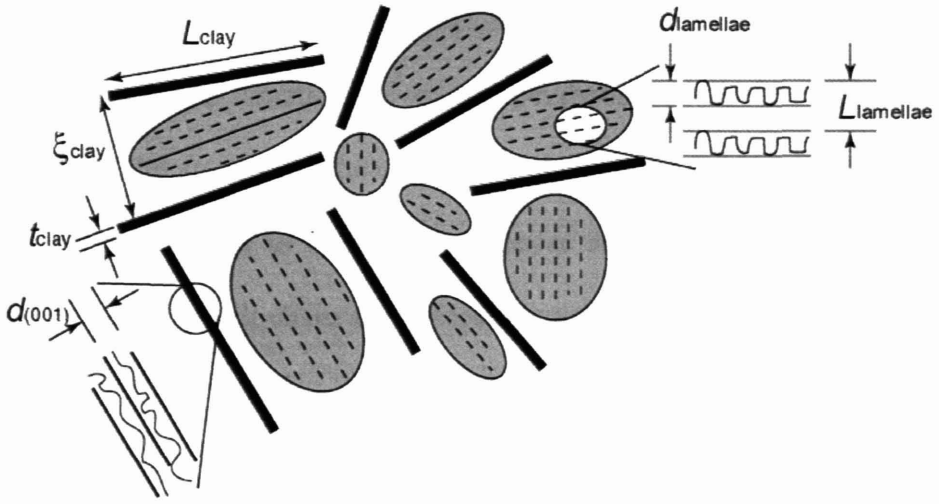

Figure 1.2 Schematic of hierarchical morphology and characteristic parameters (Nam, Maiti, Okamoto, Kotaka, Hasegawa and Usuki, 2001).

In an intercalated structure, where the inter-layer spacing ($d_{(001)}$ in Figure 1.2) within a multi-layer stack of clay is usually 1-3nm, the intra-layer polymer chains have a highly confined morphology. In the exfoliated or partially exfoliated systems, the particle separation (ξ_{clay}) is about 20-50 nm, and is on the same order of crystal lamellae. Such spacing, along with the detailed molecular interaction between clay and polymer, has an impact on the forming of crystallites in semi-crystalline polymer matrix, as observed in many morphology studies. Kim and coworkers (Kim, Lee, Hoffmann, Kressler and Stoppelmann, 2001) discovered from TEM on a clay/polyamide-12 nanocomposite that, although the silicate layers preferentially align in the flow direction of injection molding, the fine polymer lamellae are oriented perpendicular to the silicate layer, as shown in Figure 1.3.

Other observations from the Toyota Central Lab (Kojima, Usuki, Kawasumi, Okada, Kurauchi, Kamigaito and Kaji, 1995), however, show that the preferred orientation of both the silicate layer and the polymer lamellae varies with the depth from the surface of the injection-molded specimen: in the surface layer, both the silicate and the lamellae are

parallel to the specimen surface, while in the intermediate layer, the silicate plates remain parallel, but the lamellae become perpendicular to the specimen surface. In the middle layer of the specimen, the silicates are randomly oriented around the flow axis while remaining parallel to it, and the lamellae are randomly oriented around the flow axis while keeping their chain axes perpendicular to the silicate.

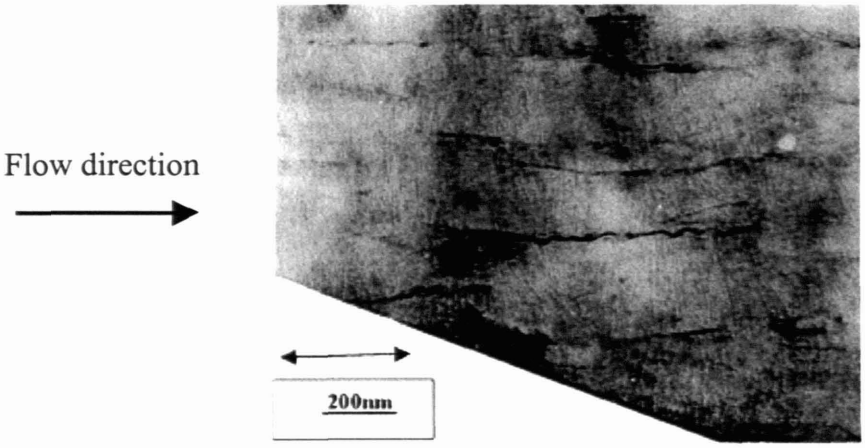

Figure 1.3 TEM on Nylon-12/clay nanocomposite, showing a lamellae structure perpendicular to the aligned clay particles (Kim, Lee, Hoffmann, Kressler and Stoppelmann, 2001).

1.2. Traditional Composite Theories

The prediction of the mechanical properties of unidirectional short-fiber/flake composite materials has been a subject of extensive study. Various micromechanical models, such as the dilute model based on Eshelby's equivalent inclusion theory, the self-consistent model, the Mori-Tanaka model and its extensions, the Halpin-Tsai equation and its extensions, shear-lag models, and bound theories have been proposed to predict a complete set of elastic constants for unidirectional short-fiber/flake composites. These models generally include parameters of particle and matrix properties, particle volume

fraction, and particle aspect ratio and orientation. In applications relevant to the present study, the particles and the matrix are assumed to be linearly elastic, with the matrix isotropic and the particles either isotropic or transversely isotropic. A good review and evaluation of these models is given by Tucker (1999). Of all the existing models, as Tucker pointed out, the widely-used Halpin-Tsai equations give reasonable estimates for effective stiffness, but the Mori-Tanaka type models give the best results for large-aspect-ratio fillers. Since the large aspect ratio of the silicate layers in the nanocomposites inevitably induces particle-particle interaction (overlapping of the stress fields due to the small inter-particle spacing relative to particle size), even at small volume fractions, we address only models that efficiently account for effects of particle interaction. Here, we first introduce the Mori-Tanaka model (Mori and Tanaka, 1973) and a closed-form analytical expression proposed by Tandon and Weng (1984), which is a combination of the Mori-Tanaka theory and Eshelby equivalent inclusion theory (Eshelby, 1957). The widely-used Halpin-Tsai equations (Ashton, Halpin and Petit, 1969; Halpin, 1969) are also included for comparison and evaluation. The shear lag model that describes the load transfer mechanics will be briefly introduced in Chapter 3. In Chapter 5, we will compare the predictions of the Mori-Tanaka model and the Halpin-Tsai equation with the axial tensile test data and our simulation results.

1.2.1. Preliminaries regarding average properties

Consider a representative volume element (RVE) of Volume V, with a particle volume of V_p and matrix volume V_m:

$$V = V_p + V_m. \tag{1.1}$$

In terms of particle volume fraction f_p and matrix volume fraction f_m ($f_p = V_p/V$, $f_m = V_m/V$), we have $f_p + f_m = 1$. The average particle and matrix stresses and strains are the averages over the whole RVE,

$$\bar{\boldsymbol{\sigma}}^p = \frac{1}{V_p}\int_{V_p}\boldsymbol{\sigma}(x)dV\,;\ \bar{\boldsymbol{\sigma}}^m = \frac{1}{V_m}\int_{V_m}\boldsymbol{\sigma}(x)dV\,; \tag{1.2}$$

$$\bar{\boldsymbol{\varepsilon}}^p = \frac{1}{V_p}\int_{V_p}\boldsymbol{\varepsilon}(x)dV\,;\ \bar{\boldsymbol{\varepsilon}}^m = \frac{1}{V_m}\int_{V_m}\boldsymbol{\varepsilon}(x)dV\,. \tag{1.3}$$

where $\boldsymbol{\sigma}$ and $\boldsymbol{\varepsilon}$ are second-order stress tensor and strain tensor, and the superscripts p and m represent particle and matrix, respectively.

The relationships between the overall average quantities ($\bar{\boldsymbol{\sigma}}, \bar{\boldsymbol{\varepsilon}}$) and the particle and matrix averages are:

$$\bar{\boldsymbol{\sigma}} = \frac{1}{V}\int_{V}\boldsymbol{\sigma}(x)dV = f_p\bar{\boldsymbol{\sigma}}^p + f_m\bar{\boldsymbol{\sigma}}^m\,, \tag{1.4}$$

$$\bar{\boldsymbol{\varepsilon}} = \frac{1}{V}\int_{V}\boldsymbol{\varepsilon}(x)dV = f_p\bar{\boldsymbol{\varepsilon}}^p + f_m\bar{\boldsymbol{\varepsilon}}^m\,. \tag{1.5}$$

The average (effective) stiffness of the composite is the fourth-order tensor $\boldsymbol{C}$ that maps the average strain to the average stress:

$$\bar{\boldsymbol{\sigma}} = \boldsymbol{C}\bar{\boldsymbol{\varepsilon}}\,. \tag{1.6}$$

Similarly, the average compliance tensor $\boldsymbol{S}$ is defined as:

$$\bar{\boldsymbol{\varepsilon}} = \boldsymbol{S}\bar{\boldsymbol{\sigma}}\,. \tag{1.7}$$

The average particle strain and stress are related to the overall average strain and stress through the strain concentration tensor $\boldsymbol{A}$ and stress concentration tensor $\boldsymbol{B}$

$$\bar{\boldsymbol{\varepsilon}}^p = \boldsymbol{A}\bar{\boldsymbol{\varepsilon}}\,; \tag{1.8}$$

$$\bar{\boldsymbol{\sigma}}^p = \boldsymbol{B}\bar{\boldsymbol{\sigma}}\,. \tag{1.9}$$

Using these relations, the average properties can be expressed in terms of the particle and matrix properties, particle volume fraction, and the concentration tensors

$$\boldsymbol{C} = \boldsymbol{C}^m + f_p(\boldsymbol{C}^p - \boldsymbol{C}^m)\boldsymbol{A}; \tag{1.10}$$

$$\boldsymbol{S} = \boldsymbol{S}^m + f_p(\boldsymbol{S}^p - \boldsymbol{S}^m)\boldsymbol{B}, \tag{1.11}$$

where $\boldsymbol{C}^p$ and $\boldsymbol{C}^m$ are elastic stiffness tensors of the matrix and particle phases, respectively, and $\boldsymbol{S}^p$ and $\boldsymbol{S}^m$ are the respective compliance tensors.

1.2.2. Eshelby's equivalent inclusion, dilute Eshelby model and Mori-Tanaka model

Eshelby's equivalent inclusion theory (Eshelby, 1957) is a foundation for several micromechanics models including the Mori-Tanaka model and the self-consistent model. It's necessary for us to be familiar with the Eshelby model first.

Eshelby solved the elasticity problem of an ellipsoidal particle embedded in an infinite linear elastic matrix, subjected to a far-field strain. The local strain field is complicated due to the existence of a second phase of different properties. Denote the far-field strain by $\boldsymbol{\varepsilon}^A$ and the strain perturbation in the particle by $\tilde{\boldsymbol{\varepsilon}}^p$; the particle strain $\boldsymbol{\varepsilon}^p$ is thus:

$$\boldsymbol{\varepsilon}^p = \boldsymbol{\varepsilon}^A + \tilde{\boldsymbol{\varepsilon}}^p. \tag{1.12}$$

In order to solve the heterogeneous problem, Eshelby proposed the important concept of "**equivalent inclusion**". An "equivalent inclusion" is an ellipsoidal region matching the geometry of the actual inclusion, but possessing the matrix properties. This inclusion is made "equivalent" to the heterogeneity (in the sense that both undergo the same strain and stress) by giving it a **transformation strain $\boldsymbol{\varepsilon}^T$ that does not generate stress**; the

value of $\boldsymbol{\varepsilon}^T$ is chosen to satisfy the stress equivalence between the heterogeneous problem and the homogeneous problem:

$$\boldsymbol{\sigma}^p = \boldsymbol{C}^p(\boldsymbol{\varepsilon}^A + \tilde{\boldsymbol{\varepsilon}}^p) = \boldsymbol{C}^m(\boldsymbol{\varepsilon}^A + \tilde{\boldsymbol{\varepsilon}}^p - \boldsymbol{\varepsilon}^T). \tag{1.13}$$

Table 1.2 summarizes the stress and strain states of the heterogeneous inclusion and its "equivalent inclusion".

An essential result of Eshelby in solving the homogeneous inclusion problem is that the strain perturbation in the particle is uniform within the inclusion, and more importantly, proportional to the transformation strain:

$$\tilde{\boldsymbol{\varepsilon}}^p = \boldsymbol{H}\boldsymbol{\varepsilon}^T \tag{1.14}$$

where $\boldsymbol{H}$ is the Eshelby's tensor, which only depends on the particle aspect ratio and dimensionless elastic constants of the matrix (components of the Eshelby tensor for ellipsoidal/spherical particles in an isotropic linear elastic matrix are given in Appendix A). Take (1.14) into (1.13), we are able to relate the transformation strain to the far-field strain according to:

$$-\left[\boldsymbol{C}^m + (\boldsymbol{C}^p - \boldsymbol{C}^m)\boldsymbol{H}\right]\boldsymbol{\varepsilon}^T = (\boldsymbol{C}^p - \boldsymbol{C}^m)\boldsymbol{\varepsilon}^A \tag{1.15}$$

Table 1.2 Comparison between the actual and "equivalent" inclusions under far-field strain $\boldsymbol{\varepsilon}^A$

	Actual inclusion	Equivalent inclusion
Property	$\boldsymbol{C}^p$	$\boldsymbol{C}^m$
Strain	$\boldsymbol{\varepsilon}^A + \tilde{\boldsymbol{\varepsilon}}^p$	$\boldsymbol{\varepsilon}^A + \tilde{\boldsymbol{\varepsilon}}^p$, $\tilde{\boldsymbol{\varepsilon}}^p = \boldsymbol{\varepsilon}^T + (\tilde{\boldsymbol{\varepsilon}}^p - \boldsymbol{\varepsilon}^T)$
Cause of strain perturbation	Property difference	Transformation strain in the particle, $\boldsymbol{C}^m\boldsymbol{\varepsilon}^T = \boldsymbol{0}$
Stress	$\boldsymbol{C}^p(\boldsymbol{\varepsilon}^A + \tilde{\boldsymbol{\varepsilon}}^p)$	$\boldsymbol{C}^m(\boldsymbol{\varepsilon}^A + \tilde{\boldsymbol{\varepsilon}}^p - \boldsymbol{\varepsilon}^T)$

Eshelby's result can be used directly to determine the effective stiffness of a composite with ellipsoidal fillers at **dilute** concentrations. Here we describe a composite system as "dilute" in the sense that the spacing of particles is large enough so that the perturbation of the matrix strain field resulting from each particle vanishes (according to *Saint-Venant's principle*) before it can have an effect on any other particles; each particle behaves as if it is "isolated", since it cannot sense the presence of the others. In such a dilute system, the far-field strain is identical to the average strain of the composite

$$\boldsymbol{\varepsilon}^A = \bar{\boldsymbol{\varepsilon}}. \tag{1.16}$$

Combining Eqs. (1.16), (1.15), (1.14), (1.12) and (1.8), we have the strain concentration tensor as

$$\boldsymbol{A} = \left[\boldsymbol{I} + \boldsymbol{HS}^m(\boldsymbol{C}^p - \boldsymbol{C}^m)\right]^{-1}. \tag{1.17}$$

The average stiffness tensor $\boldsymbol{C}$ is easily obtained by taking (1.17) into (1.10)

$$\boldsymbol{C} = \boldsymbol{C}^m + f_p(\boldsymbol{C}^p - \boldsymbol{C}^m)\left[\boldsymbol{I} + \boldsymbol{HS}^m(\boldsymbol{C}^p - \boldsymbol{C}^m)\right]^{-1}. \tag{1.18}$$

Analytical results of the five independent elastic moduli of a composite with aligned ellipsoidal inclusions (considered as transversely isotropic) were developed by Russel (1973), who obtained the effective moduli by solving three boundary problems using the dilute Eshelby model; details are given in Appendix B.

However, in non-dilute composites, the far-field strain for the inclusion can no longer be taken to be equal to the overall average strain, due to the interactions between particles. The dilute Eshelby model is accurate only at low particle volume fraction where each particle "sees" only the far-field strain. Predictions of the longitudinal stiffness of a composite with axially-aligned disc-like ellipsoidal particles or spherical particles using

the dilute Eshelby model and the Mori-Tanaka model, which approximately takes into account the effect of particle-particle interaction, are compared in Appendix C.

The essential assumption of the **Mori-Tanaka** model is that the inclusion in a non-dilute composite "sees" itself as being embedded in a domain subjected to the average strain of the matrix, instead of the overall strain of the composite, i.e.,

$$\varepsilon^A = \bar{\varepsilon}^m \tag{1.19}$$

Tandon and **Weng** (1984) developed a closed-form analytical solution for the overall elastic properties by combining the Eshelby equivalent inclusion theory and the Mori-Tanaka model. The components of the Eshelby tensor $\boldsymbol{H}$ for spheres, fiber-shaped particles, and disc-shaped particles are also given in their paper. For a material reinforced with ellipsoidal particles aligned along direction 1 (direction 2=3 due to the axial symmetry), the Tandon-Weng prediction of the Young's moduli E_{11}, E_{22} ($E_{22} = E_{33}$), and the out-plane shear modulus G_{12} of the composite are:

$$\frac{E_{11}}{E_m} = \frac{1}{1 + f_p(A_1 + 2v_m A_2)/A}, \tag{1.20}$$

$$\frac{E_{22}}{E_m} = \frac{1}{1 + f_p[-2v_m A_3 + (1 - v_m)A_4 + (1 + v_m)A_5 A]/2A}, \tag{1.21}$$

$$\frac{G_{12}}{G_m} = 1 + \frac{f_p}{G_m/(G_p - G_m) + 2(1 - f_p)H_{1212}}, \tag{1.22}$$

where A_i are constants depending on the components of the Eshelby tensor and the matrix/particle properties, H_{ijkl} are the Cartesian components of the Eshelby tensor, E_m, v_m and G_m are the Young's modulus, Poisson's ratio and shear modulus of the matrix, respectively. Note that which of the two Young's modulus, E_{11} and E_{22}, is the one of larger reinforcement (assuming $E_p >> E_m$) depends on the shape of the ellipsoidal

inclusion: for a fiber-like particle rotated about its major axis (1) (Figure 1.4 a), $E_{11}>E_{22}=E_{33}$; for a disc-like particle rotated about its minor axis (1) (Figure 1.4 b), $E_{22}=E_{33}>E_{11}$.

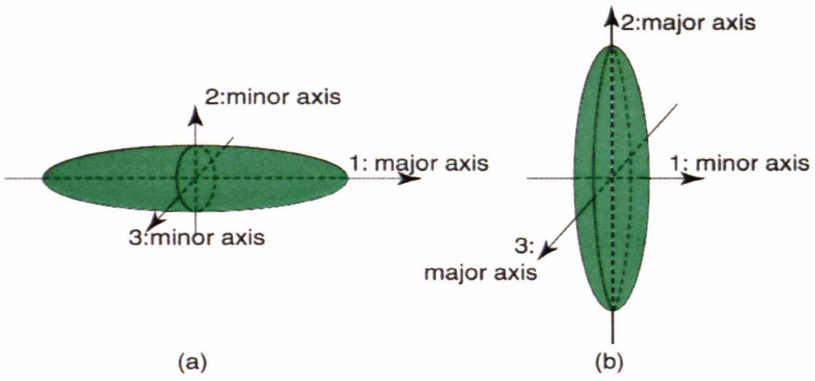

Figure 1.4 Schematic of spheroidal particles: (a) fiber-like particle; (b) disc-like particle.

1.2.3. Halpin-Tsai Equations

The Halpin-Tsai equations are one of the most popular formulas for predicting the properties of composites with unidirectional discontinuous fillers such as whiskers or ribbons. The estimation of the elastic constants of the composite can be expressed in a common form:

$$\frac{M_c}{M_m}=\frac{1+\zeta\eta v_p}{1-\eta v_p}, \tag{1.23}$$

$$\eta=\frac{(M_p/M_m)-1}{(M_p/M_m)+\zeta},$$

where M_p, M_m and M_c represent the property of the particle, the matrix, and the composite, respectively. Here ζ is a shape factor that can be fit to simulation or experimental results. A detailed review of the Halpin-Tsai equations is given by Halpin and Kardos (1976). Here, we present a brief summary of the development of Halpin-Tsai equations. In particular, we note how Halpin and Tsai reduced the results of the 'self-

consistent method' developed by Hill (1964) to a simpler analytical form and how, later on, they extended its use to various particle geometries.

Hill modeled the composite as a single fiber encased in a cylinder of matrix, the diameter of which is chosen such that $V_f/(V_f+V_m) = f_p$, where V_f and V_m are the fiber volume and matrix volume, respectively, and f_p is the overall composite volume fraction; in turn this cylinder of matrix is embedded in an unbounded homogeneous medium which has the same macroscopic elastic properties as the composite (to be determined). Both the cylindrical matrix and the fiber are assumed to be homogeneous and isotropic.

Hermans (1967) employed Hill's self-consistent model and obtained an elastic solution of the plane strain bulk modulus k, the transverse shear modulus m, and the longitudinal shear modulus μ (here we follow Hill's notation):

$$k = \frac{k_m(k_p + m_m)(1-f_p) + k_p(k_m + m_m)f_p}{(k_p + m_m)(1-f_p) + (k_m + m_m)}; \tag{1.24}$$

$$m = m_m \frac{2f_p m_p(k_m + m_m) + 2(1-f_p)m_m^2 + (1-f_p)k_m(m_p + m_m)}{2f_p m_m(k_m + m_m) + 2(1-f_p)m_p m_m + (1-f_p)k_m(m_p + m_m)}; \tag{1.25}$$

$$\mu = \frac{\mu_p + \mu_m\left[\mu_m(1-f_p) + 2\mu_p\mu_m f_p\right]}{\mu_p + \mu_m(1-f_p) + 2\mu_m f_p}; \tag{1.26}$$

where the subscripts p and m denote particle and matrix, respectively.

Halpin and Tsai re-arranged Herman's solutions ((1.24), (1.25), (1.26)), which result from exact elasticity theory, so that they all conform to one generalized form given in (1.23). Note that the parameter ζ has different expressions for different elastic moduli, as listed in Table 1.3. Halpin and Tsai made the following approximations in order to obtain more convenient forms for engineering constants:

- Eq. (1.23) can be used to predict engineering constants E_{11} and E_{22}

- The parameters ζ listed in Table 1.3 can be treated as constants since they are insensitive to v_m

Furthermore, Halpin and Tsai suggested that the value of ζ was correlated with the geometry of the reinforcement and could be obtained by comparison of the Halpin-Tsai equations with numerical micromechanics solutions. Ashton (1969) fit the shape factor ζ to theoretical equations and found the following relations to predict elastic constants of ribbon-reinforced composites having their long dimension parallel to the 1-direction:

$\zeta = 2L/t$, for the estimation of longitudinal stiffness E_{11};

$\zeta = 2$, for the estimation of transverse stiffness E_{22};

$\zeta = 1$, for the estimation of out-plane shear modulus G_{12}.

Table 1.3: Parameter ζ in the Halpin-Tsai equations corresponding to various elastic moduli (both matrix and particle are assumed to be isotropic)

Elastic moduli	ζ-value
Plane strain bulk modulus (aligned fibers)	$(1-v_m-2v_m^2)/(1+v_m)$
Transverse shear modulus (aligned fibers)	$(1+v_m)/(3-v_m-4v_m^2)$
Longitudinal shear modulus (aligned fibers)	1
Bulk modulus (spherical particulates)	$2(1-2v_m)/(1+v_m)$
Shear modulus (spherical particulates)	$(7-5v_m)/(8-10v_m)$

1.2.4. Comparison

Following Tucker's evaluation of the micromechanics models, we focus on only two composite approaches: the more accurate Mori-Tanaka-type models, and the simple and

reasonably accurate Halpin-Tsai equations. In later discussion of simulation results under different loading conditions (Chapters 3, 4, and 5), the simulation predictions of the effective longitudinal modulus E_{11}, the effective transverse modulus E_{22}, the effective out-plane shear modulus G_{12} and the transverse Poisson's ratios ν_{12} and ν_{21} will be compared to the predictions using these two composite theories, as well as to the experimental data. Here, the Mori-Tanaka and the Halpin-Tsai predictions of the longitudinal modulus E_{11} of a composite with aligned disc-like ellipsoidal particles are presented in Figure 1.5, 1.6, and 1.7, with E_{11} plotted as a function of particle volume fraction f_p, particle aspect ratio L/t, and the ratio of particle/matrix stiffness E_p/E_m respectively. The following observations are made regarding these predictions:

1) Both models predict a dramatic enhancement in E_{11} at small filler loadings provided the particle aspect ratio is large and $E_p/E_m >> 1$.
2) Both models predict an increases in E_{11} with increasing f_p, L/t, and E_p/E_m; while the increase with f_p is linear, the increases with both L/t and E_p/E_m exhibit saturation after a certain value.
3) When compared to the Mori-Tanaka model, the Halpin-Tsai equation predicts a larger influence of the individual parameters, and as a result gives a larger estimation of the effective longitudinal modulus.

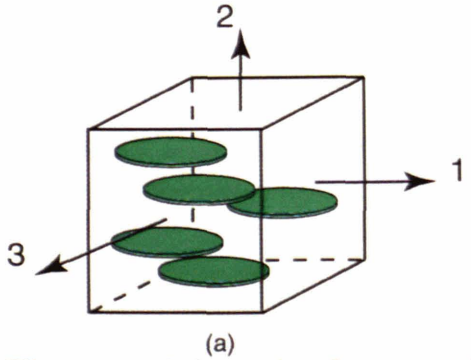

Figure 1.5 Schematic of a composite with aligned platelet fillers

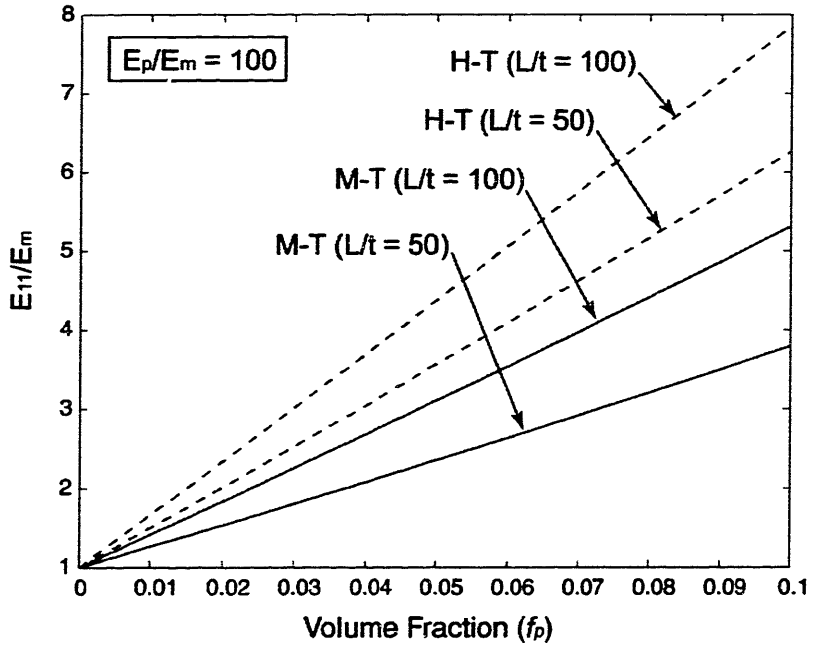

Figure 1.6 Dependence of E_{11} on clay content with M-T denoting Mori-Tanaka and H-T denoting Halpin-Tsai ($E_p/E_m = 100$).

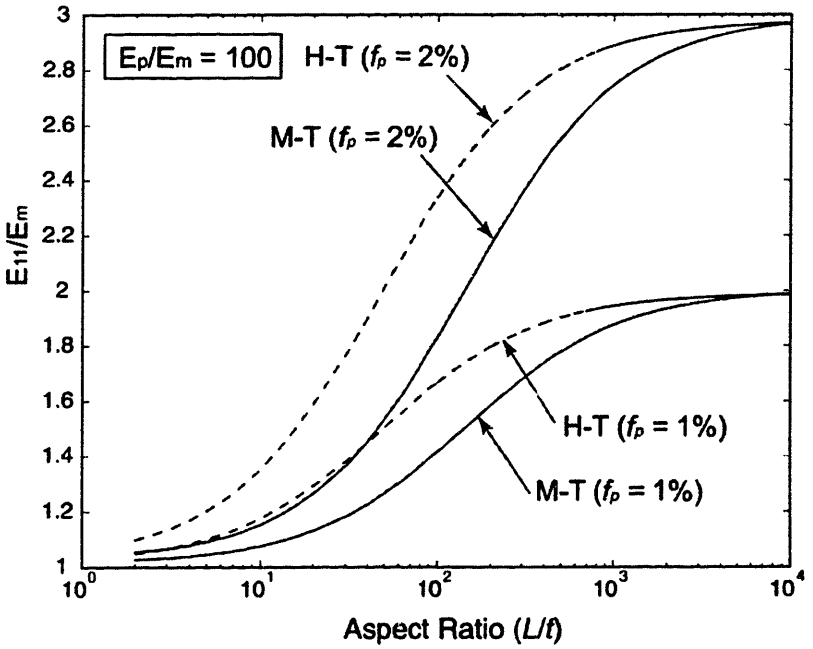

Figure 1.7 Dependence of E_{11} on particle aspect ratio with M-T denoting Mori-Tanaka and H-T denoting Halpin-Tsai ($E_p/E_m = 100$).

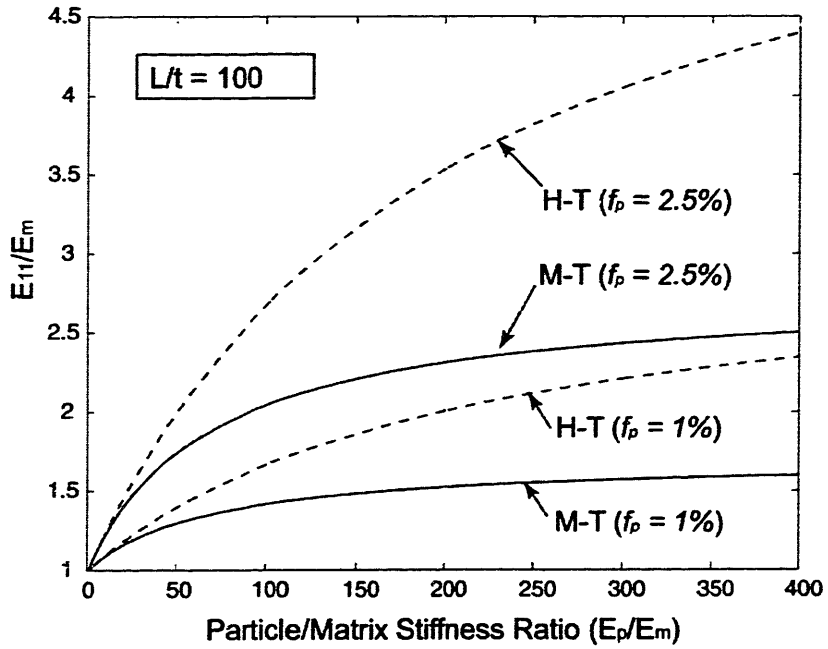

Figure 1.8 Dependence of E_{11} on particle/matrix stiffness ratio with M-T denoting Mori-Tanaka and H-T denoting Halpin-Tsai (L/t = 100).

The predictions of E_{22}, G_{12}, and v_{21} using these two composite theories are presented in Figure 1.8, Figure 1.9, and Figure 1.10, respectively. The following observations are made based on these predictions:

- E_{22} is not enhanced as dramatically as E_{11}. While the Halpin-Tsai prediction of E_{22} is insensitive to the particle aspect ratio L/t (recall that ζ in (1.23) is not a function of particle aspect ratio for evaluation of E_{22}), the Mori-Tanaka model predicts better reinforcing effect of particles with larger L/t.
- G_{12} increases with an increase in particle volume fraction. However the increase in G_{12} is almost negligible compared with the increase in E_{11}. Again, the Halpin-Tsai prediction of G_{12} ignores the influence of L/t; while the Mori-Tanaka model predicts slightly lower G_{12} for particles with larger L/t.

- Both models predict a decrease in v_{21} with an increase of particle concentration (note that v_{12} is almost the same as the Poisson's ratio of the matrix). Both models show that the larger the particle aspect ratio is, the bigger the impact of particle volume fraction on v_{21} is.

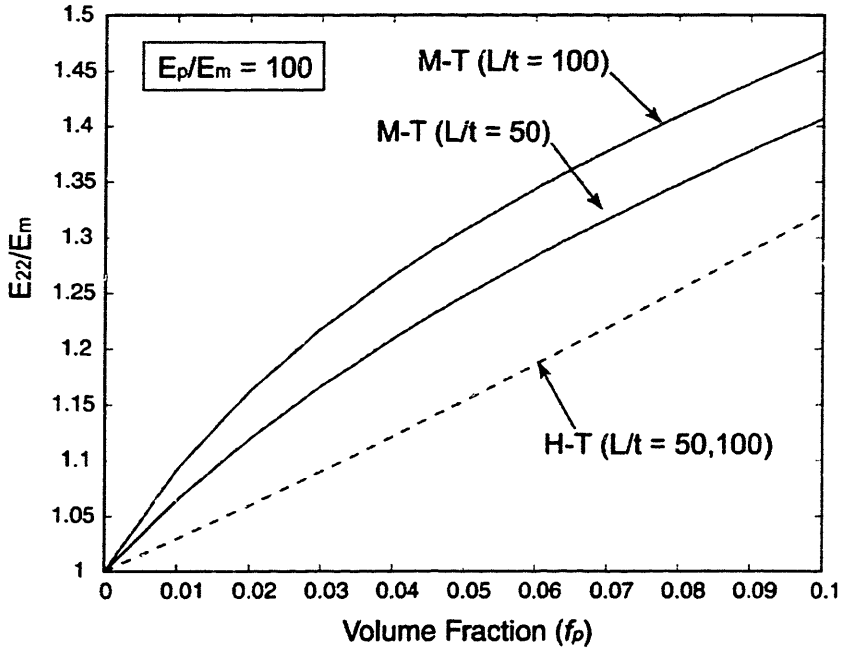

Figure 1.9 Prediction of effective transverse stiffness E_{22} with M-T denoting Mori-Tanaka and H-T denoting Halpin-Tsai ($E_p/E_m = 100$, $v_m = 0.35$, $v_p = 0.20$).

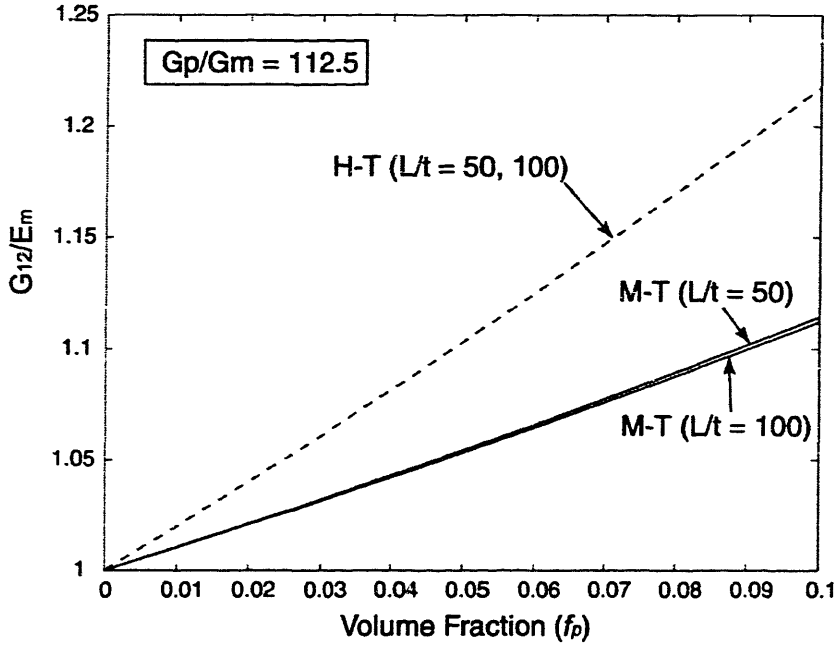

Figure 1.10 Prediction of effective out-plane shear modulus G_{12} with M-T denoting Mori-Tanaka and H-T denoting Halpin-Tsai ($G_p/G_m = 112.5$).

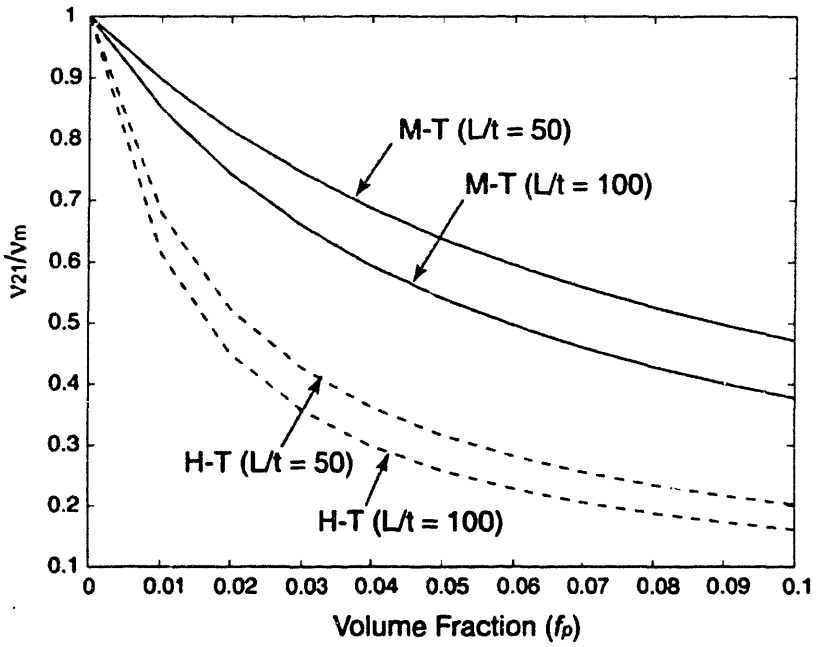

Figure 1.11 Prediction of effective Poisson's ratio ν_{21} with M-T denoting Mori-Tanaka and H-T denoting Halpin-Tsai ($E_p/E_m = 100$, $\nu_m = 0.35$, $\nu_p = 0.20$).

Chapter 2

Model Description

2.1. Important Model Parameters

The polymer/layered-silicate nanocomposite systems possess a complicated hierarchical morphology (section 1.2). It is almost impossible to build a model that captures every morphological and material detail of such a sophisticated system. Even if such a model is successfully created, the amount of time spent on model development and numerical calculation will be frustrating and, indeed, may fail to identify the relative importance and dominance of specific structural features. In this thesis, we focus on studying the effects of those features closely related to the macroscopic material behavior of the nanocomposite.

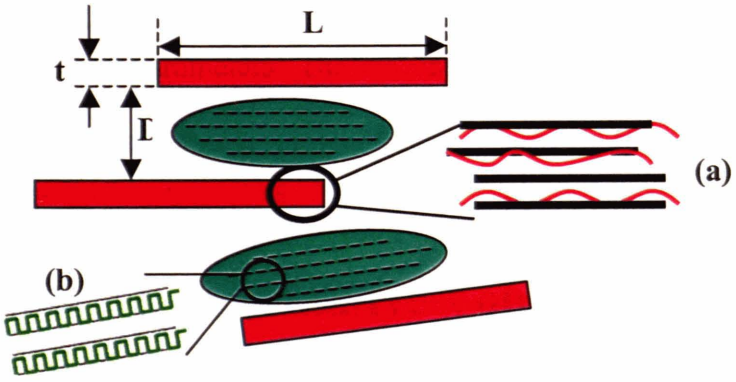

Figure 2.1 Schematic of the hierarchical morphology of polymer/layered-silicate nanocomposite. (a) Multi-layer stack in an intercalated structure. (b) Lamellar structure in semi-crystalline polymer.

Generally speaking, the important geometrical features of nano-clay-filled polymer composites can be thought of in terms of clay dispersion, clay volume fraction, clay

aspect ratio (diameter/thickness, L/t), clay platelet orientation distribution, and clay platelet curvature distribution; the material features can be described in terms of clay intercalation vs. exfoliation, clay/particle interface behavior, and polymer morphology (both in the vicinity of particles, and away from particles).

Particularly, for an intercalated clay stack (Figure 2.1 (a)), the number of individual layers and the inter-layer spacing are important parameters; for a semi-crystalline polymer (Figure 2.1 (b)), quantities such as lamellar orientation, degree of crystallization, and lamellar thickness are important morphological features.

So far, our model contains the particle volume fraction f_p, particle length distribution L and δL (L denotes the mean value and δL denotes the variance), particle thickness distribution t and δt (t denotes the mean value and δt denotes the variance), and particle position dispersion (random vs. patterned) as geometrical parameters; and the elastic properties of matrix and particle, E_m, v_m, E_p, and v_p (E and v are the Young's modulus and Poisson ratio; subscripts m and p denote the matrix and the particle, respectively), as material parameters. The current model will be modified in future work to incorporate more micro-structural details, as described in the previous section.

2.2. Representative Volume Element (RVE)

Models of various RVEs of the underlying structure of the nano-clay filled polymers are constructed. A schematic RVE of the general three-dimensional case of nano-clay particles randomly distributed in a polymer matrix is shown in Figure 2.2. We can simplify the representation to two-dimensions and also specialize to highly oriented dispersions, as shown in Figure 2.2. Furthermore, the random dispersion can then be

idealized to different cases of regular patterned distributions such as a stacked array and a staggered array, as depicted in Figure 2.3.

Note that for a system with randomly distributed particles, the number of particles needed to be included in a model in order to obtain an accurate representation of this structure is an important quantity; here we are showing a highly simplified schematic for illustrative purposes only.

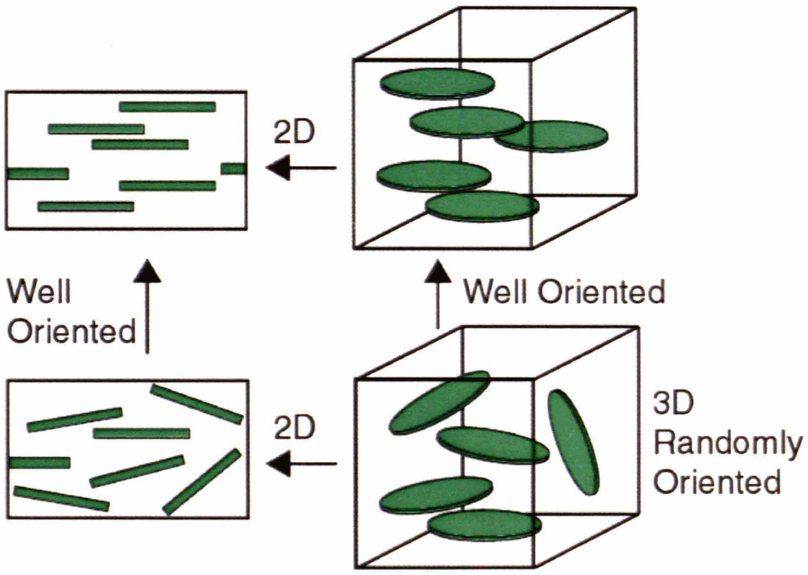

Figure 2.2 Schematic representative volume elements.

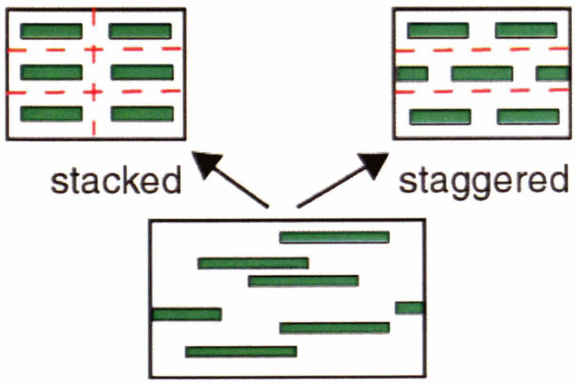

Figure 2.3 Regular patterned clay dispersions ("stacked" and "staggered").

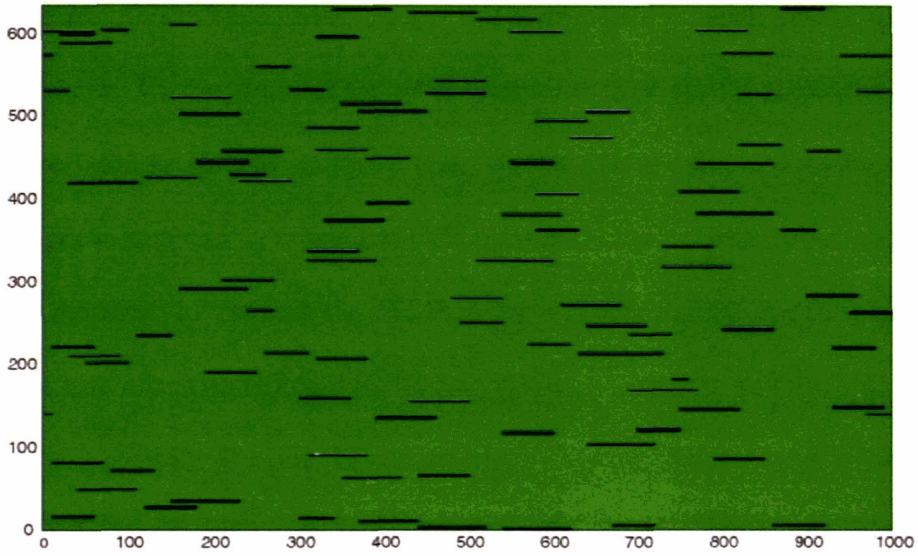

Figure 2.4 FEM realization of a RVE with random particle dispersion (dimension unit is nanometer).

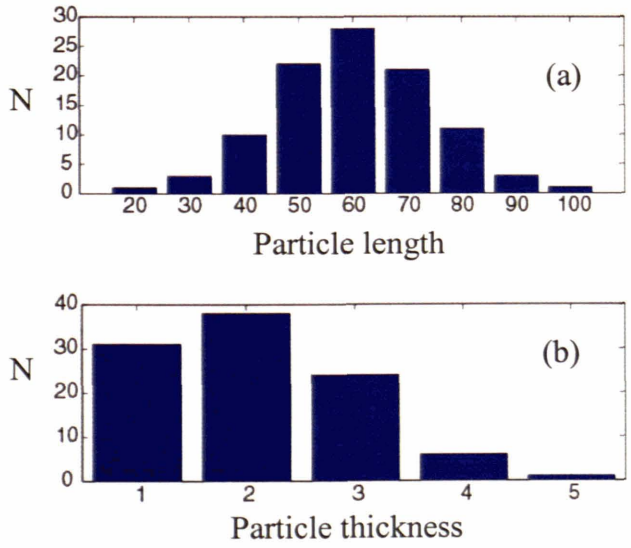

Figure 2.5 (a) Particle length distribution; (b) particle thickness distribution (N denotes the number of particles in the RVE that fall within corresponding dimension range).

Figure 2.4 shows a FEM realization of a 2-D RVE with random particle location distribution and various particle sizes. The corresponding distributions of particle length and thickness are plotted in Figure 2.5. All model parameters, including the variance of

the length/thickness distribution are controllable variables during the model generation process. In the generation of a "random" system as presented in Figure 2.8, a non-overlapping rule is imposed (i.e., no particle is allowed to be overlapped). Also, if a particle happens to cross the RVE boundary, the part emanating out of the RVE boundary is required to "enter" the RVE in the corresponding position required by the periodic continuation condition.

It is important to understand that our 2-D plane strain model is only an approximation of the 3-D geometry, as illustrated in Figure 2.6. More specifically, the real platelet-inclusions (in reality as well as in some of the micromechanical theories, such as the Eshelby-dilute model and the Mori-Tanaka-type model) have finite dimensions in all directions; however, in our model, the **particle itself has an unbounded dimension in the plane strain direction** (the 3-direction in Figure 2.6 b).

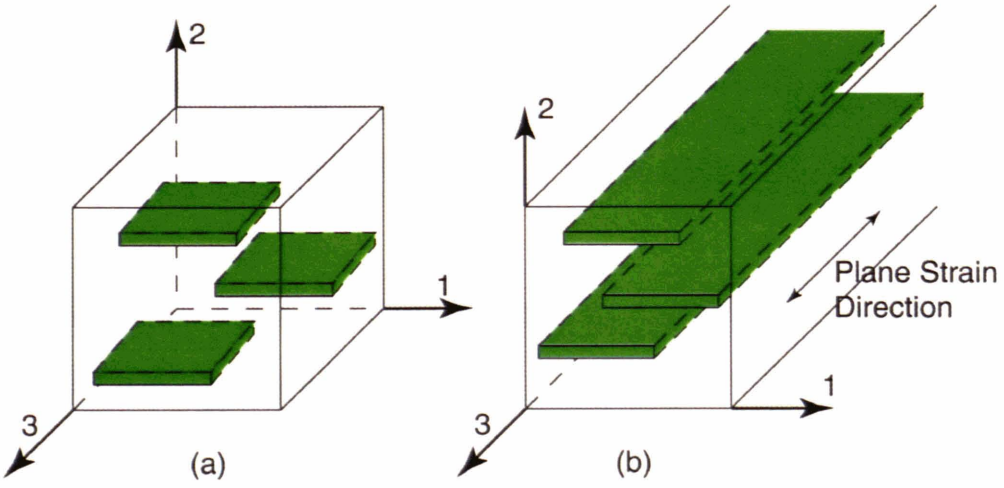

Figure 2.6 Schematic of RVEs: (a) 3-D; (b) 2-D plane strain.

2.3. Periodic Boundary Conditions

The RVEs are subjected to periodic boundary conditions expressed in terms of the macroscopic deformation gradient $\boldsymbol{F}$, where $\boldsymbol{F} = \boldsymbol{I} + \frac{\partial \boldsymbol{u}}{\partial \boldsymbol{X}}$ with $\boldsymbol{u}$ being the displacement vector and $\boldsymbol{X}$ being the reference position vector. For plane strain analysis, $F_{33} = 1$, $F_{13} = F_{23} = F_{31} = F_{32} = 0$:

$$\boldsymbol{F} = \begin{bmatrix} F_{11} & F_{12} & 0 \\ F_{21} & F_{22} & 0 \\ 0 & 0 & 1 \end{bmatrix}. \tag{2.1}$$

2.3.1. General Equations

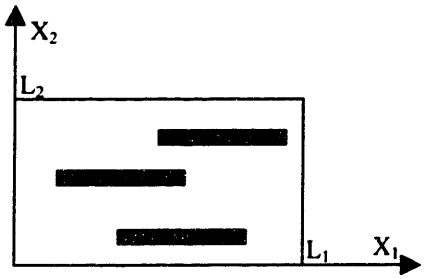

Figure 2.7 A schematic of a RVE

General periodic boundary equations for a two-dimensional RVE with a size of $L_1 \times L_2$, as illustrated in Figure 2.7, are developed as following:

$$u_1(X_1 = L_1, X_2) - u_1(X_1 = 0, X_2) = (F_{11} - 1)L_1 \tag{2.2}$$

$$u_2(X_1, X_2 = L_2) - u_2(X_1, X_2 = 0) = (F_{22} - 1)L_2 \tag{2.3}$$

$$u_1(X_1, X_2 = L_2) - u_1(X_1, X_2 = 0) = F_{12}L_2 \tag{2.4}$$

$$u_2(X_1 = L_1, X_2) - u_2(X_1 = 0, X_2) = F_{21}L_1 \tag{2.5}$$

2.3.2. Loading

Appropriate values of the components of $\boldsymbol{F}$ are imposed in order to achieve the desired macroscopic deformation under certain loading conditions. Two illustrative examples of the boundary conditions are given under loading of plane-strain uniaxial tension and simple shear loading respectively. Note that since only infinitesimal deformations are employed to study the overall elastic properties, we do not distinguish between the nominal stress/strain and the true stress/strain; i.e., the following macroscopic stress and strain calculations are all conducted with respect to the reference configuration.

2.3.2.1. Plane strain uniaxial Tension

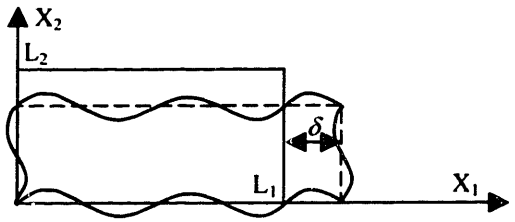

Figure 2.8 Schematic of a RVE under axial tensile loading

Figure 2.8 illustrates a deformed RVE under axial tensile loading in direction 1. F_{11}, the macroscopic stretch in the loading direction, is imposed to the RVE through the boundary condition:

$$u_1(X_1 = L_1, X_2) - u_1(X_1 = 0, X_2) = (F_{11} - 1)L_1 . \tag{2.6}$$

Macroscopic shear deformations are forbidden by imposing F_{12} and F_{21} to be zero:

$$F_{12} = F_{21} = 0 .$$

Note that F_{22}, the macroscopic stretch in direction 2 is left free to contract as the body undergoes the prescribed tensile stretch in direction 1.

The corresponding macroscopic strain is derived as:

$$\begin{cases} F_{11} \\ F_{12} = F_{21} = 0 \end{cases} \Rightarrow \delta = L_1(F_{11} - 1) \Rightarrow \bar{\varepsilon}_{11} = F_{11} - 1 = \frac{\delta}{L_1}, \tag{2.7}$$

where δ is the macroscopic average displacement in direction of tensile loading, and $\bar{\varepsilon}_{11}$ is the macroscopic nominal tensile strain.

2.3.2.2. Simple Shear

The macroscopic deformation gradient of an in-plane simple shear deformation illustrated in Figure 2.9 can be expressed as

$$\boldsymbol{F} = \begin{bmatrix} 1 & \gamma & 0 \\ 0 & 1 & 0 \\ 0 & 0 & 1 \end{bmatrix}, \tag{2.8}$$

where γ is the macroscopic shear strain.

Boundary condition:

$$u_1(X_1, X_2 = L_2) - u_1(X_1, X_2 = 0) = F_{12} L_2 \tag{2.9}$$

The macroscopic shear strain γ can be obtained from (2.9) as

$$\gamma = F_{12} = \frac{\delta}{L_2}, \tag{2.10}$$

where δ is the macroscopic average displacement of the top-edge relative to that of the bottom-edge, as marked in Figure 2.8.

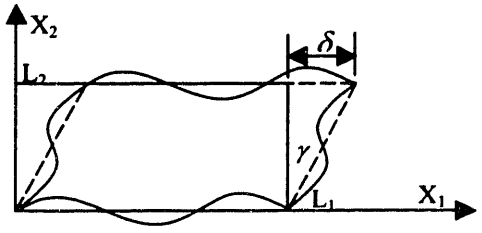

Figure 2.9 Schematic of a RVE undergoing macroscopic simple shear deformation.

2.4. Macroscopic Cell Response

The macroscopic response of the RVE is obtained through appropriate averaging over the stress and strain field of the whole body.

2.4.1. Average Strain

The components of the macroscopic deformation gradient are quantities that drive the deformation of the whole RVE (Eqs. (2.2) ~ (2.5)).

The macroscopic Green strain tensor can be calculated from

$$\boldsymbol{E} = \frac{1}{2}\left(\boldsymbol{U}^2 - \boldsymbol{I}\right) = \frac{1}{2}\left(\boldsymbol{F}^T\boldsymbol{F} - \boldsymbol{I}\right). \tag{2.12}$$

For infinitesimal strain ($|\boldsymbol{F} - \boldsymbol{I}| << 1$),

$$\boldsymbol{E} = 1/2\left[(\boldsymbol{F} - \boldsymbol{I}) + (\boldsymbol{F} - \boldsymbol{I})^T\right].$$

On the other hand, the macroscopic strain $\bar{\varepsilon}$ by definition is a volume average of the local strain over the whole RVE as given in (1.5).

It can be shown that, with the boundary conditions given in equations (2.2) to (2.5), the average strain calculated can be written in terms of the macroscopic deformation gradient $\boldsymbol{F}$. A proof in the axial tensile loading condition is given as an illustrative example. Refer to Figure 2.7, for convenience the left edge, right edge, top edge, and bottom edge of the RVE are denoted as L, R, T, and B respectively. Note that the proof is developed in the reference configuration since only small strain is concerned; consequently the surface normal $\boldsymbol{n}$ is measured in the reference configuration, e.g., $\boldsymbol{n}$ = (1, 0, 0) for the right-edge and $\boldsymbol{n}$ = (0, -1, 0) for the bottom-edge.

Proof:

$$\varepsilon_{11} = \frac{\partial u_1}{\partial X_1}$$

Divergence theorem, where n_i are the components of corresponding surface normal

$$\overline{\varepsilon_{11}} = \frac{1}{V}\int_V \varepsilon_{11} dV = \frac{1}{V}\int_V \frac{\partial u_1}{\partial X_1} dV = \frac{1}{V}\int_S u_1 n_1 dS$$

$$= \frac{1}{V}\int_{L+R+T+B} u_1 n_1 dS = \frac{1}{V}\int_{L+R} u_1 n_1 dS = \frac{1}{V}\left[\int_R u_1 dS - \int_L u_1 dS\right]$$

@ T and B, $n_1 = 0$; @R, $n_1 = 1$; @L, $n_1 = -1$

$$= \frac{1}{V}\left\{\int_{X_2=0}^{L_2} [u_1(X_1 = L_1, X_2) - u_1(X_1 = 0, X_2)] dX_2\right\}$$

$$= \frac{1}{V}\int_{X_2=0}^{L_2} (F_{11} - 1) L_1 dS = \frac{1}{V}(F_{11} - 1) L_1 L_2 = F_{11} - 1$$

B.C. ; 2D, $V = L_1 L_2$

Conclusion: $\overline{\varepsilon_{11}} = F_{11} - 1$.

2.4.2. Average Stress

The principle of virtual work (PVW) is used in order to calculate the overall mechanical response of the RVE. Danielsson (Danielsson, Parks and Boyce, 2002) derived the components of the macroscopic first Piola-Kirchhoff stress tensor $\overline{\boldsymbol{P}}$ in terms of the generalized reaction forces of three "imaginary nodes", the displacement components of which are related to the macroscopic deformation gradient $\boldsymbol{F}$. The macroscopic Cauchy stress tensor $\overline{\boldsymbol{T}}$ is calculated from $\overline{\boldsymbol{T}} = \overline{\boldsymbol{P}}\boldsymbol{F}^T / J$, where $J = \det \boldsymbol{F}$.

Here we adapt the same scheme to the frame of small strains. When only infinitesimal strains are concerned, the stress and strain tensors $(\boldsymbol{\sigma}, \boldsymbol{\varepsilon})$ are measured in the reference

configuration with volume V_0. The small strain tensor ε is defined as $\varepsilon = 1/2\left[\nabla \boldsymbol{u} + (\nabla \boldsymbol{u})^T\right]$, where $(\nabla \boldsymbol{u})_{ij} = \frac{\partial u_i}{\partial X_j}$. The small macroscopic deformation is now described with the **macroscopic displacement gradient** $\boldsymbol{D}$ ($\boldsymbol{D} = \boldsymbol{F} - \boldsymbol{I}$), defined as

$$\boldsymbol{D} = \frac{1}{V_0}\int_{V_0} \nabla \boldsymbol{u} dV;\ D_{ij} = \frac{1}{V_0}\int_{V_0} \frac{\partial u_i}{\partial X_j} dV. \tag{2.12}$$

$\boldsymbol{D}$ is related to the macroscopic strain $\bar{\varepsilon}$ (defined in Eq. (1.5) as $\bar{\varepsilon} = \frac{1}{V}\int_V \varepsilon(x) dV$) by

$$\bar{\varepsilon} = \frac{1}{2}\left(\boldsymbol{D} + \boldsymbol{D}^T\right). \tag{2.13}$$

Plane strain constraint requires $\frac{\partial u_i}{\partial X_3} = \frac{\partial u_3}{\partial X_j} = 0, \forall i, j$; thus the *plane-strain* $\boldsymbol{D}$ is

$$\boldsymbol{D} = \begin{bmatrix} D_{11} & D_{12} & 0 \\ D_{21} & D_{22} & 0 \\ 0 & 0 & 0 \end{bmatrix}. \tag{2.13}$$

PVW requires

$$\delta W^{\text{int}} = \delta W^{ext}. \tag{2.14}$$

External virtual work is the virtual work of surface traction

$$\delta W^{ext} = \int_{\partial\Omega_0} \boldsymbol{t} \cdot \delta \boldsymbol{u} dS = \int_{\partial\Omega_0} \boldsymbol{\sigma n} \cdot \delta \boldsymbol{u} dS. \tag{2.15}$$

Define the *plane-strain* macroscopic stress tensor $\bar{\sigma}$

$$\bar{\sigma} = \frac{1}{V_0}\int_{\Omega_0} \sigma dV = \begin{bmatrix} \bar{\sigma}_{11} & \bar{\sigma}_{12} & 0 \\ \bar{\sigma}_{12} & \bar{\sigma}_{22} & 0 \\ 0 & 0 & \bar{\sigma}_{33} \end{bmatrix}. \tag{2.16}$$

Since $\bar{\sigma}$ is work-conjugate to $\bar{\varepsilon}$, which is related to $\boldsymbol{D}$ via (2.13), the internal virtual work can be written in terms of $\bar{\sigma}$ and the macroscopic displacement gradient $\boldsymbol{D}$

$$\delta W^{\text{int}} = V_o \bar{\boldsymbol{\sigma}} : \delta \bar{\boldsymbol{\varepsilon}} = V_0 \bar{\boldsymbol{\sigma}} : \delta \left[1/2 \left(\boldsymbol{D} + \boldsymbol{D}^T \right) \right] \tag{2.17}$$

Due to the symmetry of $\bar{\boldsymbol{\sigma}}$, (2.17) can be further written as

$$\delta W^{\text{int}} = V_0 \bar{\boldsymbol{\sigma}} : \delta \boldsymbol{D} = V_0 \begin{bmatrix} \bar{\sigma}_{11} & \bar{\sigma}_{12} \\ \bar{\sigma}_{12} & \bar{\sigma}_{22} \end{bmatrix} : \delta \begin{bmatrix} D_{11} & D_{12} \\ D_{21} & D_{22} \end{bmatrix} \tag{2.18}$$

Since δW^{ext} is equal to δW^{ext} (PVW), we have

$$\delta W^{ext} = V_0 \begin{bmatrix} \bar{\sigma}_{11} & \bar{\sigma}_{12} \\ \bar{\sigma}_{12} & \bar{\sigma}_{22} \end{bmatrix} : \delta \begin{bmatrix} D_{11} & D_{12} \\ D_{21} & D_{22} \end{bmatrix} \tag{2.19}$$

Note that the components of $\boldsymbol{D}$ are imposed quantities in the finite element analysis, thus they are the external driver of the imposed deformation of the whole RVE. For convenience, introduce four *generalized degrees of freedom*, ξ_i (i = 1,...,4)

$$\begin{bmatrix} \xi_1 & \xi_2 \\ \xi_3 & \xi_4 \end{bmatrix} = \begin{bmatrix} D_{11} & D_{12} \\ D_{21} & D_{22} \end{bmatrix}. \tag{2.20}$$

ξ_i are assigned to the displacement components of two "auxiliary" nodes. By prescribing the value of ξ_i, the macroscopic deformation is imposed on the RVE. Now the external virtual work can be rewritten in terms of these generalized dof ξ_i and their work-conjugate, *generalized reaction forces*, r_i (i = 1,...,4):

$$\delta W^{ext} = \sum r_i \delta \xi_i = \begin{bmatrix} r_1 & r_2 \\ r_3 & r_4 \end{bmatrix} : \delta \begin{bmatrix} \xi_1 & \xi_2 \\ \xi_3 & \xi_4 \end{bmatrix} = \begin{bmatrix} r_1 & r_2 \\ r_3 & r_4 \end{bmatrix} : \delta \begin{bmatrix} D_{11} & D_{12} \\ D_{21} & D_{22} \end{bmatrix} \tag{2.21}$$

Equating (2.19) and (2.21), we have

$$\delta W^{ext} = V_0 \begin{bmatrix} \bar{\sigma}_{11} & \bar{\sigma}_{12} \\ \bar{\sigma}_{12} & \bar{\sigma}_{22} \end{bmatrix} : \delta \begin{bmatrix} D_{11} & D_{12} \\ D_{21} & D_{22} \end{bmatrix} = \begin{bmatrix} r_1 & r_2 \\ r_3 & r_4 \end{bmatrix} : \delta \begin{bmatrix} D_{11} & D_{12} \\ D_{21} & D_{22} \end{bmatrix}. \tag{2.22}$$

Hence the average stress is related to the generalized reaction force according to:

$$\begin{bmatrix} \bar{\sigma}_{11} & \bar{\sigma}_{12} \\ \bar{\sigma}_{12} & \bar{\sigma}_{22} \end{bmatrix} = \frac{1}{V_0} \begin{bmatrix} r_1 & r_2 \\ r_3 & r_4 \end{bmatrix}. \tag{2.23}$$

Chapter 3

Results under Axial Tensile Loading

Polymer matrix composites with high-aspect-ratio fillers, such as fibers and flakes, have been under study for half a century owing to their outstanding reinforcing efficiency. The fine fillers, which typically have a stiffness 2 orders of magnitude higher than the matrix, act to render a higher overall stiffness to the composite, while the relatively compliant and ductile polymer serves as matrix to bond all the particles and, more importantly, as a means to have load transferred to them.

Historically, the overall elastic properties of 2-phase composites have been treated mostly as an appropriate average of the individual phase properties, which generally overlooks local particle-particle interactions as well as the micro/nanoscale interaction between the molecules of the matrix and the embedded second-phase material. When the length scale of the filler approaches the nanoscale, it is reasonable to claim that this interaction effect is no longer negligible. However, the magnitude of the influence of the micro/nanoscale interaction on the dramatic enhancement of stiffness, as compared to the more conventional continuum reinforcing effects obtained by large-scale matrix homopolymer/particle composites, is still unclear. With this important mystery left unsolved, we try to predict the overall stiffness and explore the underlying physical mechanism from the perspective of continuum mechanics. Based upon the results of 2D plane strain finite element (FE) micromechanics simulations, the role of the interface interaction on stiffness enhancement will also be discussed.

3.1. Prediction of Effective Longitudinal Modulus

The approach to obtain the effective longitudinal modulus is summarized as following: 2D plane strain simulations of different microstructures are subjected to tensile loading parallel to the plane of the particles; appropriate periodic boundary conditions (Section 2.3.2.1) are applied to each RVE, and appropriate averaging (Section 2.4.3) over the stress field is conducted to obtain the overall response, which is then interpreted in terms of macroscopic properties.

In general, the overall reaction of a composite is an integrated reflection of the effects of various mutually independent factors. Here, using the 2D models illustrated in Figure 2.2 and Figure 2.3, we predict the effective longitudinal modulus as a function of particle volume fraction, particle aspect ratio, particle distribution (random vs. pattern) and the particle/matrix stiffness ratio.

$E_c/E_m = E_c/E_m$ (f_p, L/t, E_p/E_m, particle distribution)

Note that since plane strain elastic properties are generally different from the actual elastic constants, as shown in Appendix D, **all of the simulation results presented in this thesis are normalized with respect to corresponding plane strain properties of the matrix**. In this chapter, the calculated effective plane strain modulus, E_{11}^*, is normalized with respect to the matrix plane strain, E_m^*. For convenience, we do not use the '*' to specifically indicate a plane strain property in the remaining contents of this thesis.

Before the discussion of the results, a few basic concepts in the composite theory will be introduced. For the purpose of demonstration, the results of the "stacked" array system are used to interpret these concepts instead of the more realistic "random" structure.

Although hardly existing in the real world, the highly symmetric "stacked" system renders us the convenience to clarify important physical mechanisms and sheds light on the behavior of the more chaotic "random" system.

3.1.1. Basic Concepts

- **Load Transfer**

When a discontinuous-filler-composite is subjected to tensile loading, load is not directly applied to the particles; for particles with high aspect ratios, the load is transferred from the surrounding matrix to the particles mainly through matrix/particle interface shear stress. In particular, in order to transmit substantial levels of axial stress to the particles (and thus uses their full potential as reinforcing agents), the matrix will undergo substantial shear.

Figure 3.1 (d) and Figure 3.1 (c) show the simulation results of the distribution of the interface shear stress, τ_m, and the tensile stress in the particle, σ_p, with distance along the particle axis. The shear-distorted mesh surrounding the particle is shown in Figure 3.1 (b) (note that the undeformed mesh is a rectangular grid). The interface shear stress starts with a maximum at the ends of the particle, decreases rapidly with distance away from the ends and remains zero over the central portion of the particle; the tensile stress in the particle is relatively small at the ends and reaches the maximum at the points where interface shear stress vanishes.

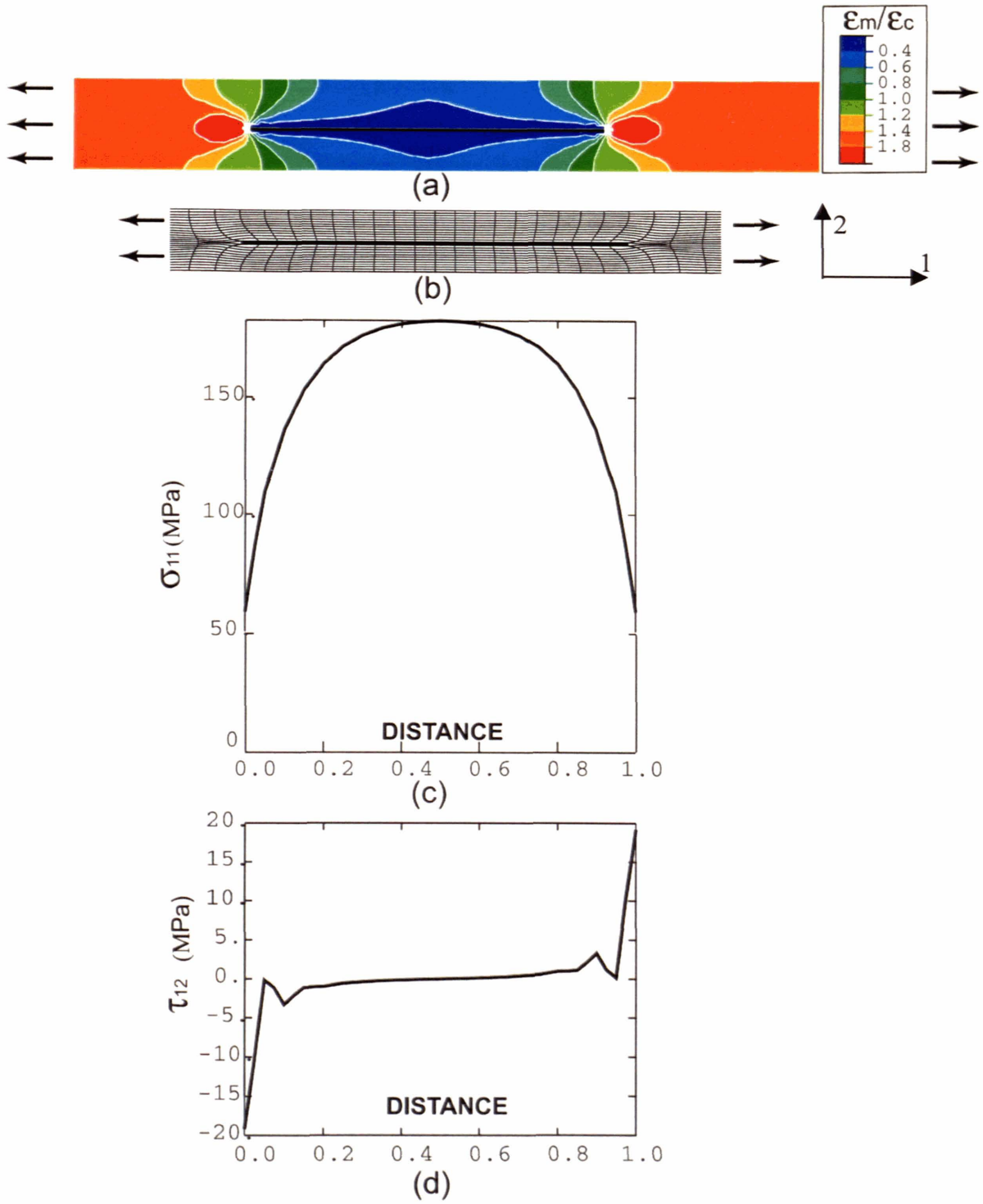

Figure 3.1 Results of a "stacked" array (f_p = 2%, L/t = 100, macroscopic strain ε_c = 0.5%): (a) Strain contour (normalized by ε_c) in the matrix adjacent to the particle; (b) Shear deformation in the matrix adjacent to the particle; (c) Tensile stress in the particle; (d) Shear stress along the matrix/particle top-interface.

- **Effective length**

We can see from Figure 3.1 (c) that the force carried by the ends is small compared to the central portion of the particle, where the tensile stress reaches its maximum value. The length of the central portion is consequently described as the "effective length" of the particle; while the short distance over which the maximum tensile stress is achieved is the so-called "load-transfer length" (Figure 3.2). Particles with longer effective length have a higher load carrying efficiency and thus have a better reinforcing capacity.

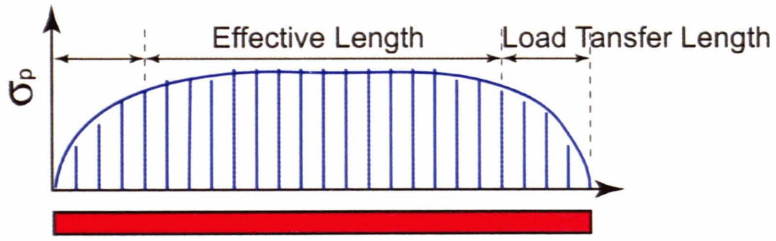

Figure 3.2 A demonstration of the "effective length" and the "load-transfer length".

The effective length of the particle can be affected by many factors such as the aspect ratio of the particle, the particle/matrix stiffness ratio, etc. More detailed study regarding the load transfer mechanism will be presented in section 3.2.1.

- **Strain shielding**

Another important phenomenon that has direct impact on the overall stiffness is the strain shielding taking place in the matrix material. Owing to the compatibility requirement, the axial strain in the matrix near the particle is very small (almost as low as the strain in the particle). When a particle is isolated (i.e., no particle-particle interaction), there is a zone surrounding the particle in which the matrix strain gradually recovers to the applied macroscopic strain, as is shown in Figure 3.3 (a). As particles start to interact with each

other, however, they penetrate into each other's "recovery zone" and shield the matrix in between them from straining.

The cause of such particle interaction usually comes from an increase in particle volume fraction or in the aspect ratio of the particle. However, for a "stacked" array system possessing fixed f_p and L/t, a change merely in the shape of the unit cell can easily result in the transition from an "isolated" strain state to a "highly shielded" one. Figure 3.3 (a) and (b) show the strain contours of two "stacked" systems under an applied macroscopic strain of 0.005. The width and the height of the unit cell are denoted as a and b, respectively. Both cases have a particle volume fraction of 1% and a particle aspect ratio of 50. Case 1 has a larger inter-particle spacing ($b = 50$) than case 2 ($b = 25$). It is clearly demonstrated in the strain contours of both cases, that the matrix material in the latter is shielded from straining due to the closeness of two particles, while in the former, the matrix is able to recover to the applied strain, and the particles are essentially isolated from each other.

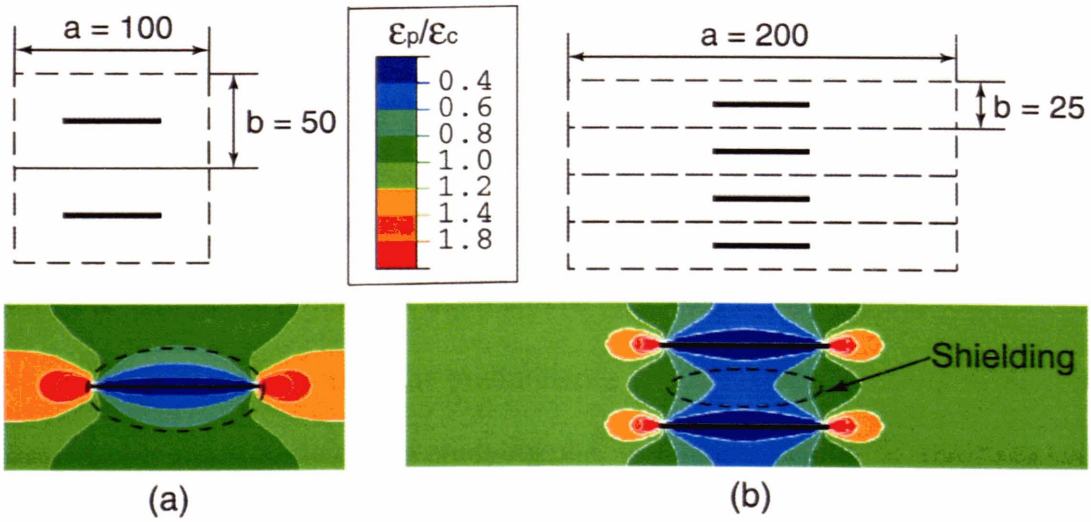

Figure 3.3 Strain contours (normalized by ε_c) of two "stacked" array systems ($v_p = 1\%$, $L/t = 50$, $\varepsilon_c = 0.5\%$). Size of unit cell: (a) 100×50, (b) 200×25. Dashed circle in (a): matrix strain recovery zone; dashed circle in (b): strain shielding zone.

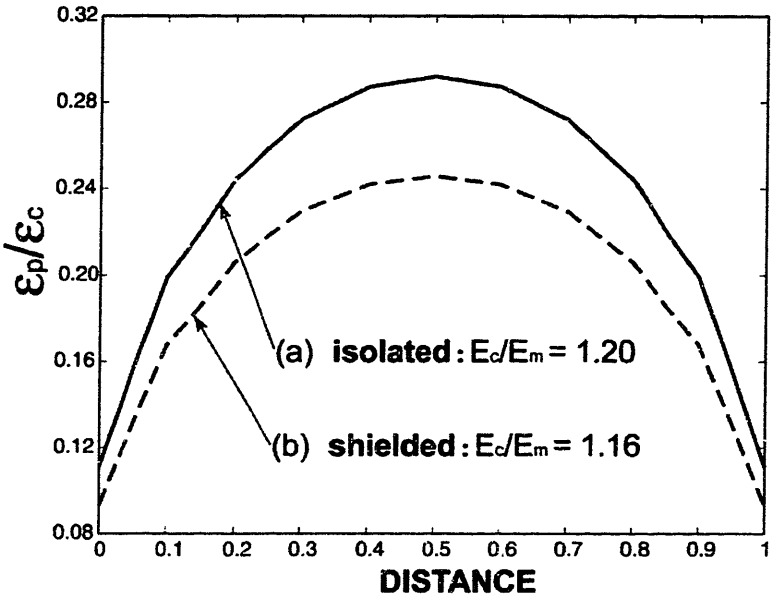

Figure 3.4 Strain distributions in the particle: solid line corresponds to the stacked array (a) in Figure 3.3; dashed line corresponds to the stacked array (b) in Figure 3.3.

Strain shielding has both positive and negative effects on stiffness enhancement: on one hand, the strain in the matrix is restrained; on the other hand, the efficiency of load transfer from matrix to particles is impaired due to the decrease in the matrix shearing, which is needed to build up the axial stress in the particles. The strain distributions in the particle for the two "stacked" array systems in Figure 3.3 are plotted in Figure 3.4, with E_c/E_m = 1.20 for the "isolated" structure and 1.16 for the "shielded" structure. Strain shielding lowers the maximum strain achieved in the particle, and in this case, lowers the stiffness reinforcing efficiency; more will be discussed in Section 3.3.

So far we have introduced some preliminaries about the reinforcement of discontinuous, large-aspect-ratio particles by studying the simulation results of the "stacked" array system. The following contents of this chapter, however, mainly focus on the more realistic "random" particle system. The effective stiffnesses of systems with randomly distributed, yet perfectly aligned particles are predicted as a function of various geometric

and material parameters. Relations between the enhanced stiffness and the underlying microscopic structures will be explored as well.

3.1.2. Effect of Particle Volume Fraction

Figure 3.5 depicts the prediction of the longitudinal modulus as a function of weight percent clay and clay aspect ratio for a random dispersion of clay particles. These results show the strong dependence on both filler weight fraction and aspect ratio.

Note that in order to compare with the Toyota experimental data (Toyota Central Lab, 1993), we need to convert the clay weight percentage (W_p), which is given as a material parameter, to our model parameter, clay volume fraction (f_p). Here the conversion ratio is taken to be $f_p/W_p = 0.4$, following Beall (2000); more regarding the conversion will be discussed later in Chapter 4, where the finite element results are compared with tensile experiment data.

The modulus is predicted to increase with increase in clay weight fraction. This increase is nonlinear: at higher weight fractions, the particles act to interfere with the efficiency of load transfer to the neighboring particles. These results also predict the very large influence that rather small filler loadings have on enhancing mechanical properties of polymer nanocomposites. The trends of the predictions are also highly consistent with experimental data in the literature, as shown in Figure 3.6.

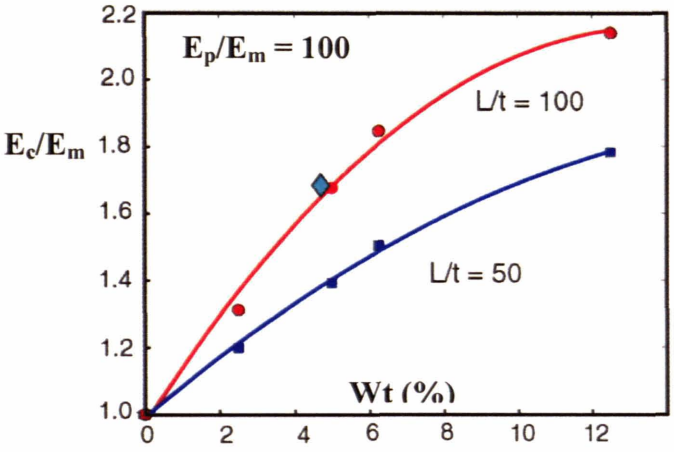

Figure 3.5 Dependence on clay content. Diamond mark: Toyota room-temperature test data on Nylon6-clay nanocomposite with $L/t = 100$, $E_m = 1.1$GPa.

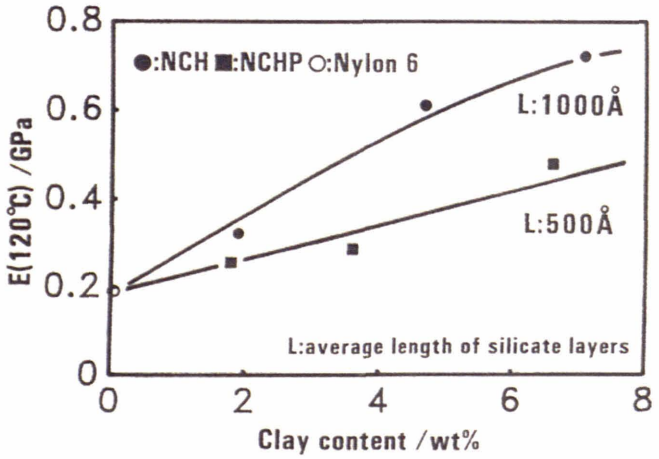

Figure 3.6 Toyota high-temperature test data (Toyota Central Lab, 1993)

3.1.3. Effect of Particle Aspect ratio

As shown in Figure 3.5, particles with larger aspect ratio have higher reinforcement efficiency. The effect of particle aspect ratio on the overall stiffness is studied by varying L/t while keeping the other parameters fixed, as plotted in Figure 3.7. It's clear that the normalized effective stiffness increases with increasing L/t, but the rate of increase decreases as L/t becomes larger.

The increase in E_c is a direct result of the improvement in load carrying efficiency as the particle aspect ratio increases. Figure 3.8 shows the strain distributions in particles with various aspect ratios (note that the particles are of uniform length and thickness in each RVE; the distribution is an average over all of the particles in a RVE). While the load transfer length is more-or-less the same for different aspect ratios, particles with larger aspect ratios tend to have a longer effective length and a higher maximum strain (In the extreme case of a continuous particle, the particle longitudinal strain ε_p becomes the same as the macroscopic longitudinal strain ε_c.). The average particle stress is defined as

$$\overline{\sigma_p} = \frac{1}{L}\int_L \sigma_p(x)dx, \tag{3.1}$$

and is calculated for each L/t, as plotted in Figure 3.9. Recall the relationship between the overall average stress and the particle stress given in equation 3.4; the nonlinear dependence of particle average stress on particle aspect ratio is the cause of the similar nonlinear dependence of the overall stiffness, shown in Figure 3.7 as discussed earlier.

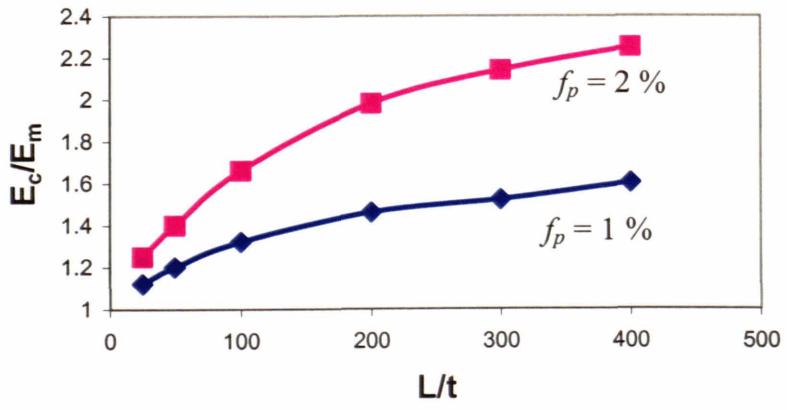

Figure 3.7 Dependence of E_c/E_m on particle aspect ratio ($\varepsilon_c = 0.005$, $E_p/E_m = 100$).

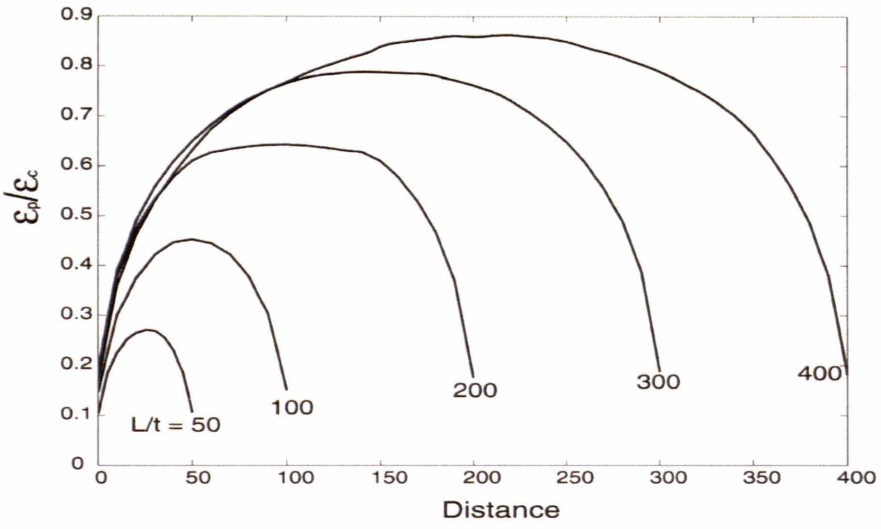

Figure 3.8 Particle strain distribution (averaged over all particles) for L/t = 25, 50, 100, 200, 300, 400 ($\varepsilon_c = 0.005, f_p = 2\%, E_p/E_m = 100$).

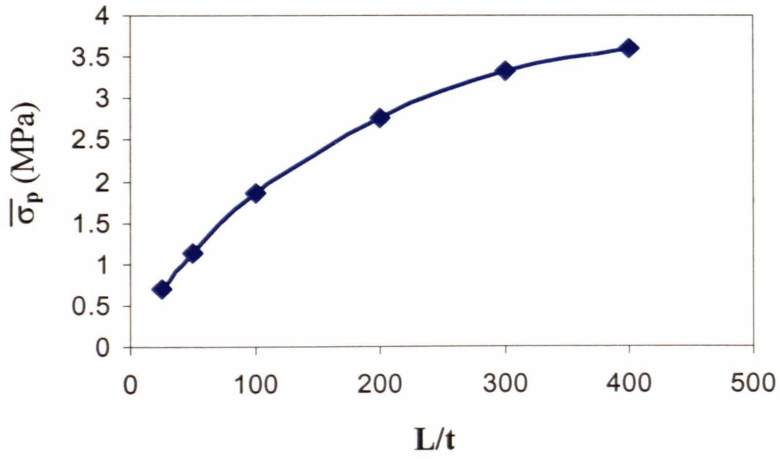

Figure 3.9 Dependence of average particle stress on particle aspect ratio ($\varepsilon_c = 0.005, f_p = 2\%, E_p/E_m = 100$).

We can have a better understanding of the role of particle aspect ratio by calculating the particle average stress from an idealized particle stress distribution as shown in Figure 3.10.

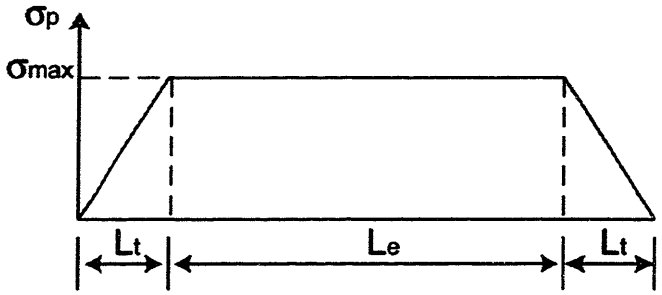

Figure 3.10 Idealized stress distribution in the particle. L_e is the effective length; L_t is the load transfer length.

The average particle stress can be calculated as:

$$\begin{aligned}\overline{\sigma_p} &= \frac{1}{L}\int_L \sigma_p(x)dx \\ &= \left[(L-2L_t)\,\sigma_{\max} + L_t\sigma_{\max}\right]/L = \sigma_{\max}\left(1-\frac{L_t}{L}\right)\end{aligned} \tag{3.2}$$

When L is large enough, both the load transfer length L_t and the maximum particle stress σ_{max} can be treated as constants (σ_{max} approaches $E_p\varepsilon_c$, the extreme case of continuous particle). Considering a fixed particle thickness, we can easily differentiate the average particle stress with respect to particle length

$$\frac{d\overline{\sigma_p}}{dL} = \frac{(\sigma_{\max}L_t)}{L^2}. \tag{3.3}$$

While $\overline{\sigma_p}$ increases with L, the rate of increase decreases, and will eventually stop ($\underset{L\to\infty}{Lim}\frac{d\overline{\sigma_p}}{dL} = 0$). Consequently, the overall stiffness of the composite will saturate with increasing particle length.

3.1.4. Effect of the Particle/Matrix Stiffness Ratio

The particle/matrix stiffness ratio E_p/E_m has always been an important parameter in the prediction of overall stiffness. The so-called "rule of mixtures" predicts a linear relationship between E_c/E_m and E_p/E_m as:

$$E_c = f_p E_p + f_m E_m \text{ or } \frac{E_c}{E_m} = f_p \frac{E_p}{E_m} + f_m . \tag{3.4}$$

However, this is only an upper bound for E_c. Results from simulations exhibit a large deviation from it. In Figure 3.11, E_c/E_m is plotted as a function of E_p/E_m while the particle volume fraction and aspect ratio are kept as constants. The two curves, with particle volume fractions of 1.88% and 2.50%, respectively, show similar nonlinear dependence of the effective stiffness on the ratio of E_p/E_m, other than the linear relationship predicted by the mixing law. It is clear from the figure that the effective stiffness, which increases

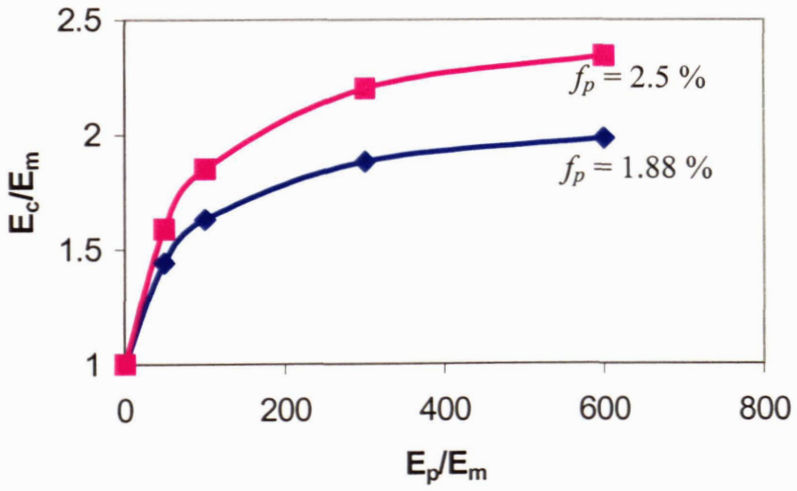

Figure 3.11 Dependence of E_c/E_m on the ratio of E_p/E_m ($L/t = 100$)

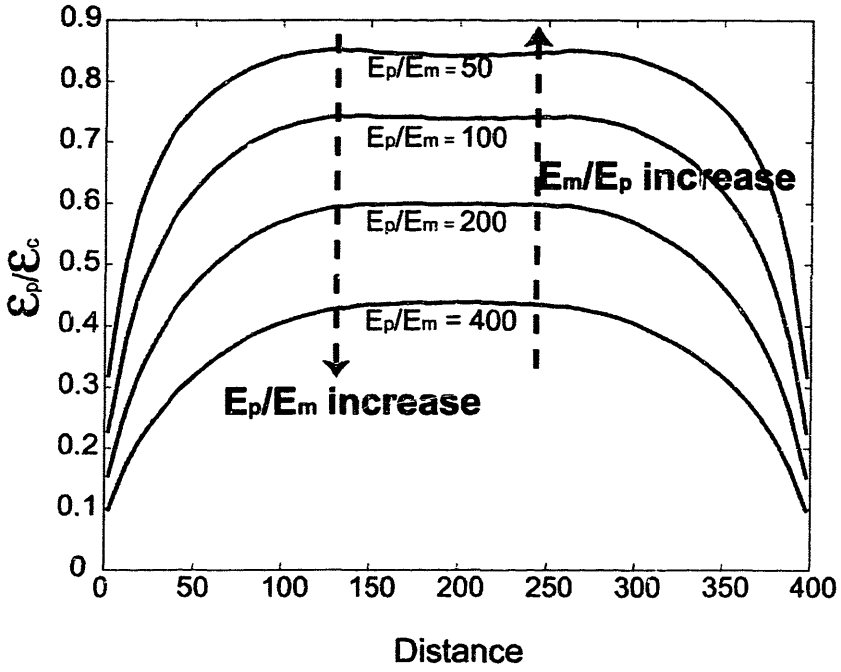

Figure 3.12 Strain distribution along interface (averaged over all the particles) (ε_c = 0.005, v_p = 1%, L/t = 400). The plotted strain is normalized with the applied macroscopic strain ε_c.

almost linearly at the beginning of the increase of E_p/E_m, enters a plateau when the ratio of E_p/E_m reaches a critical value (~200 for both volume fractions) and keeps growing slowly until it saturates. Although the critical value of E_p/E_m seems unaffected by the particle volume fraction, the ultimate value of the effective stiffness is largely dependent on it.

The forming of the plateaus in Figure 3.11 can be explained by examining the stress/strain distributions in the particle. As the ratio of E_p/E_m increases (i.e., E_m/E_p decreases), both the effective length and the maximum strain in the particle drop, as shown in Figure 3.12. When the particle modulus E_p is fixed, higher E_p/E_m implies lower matrix modulus E_m, and consequently lower shear modulus of the matrix (for isotropic material, shear modulus $G = E/(1-2v)$, where v is Poisson ratio). As previously discussed,

the load applied to the composite is transferred from the matrix to the particle through the interfacial shear stress. Lowered shear modulus of the matrix requires longer load transfer length in order to build up the same amount of maximum stress in the particle. It will also be shown later in the shear-lag analysis, that a high ratio of G_m/E_p is desirable for better stiffness reinforcing result.

3.1.5. Effect of Particle Distribution

The random dispersion of particles in the polymer/layered-silicate nanocomposites has long been recognized by morphology studies. Further more, the orientation of the particles is intrinsically a random factor as well: while intercalated systems possess a locally preferred orientation, the exfoliated systems do not have one. Hence, to model the real structure with some well-packed particle arrays that not only have perfect alignment but also exhibit regular patterns is a really rather extreme simplification. However, considering the simplicity of the patterned structures (only one unit cell containing one particle is needed in a simulation due to the periodicity of the structure) the regular patterned structures are worthy of our attention.

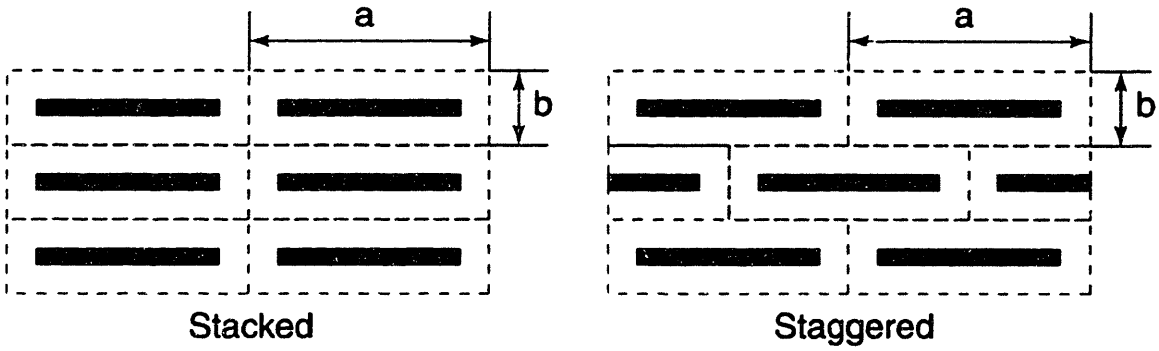

Figure 3.13 Schematic of the structure of "stacked" array and "staggered" array

The two types of pattern under our concern are the so-called "stacked" and "staggered" arrays. A schematic of these structures are drawn in Figure 3.13, where "a" and "b" set the horizontal and vertical inter-particle spacing respectively.

When the particle volume fraction and aspect ratio are fixed, the shape of the unit cell becomes an additional parameter:

$$f_p = \frac{Lt}{(ab)},$$

$$\frac{b}{a} = \left(\frac{L}{a}\right)^2 \Big/ \left[f_p\left(\frac{L}{t}\right)\right]. \tag{3.5}$$

In order to study the effect of the shape of the unit cell on the overall behavior, a series of models are generated with various ratios of a/L for fixed f_p and L/t. The simulation results are depicted in Figure 3.14. While the results of both deviate from the result of the random structure, the "stacked" and "staggered" systems behave rather differently from each other. Furthermore, even within one particular pattern, the overall stiffness is largely affected by the shape of the unit cell (i.e., the change in a/L). For both "stacked" and "staggered" arrays, the overall stiffness decreases with an increase of a/L.

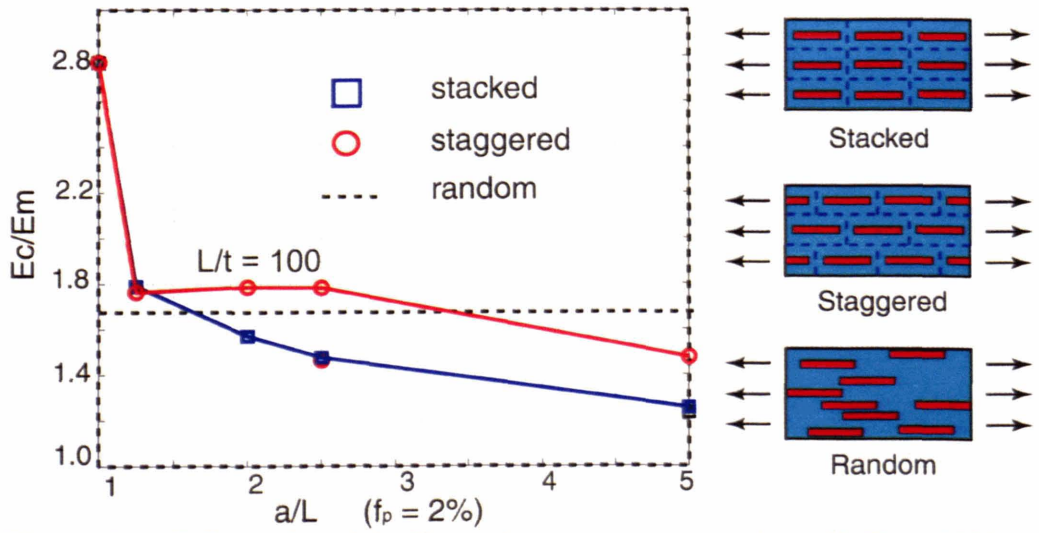

Figure 3.14 Effect of particle dispersion (pattern vs. random, $E_p/E_m = 100$).

Two extreme cases, when $a/L = 1$ or $a/L >> 1$, are illustrated in Figure 3.15(1) and (2). The two extremes correspond to the upper and lower bounds respectively. In the former condition, the strains in the particle and the matrix are equal, giving $E_c = f_p E_p + f_m E_m$. While in the latter case, the equal quantity is the stress, giving $\frac{1}{E_c} = \frac{f_p}{E_p} + \frac{f_m}{E_m}$.

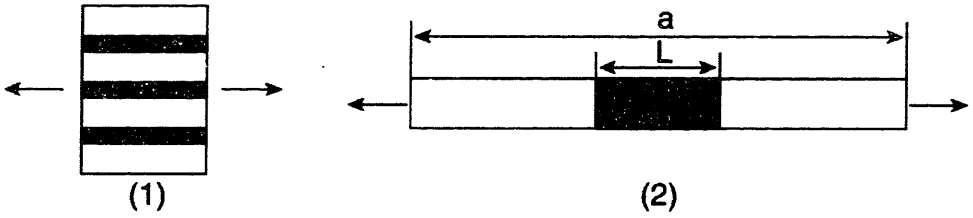

Figure 3.15 Two extreme cases of the unit cell: (1) $a = L$; (2) $a << L$.

Another noticeable observation from Figure 3.14 is that, for a fixed value of a/L (slightly greater than one) the "staggered" structure is more efficient than the "stacked" in terms of the longitudinal stiffness enhancement. The strain contours of both structures with the same size of unit cell are shown in Figure 3.16, together with the strain contour of a random structure. All three possess the same particle volume fraction, particle aspect ratio, and are subjected to the same amount of applied macroscopic strain. It is clear from the contours that the large areas of matrix unaffected by the particles in the "stacked" structure enable the compliant matrix to deform and thus cost it the efficiency in stiffness enhancement.

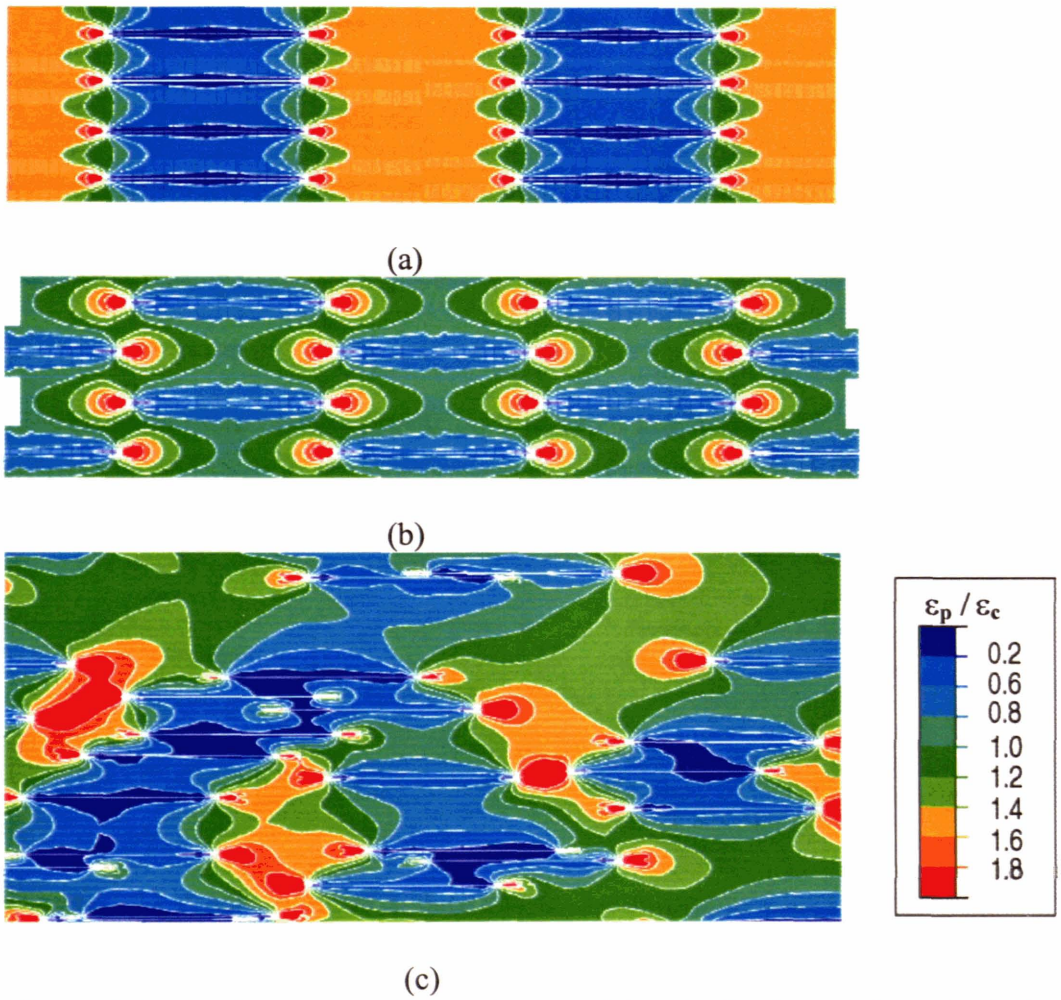

Figure 3.16 Strain contours for various particle distributions: (a) stacked, (b) staggered, (c) random. For (a) and (b), $a/L = 2$.

In summary, with fixed values of L/t, f_p, and E_p/E_m, the structure of "staggered" array with a small a/L is the most desirable dispersion of particle as far as the overall longitudinal stiffness is concerned.

3.2. Stiffness Enhancement Mechanism

Two major mechanisms governing the dramatic enhancement in the longitudinal stiffness, load transfer and strain shielding, will be discussed here.

3.2.1. Load Transfer Mechanism

3.2.1.1. Simple Analysis

The idea of load transfer and a few related concepts such as the effective length and transition length have been introduced at the beginning of this chapter. The tensile stress distribution in the particle can be calculated from a simple force equilibrium analysis on a free body diagram of the particle, as illustrated in **Figure 3.17**.

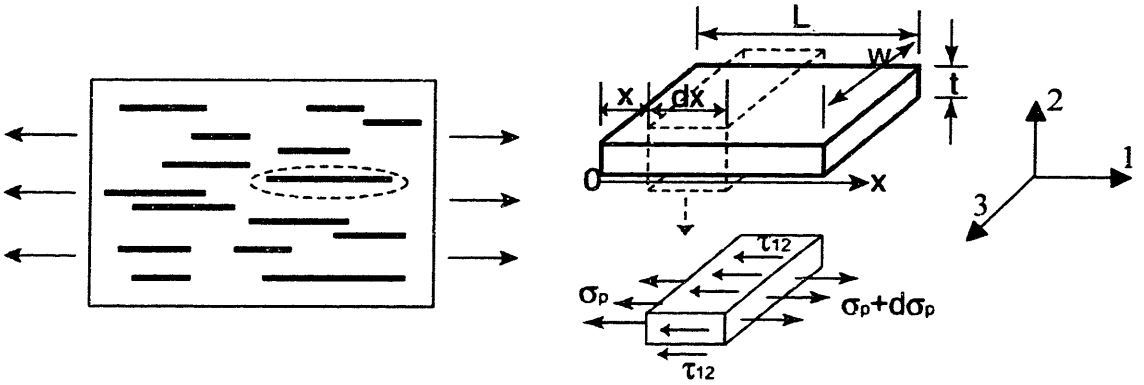

Figure 3.17 A schematic of a matrix with discontinuous fillers under axial tensile loading

Consider a square-shaped flake with a width of W and a thickness of t. By simple force balance we have,

$$\tau_{12} A_s = d\sigma_p A \ , \tag{3.6}$$

where τ_m is the shear stress on the matrix/particle interface, σ_p is the tensile stress in the particle, A_s and A are the surface area and the cross-section area, respectively

$$A_s = 2(W + t)dx, \quad A = Wt \tag{3.7}$$

Take (3.7) into (3.6), we have

$$\frac{d\sigma_p}{dx} = 2\left(\frac{W + t}{Wt}\right)\tau_{12} \tag{3.8}$$

For simple analysis, assume that the interface shear stress is constant. With the constant shear stress assumption and ignoring the tensile stress at the ends (since it is rather small compared to the maximum stress that can be built up to), we have

$$\sigma_p = 2\left(\frac{W+t}{Wt}\right)\tau_{12}x\,. \tag{3.9}$$

Figure 3.16 shows the stress distribution given in (3.9), where the maximum particle stress is achieved over the load transfer length L_t. Since the maximum strain in the particle approaches ε_c, the macroscopic composite strain, as the particle aspect ratio becomes larger (as shown in Figure 3.8), we assume the maximum tensile stress in the particle to be a constant, i.e., $(\sigma_p)_{\max} = E_p\varepsilon_c$. From (3.9), the load transfer length can be obtained as

$$L_t = \frac{(\sigma_p)_{\max}}{\tau_{12}}\cdot\left(\frac{2Wt}{W+t}\right) = \frac{(\sigma_p)_{\max}}{\tau_{12}}\cdot\frac{2t}{1+t/W}\,. \tag{3.10}$$

Note that since $W >> t$ in plane strain analysis (which is our case), (3.10) can be simplified as

$$L_t \approx \frac{(\sigma_p)_{\max}}{\tau_{12}}\cdot 2t \tag{3.11}$$

However, when both the particle and the matrix are in the elastic state and the particle-matrix bond is not broken, the shear stress is not a constant, but varies with distance along the particle. Here I'd like to introduce the well-known shear lag models. Although the models are built upon short fibers instead of the flake-like particles in our interest, some results of the shear lag analysis can still serve as assistance to our understanding of the physics underneath as well as a guideline for the analysis of our simulation results.

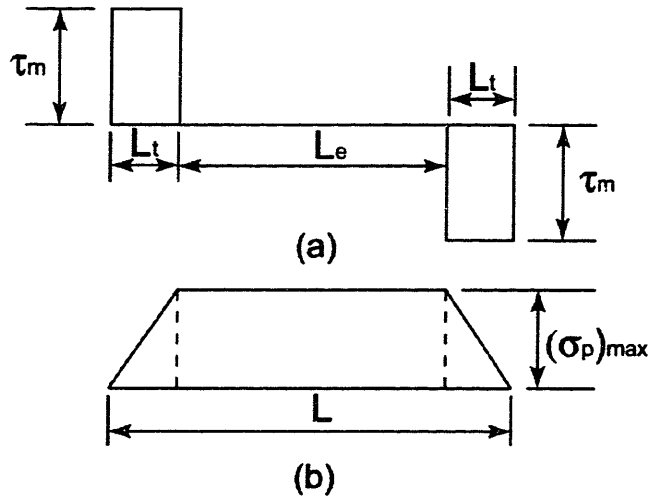

Figure 3.18 Idealized stress distribution

3.2.1.2. A Brief Review on Shear-lag Analysis

Following Cox (Cox, 1952), the shear-lag analysis focuses on a single fiber with a radius of r_f embedded in a cylindrical matrix with an outer radius of R, as shown in Figure 3.19. It is assumed that the axial strain on the outer surface of the matrix cylinder is the overall average strain ε_c. Axial equilibrium of the fiber requires that

$$\frac{d\sigma_f}{dz} = -\frac{2\tau}{r_f}, \tag{3.12}$$

where σ_f is the axial fiber stress, τ is the interface shear stress. Assuming that the shear stress in the matrix is proportional to the difference in the axial displacement between the fiber and the matrix, Cox was able to calculate the fiber stress distribution and the interface shear stress:

$$\sigma_f = E_f \varepsilon_c \left[1 - \frac{\cosh \beta(l_f/2 - z)}{\cosh \beta l_f/2} \right], \tag{3.13}$$

$$\tau = \frac{1}{2} E_f \varepsilon_c \beta r_f \left[\frac{\sinh \beta(l_f/2 - z)}{\cosh \beta l_f/2} \right], \tag{3.14}$$

$$\beta = \sqrt{\frac{2G_m}{E_f r_f^2 \ln(R/r_f)}}, \tag{3.15}$$

where E_f is the fiber modulus, G_m is the matrix shear modulus.

The matrix radius R is determined by

$$\frac{R}{r_f} = \sqrt{\frac{K_R}{\phi}} \tag{3.16}$$

where ϕ is the fiber volume fraction, and K_R is a constant that depends on the packing of fibers.

The distributions of tensile stress and shear stress given in (3.13) and (3.14) are plotted in Figure 3.20 (a) and (b), respectively. The ratio of G_m/E_f is varied to demonstrate the influence of parameter β on the fiber stress, while the other parameters are fixed. In particular, K_R in (3.22) is taken to be 0.907 for hexagonal fiber packing (Rosen, 1964 and 1965). With a fixed fiber length, both the effective length of the fiber and the maximum fiber stress increase with increasing β. This suggests that not only a large aspect ratio of the fiber but also a high ratio of G_m/E_f is desirable for reinforcing a discontinuous fiber composite.

Recalling the discussion regarding the effects of particle aspect ratio and particle/matrix stiffness ratio in Section 3.1.3 and 3.1.4, analyses based on 2D FE simulations of our polymer-clay nanocomposite models have led to similar conclusions (Figure 3.8 and Figure 3.12).

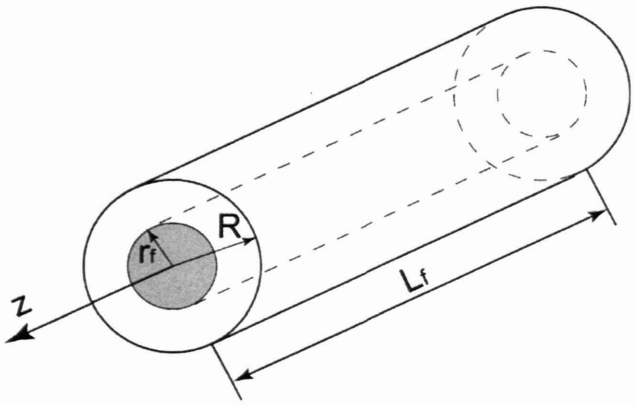

Figure 3.19 Shear lag model: idealized geometry

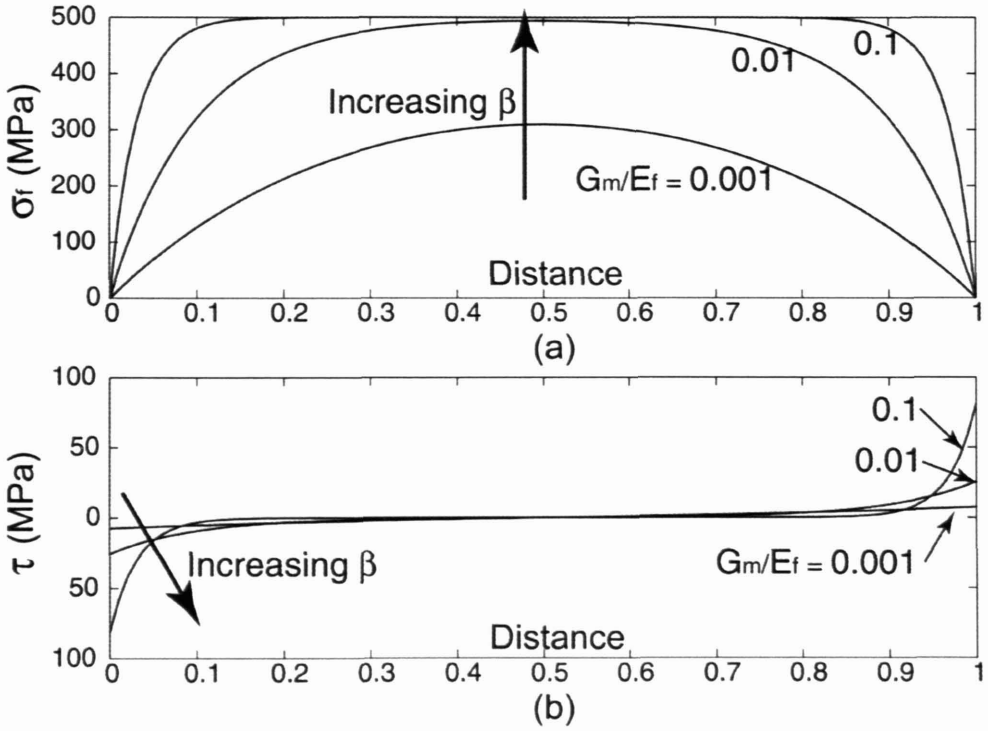

Figure 3.20 Shear lag model: (a) particle tensile stress distribution; (b) interface shear stress distribution (parameters used in (3.19) to (3.22) are: E_f = 100 Gpa, ϕ = 2%, r_f = 1 nm, l = 100 nm, ε_c = 0.005; number on each curve indicate the ratio of G_m/E_f).

3.2.1.3. Factors Influencing Load-Transfer Efficiency

The average stress of the particle is an important parameter in determining its efficiency in load carrying. Recall that the effective stiffness is defined as a mapping between the

overall average stress and average strain (equation 3.6); given a fixed macroscopic strain, a larger $\overline{\sigma_p}$ results in a larger overall stiffness (the overall average stress of the composite is dominated by $\overline{\sigma_p}$, due to the high stiffness contrast between the matrix and the particle).

We have calculated $\overline{\sigma_p}$ as a function of $(\sigma_p)_{max}$ and L_t from the idealized stress distribution while examining the effect of particle aspect ratio on the overall stiffness (equation 3.8). However, that expression is only valid for cases where particles have at least a critical length L_c ($L_c = 2L_t$). If the particle length is less than L_c, the stress in particle cannot fully build up to its maximum, as illustrated in Figure 3.21. These particles have a zero effective length and consequently cannot carry the load efficiently.

Now let us focus on longer particles ($L>L_c$). Take the expression of L_t given in (3.17) into (3.8), we have

$$\overline{\sigma_p} = (\sigma_p)_{\max}\left[1 - \frac{(\sigma_p)_{\max}}{\tau_{12}} \cdot 2\left(\frac{t}{L}\right)\right]. \tag{3.21}$$

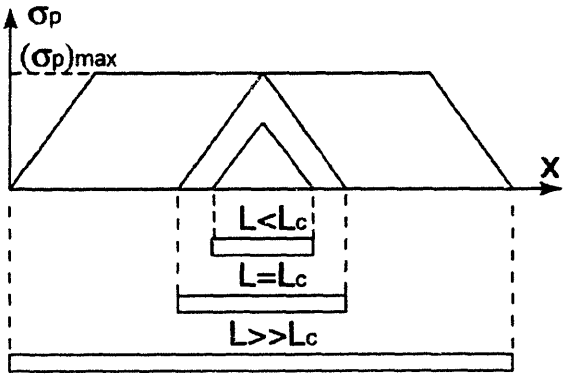

Figure 3.21 Effect of particle aspect ratio on the load transfer efficiency

Assuming the maximum particle stress to be constant, we have the following observations from equation 3.21:

- For a fixed interface shear stress τ_{12}, $\overline{\sigma_p}$ increases with the increase of particle aspect ratio, L/t;
- For a fixed L/t, $\overline{\sigma_p}$ increases with the increase of the interface shear stress τ_{12}, i.e., when the particle stiffness E_p is fixed (in order for $(\sigma_p)_{max}$ to be constant) $\overline{\sigma_p}$ increases with the matrix shear modulus G_m.

The above observations well illustrate the effect of L/t and E_p/E_m on the effective stiffness of the composite, discussed in 3.1.3 and 3.1.4. The conclusion is, in order for particles to carry load efficiently, larger particle aspect ratio and high matrix/particle stiffness ratio are desired.

3.2.2. Strain Shielding Mechanism

As introduced in 3.1.1, strain shielding in the matrix is another important factor that affects the overall properties of the composite. Increases in particle volume fraction or particle aspect ratio both raise the chance of particle interaction, and hence improve the efficiency of the particle in shielding the matrix from straining.

However, shielding of the matrix alone cannot result in the dramatic enhancement of stiffness. It is important not to overlook the effect of strain shielding on the efficiency of load transfer. In the previous discussion we have seen how the particle stress decreases with decrease in the vertical inter-particle spacing of a "stacked" array (Figure 3.4). The particles shield the matrix from straining at the cost of the efficiency of the matrix in

transferring the load to the particles. This conclusion is well supported by the strain contour of a system with random particle dispersion shown in Figure 3.22. Three typical particle states in terms of their relative positions are marked with red circles: (a) isolated; (b) partly overlapped by other particles; (c) completely overlapped by other particles. The corresponding strain distribution in each particle demonstrates the strong influence of particle interaction on the efficiency of load transfer: in an "isolated" particle, the stress/strain builds up fully to its maximum; in a particle of state (c), the strain can only develop to half of the maximum strain developed in (a), due to the impaired capacity of the severely shielded matrix to transfer load to the particle; in a particle of state (b), the half overlapped by another particle has lower strain compared to the other half.

The negative impact of matrix strain shielding on load transfer is also one of the factors responsible for the nonlinear dependence of the effective stiffness on particle volume fraction (Figure 3.5) and particle aspect ratio (Figure 3.7).

As can be observed from the strain contour, the strains in the interfacial areas (marked with white rectangular boxes in Figure 3.23) are generally small compared to the applied strain. A deduction from this observation is that the special morphology of polymer surrounding the particle probably does not have a large impact on the overall result. The reason being that, even if the longitudinal stiffness of the polymer within the interfacial areas increases by a few times due to the constrained chain morphology, the increase of modulus in a region with low strain won't be of much help to the average stress, and as a result, won't have a large effect on the overall stiffness of the composite. Another concern regarding the influence the special interfacial-area chain morphology has on the dramatic stiffness enhancement is that, although the highly oriented chains might increase

longitudinal stiffness, they might also tend to reduce the local shear modulus of the matrix, resulting in lowered matrix load transfer ability (Section 3.2.1.3), and thus may not have as large an impact on the stiffness enhancement as suspected. However, study on these nanocomposite systems will not stop at the composite-level explanations. The role of the matrix morphology in contributing to property enhancement will be put under investigation in future work, particularly, with regard to the properties of the matrix and how these enhance load transfer to the particles.

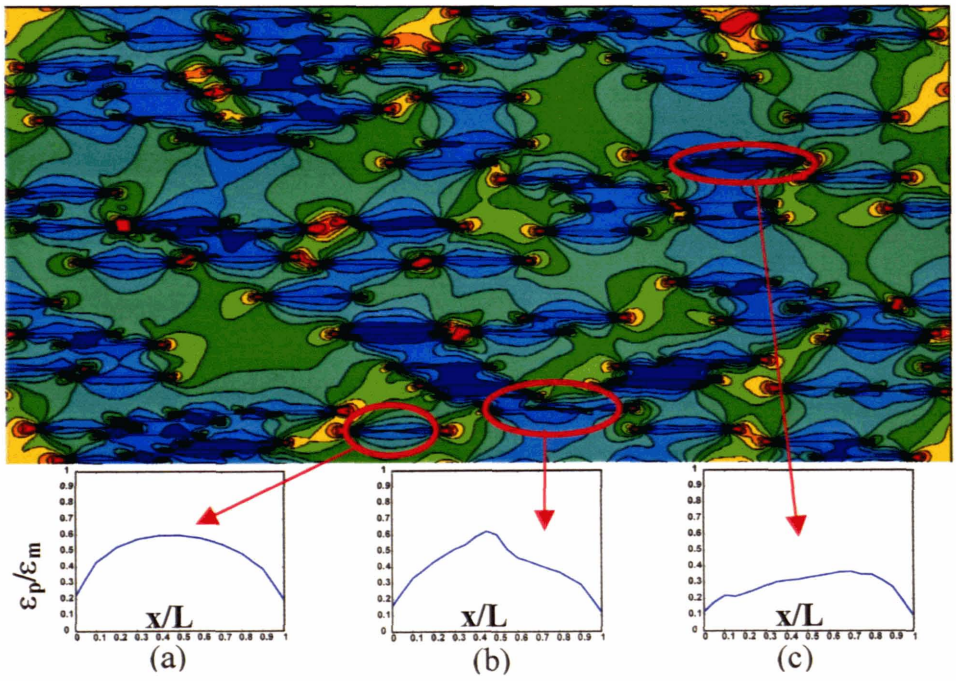

Figure 3.22 The effect of strain shielding on particle strain/stress distribution.

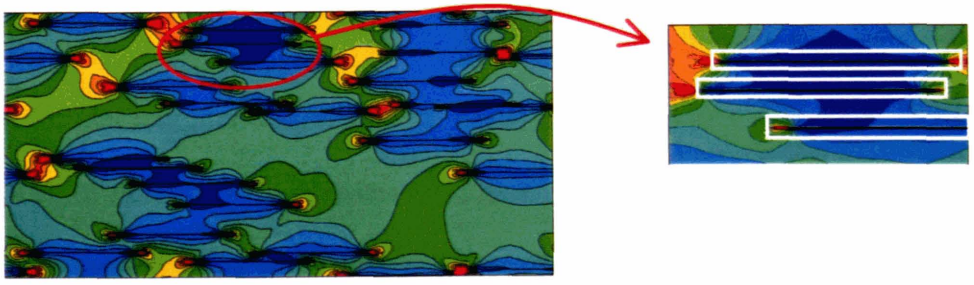

Figure 3.23 Low-strain interfacial areas.

Chapter 4

The Clay Particle

It has been shown in the previous chapter that the macroscopic stiffness of the polymer/nanoclay composite is strongly dependent on the particle aspect ratio (Fig 3.5), the particle volume fraction (Fig 3.7), and the elastic properties of the particle (Fig 3.11); however these important aspects of the nanoclay have yet to be consistently and accurately defined thus far. It is the task of this chapter to give some insight to the internal structure of the clay particle and upon which, make estimations of its properties that are of crucial importance to the macroscopic mechanical properties of the nanocomposite.

Previously, the clay particle has been treated as one continuous entity. This is a reasonable representation of the particle in a morphology of complete exfoliation, where single silicate layers are dispersed in a polymer matrix; however, in an intercalated or partially exfoliated structure, a primary particle actually consists of several individual silicate layers with an inter-layer spacing of a few nanometers. Figure 4.1 shows two TEM images of MXD6 nylon/clay nanocomposite with 5.1 wt % clay: the layered structure of the particles, which appear to be continuous in (a), can be clearly identified in (b) under a higher magnification. Analysis of the X-ray diffraction (XRD) pattern (Figure 4.2) of this nanocomposite reveals a ~3-layer-crystalline structure with an average interlayer spacing of 4.1 nm; in contrast, the average organo-clay crystallite before intercalation has ~4 layers and an interlayer spacing of 2.4 nm (Lee and McKinley,

2002). For such intercalated morphology, we consider the basic reinforcing clay particle to include the multiple silicate layers *and* the interlayer gallery material as the basic element to model when assessing the influence of nanoclay particles on nanocomposite properties. Therefore it is of crucial importance to determine the effective properties of this so-called "particle".

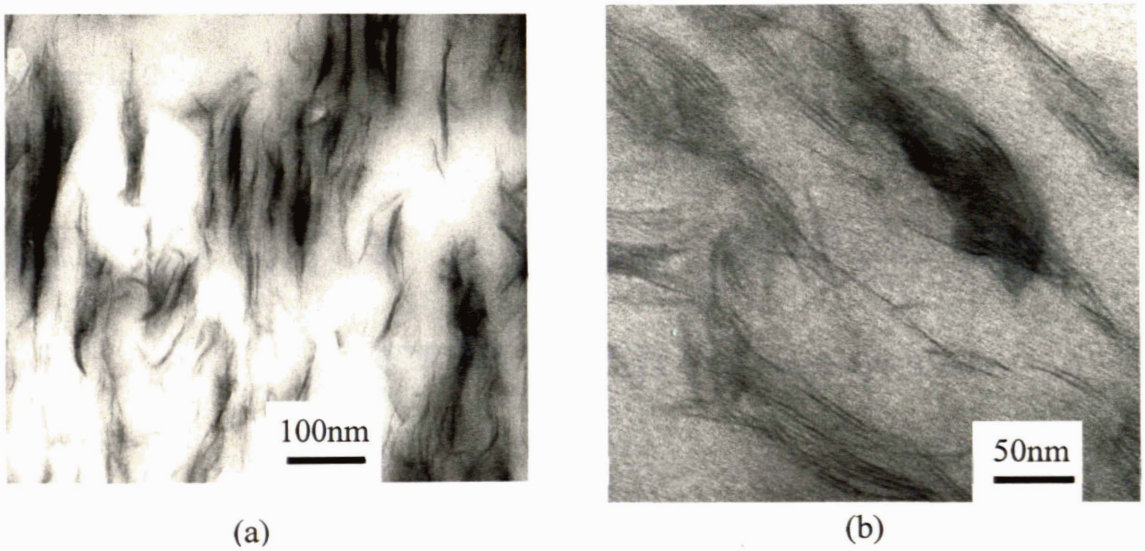

Figure 4.1 TEMs of MXD6 nylon/clay nanocomposite with 5.1 wt % clay. (a) magnified by 50,000; (b) magnified by 100,000 (Lee and McKinley, 2002).

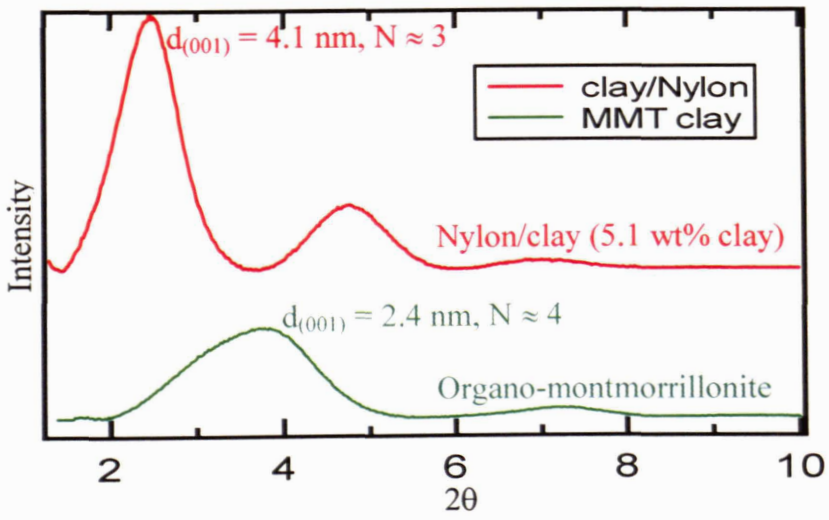

Figure 4.2 XRD patterns of nylon/clay nanocomposite (5.1-wt % clay) and organo-montmorillonite. (Lee and McKinley, 2002).

Structure of the clay particle: For simplicity, the internal structure of an intercalated clay particle is idealized as a multi-layer stack that contains N single silicate sheets (each sheet has an area A, an effective thickness d_s and mass M) with even interlayer spacing $d_{(001)}$, as illustrated in Figure 4.3. Separating adjacent sheets is a so-called gallery layer comprising both surfactants and polymer matrix chains that have penetrated the inter-silicate layers during processing. An important parameter of this structure is the volume fraction of silicate in the stack, defined as

$$\chi = \frac{V_{silicate}}{V_{stack}} = \frac{N d_s}{(N-1)d_{(001)} + d_s} = \frac{1}{\left\{\left(1-\frac{1}{N}\right)\left(\frac{d_{(001)}}{d_s}\right)+\frac{1}{N}\right\}}. \tag{4.1}$$

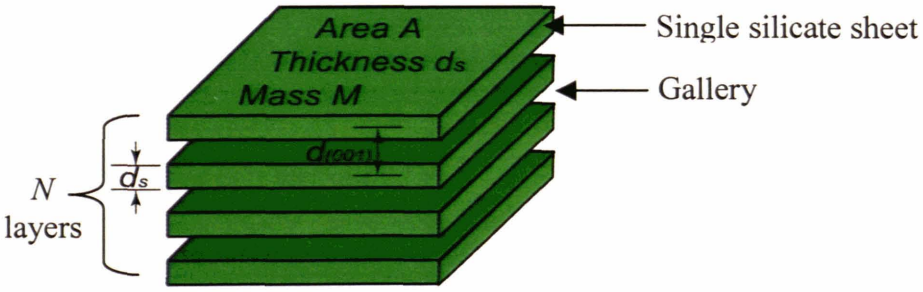

Figure 4.3 Schematic of a multi-layer clay stack.

Each individual silicate sheet further consists of n repetitive lattice cells, each of area A_0, thickness d_s, and molecular weight M_0. The typical values of these molecular parameters of a montmorillonite lattice cell (Figure 4.4) used in molecular dynamics simulations (Manovitch and Rutledge, 2002) are listed in Table 4.1. This structure will now be utilized to determine important particle characteristics that govern properties, including determination of the particle aspect ratio, volume fraction of the particle (if given weight fraction), and particle stiffness (which may be anisotropic).

Note that in this chapter, the subscripts *sheet*, *gallery*, and *stack* will be used to denote the properties of the silicate sheet, the gallery material, and the composite stack, respectively.

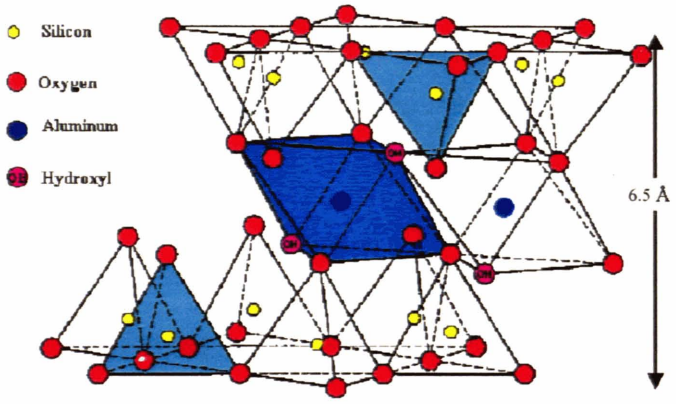

Figure 4.4 Chemical structure of montmorillonite lattice.

Table 4.1: Molecular characterization of montmorillonite lattice cell (Rutledge, 2002)

	Unit	Symbol	Value
MMT repetitive cell formula			$2\{Al_2Si_4O_{10}(OH)_2\}$
MMT cell planar dimensions	nm	(a_0, b_0)	(0.53, 0.92)
MMT cell planar area	$(nm)^2$	$A_0 = a_0 b_0$	0.49
MMT cell thickness	nm	c_0 $(c_0 = d_s)$	0.615
MMT cell molecular weight	g/mol	M_0	720

4.1. Effective Particle Aspect Ratio

For a multi-layer stack as illustrated in Figure 4.2, the particle thickness t can be related to the internal structure parameters N and $d_{(001)}$ through

$$t = (N-1)d_{(001)} + d_s, \tag{4.2}$$

where d_s, the silicate sheet thickness, is viewed as a constant fixed by the sheet chemistry. The particle aspect ratio L/t is thus

$$\frac{L}{t} = \frac{L}{(N-1)d_{(001)} + d_s}. \tag{4.3}$$

Eqn. (4.3) can be further written in terms of the parameter χ (the silicate volume fraction) defined in Eqn. (4.1)

$$\frac{L}{t} = \left(\frac{L}{Nd_s}\right)\chi. \tag{4.4}$$

4.2. Effective Particle Density

The density of the silicate sheet and the density of the gallery material are denoted by ρ_{sheet} and $\rho_{gallery}$, respectively. The density of the stack as a single entity is a combination of ρ_{sheet} and $\rho_{gallery}$ weighted by the silicate volume fraction χ:

$$\rho_{stack} = \chi\rho_{sheet} + (1-\chi)\rho_{gallery}. \tag{4.5}$$

ρ_{sheet} can be calculated from the lattice cell parameters given in Table 4.1,

$$\rho_{sheet} = \rho_{cell} = \frac{M_0}{A_0 c_0} = \frac{M_0}{A_0 d_s} = 4.0 g/(cm)^3. \tag{4.6}$$

Generally speaking, if the clay is pure, the gallery is essentially empty and $\rho_{gallery} << \rho_{sheet}$. However, clay particles are often modified by organo surfactants in order to obtain better exfoliation, and the surfactants may have a bulk density as high as 1 g/(cm)^3 (Rutledge, p.c., 2002). The mass density of the interlayer gallery depends on the amount of polymer chains that have penetrated the inter-silicate layers as well as the coverage of the clay surface by the surfactants and the chemical structure of the surfactant molecules. Since

the quantity $\rho_{gallery}$ is dependent on these parameters, the stack density will be specified in terms of a normalized variable $\rho_{gallery}/\rho_{sheet}$, viewed as a characteristic material parameter of the expanded clay particle:

$$\rho_{stack} = \chi \rho_{sheet} \left[1 + (1-\chi) \cdot \frac{\rho_{gallery}}{\rho_{sheet}} \right]. \tag{4.7}$$

Taking ρ_{sheet} to be 4.0 g/cc (4.6), the stack density is plotted as a function of $\rho_{gallery}/\rho_{sheet}$ in Figure 4.5 for two sets of clay structural parameters corresponding to the organo-clay and the 5.1-wt % nylon/clay nanocomposite (Figure 4.1 and 4.2), respectively. The strong dependence of ρ_{stack} on $\rho_{gallery}/\rho_{sheet}$ demonstrates the importance of getting a good estimation for $\rho_{gallery}$, which will be part of the future work.

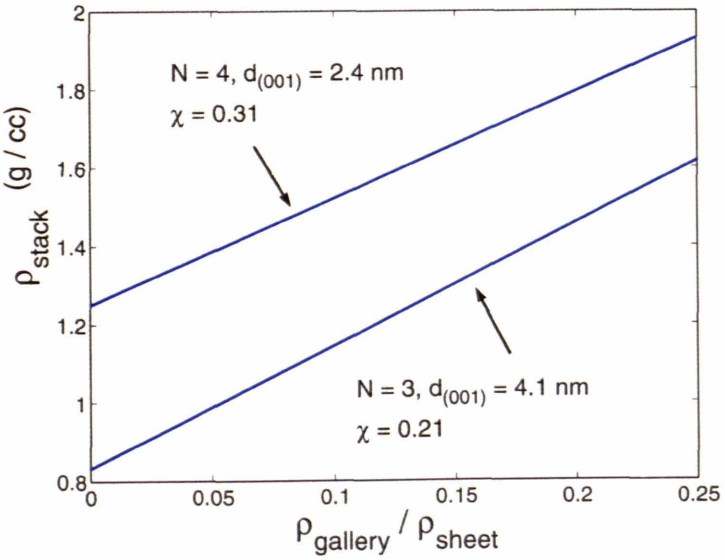

Figure 4.5 Dependence of ρ_{stack} on $\rho_{gallery}/\rho_{sheet}$ (ρ_{sheet} = 4 g/cc, d_s = 0.615 nm).

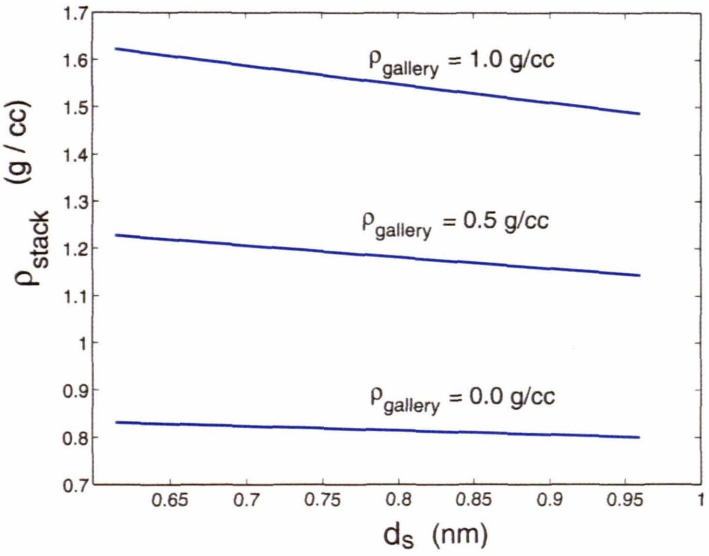

Figure 4.6 Dependence of ρ_{stack} on the choice of d_s ($N = 3$, $d_{(001)} = 4.1$ nm).

Note that the definition of the thickness of a single silicate layer (d_s or c_0) is still a controversial subject; values such as 0.883 nm and 0.96 nm have been assigned to d_s (Rutledge, 2002) other than the 0.615 nm used by Manovitch and Rutledge due to different choices of definitions. Note that the Manovitch and Rutledge MD simulations compute the quantity E_{sheet} ds; they then took d_s=.615nm which, in turn, gave the value of 400 GPa for E_{sheet}. The value of d_s will affect both the silicate layer fraction, χ , (Eqn. 4.1) and the silicate sheet density, $\rho_{sheet,}$ (Eqn. 4.6, where $c_0 = d_s$). Figure 4.6 shows the slight sensitivity of the overall stack density to the value of d_s, for various values of $\rho_{gallery}$. The uncertainty of the effective particle density due to the definition of d_s is the lowest (~5%) when the gallery is empty; it rises with increasing gallery density and reaches ~15% when the bulk surfactant density of 1 g/cc is assigned to $\rho_{gallery}$.

In this thesis, we assume $\rho_{gallery} << \rho_{sheet}$, and d_s = 0.615 nm in order to avoid unnecessary confusion and to stay consistent with molecular dynamics simulations.

The conformation and properties of the gallery matter, however, will be studied in the future work.

Taking ρ_{sheet} to be 4.0 g/cc (4.6) and assuming $\rho_{gallery} << \rho_{sheet}$, we have

$$\rho_{stack} = 4\chi \ g/(cm)^3 \tag{4.8}$$

A further step is to calculate the "clay particle" volume fraction, f_p, from a given weight fraction, W_p (noting that W_p is the standard material parameter available from processing, yet f_p is needed as an input for the constitutive modeling):

$$f_p = (W_p/\rho_{stack}) / (W_p/\rho_{stack} + (1-W_p)/\rho_{polymer}), \tag{4.9}$$

where the matrix polymer density, $\rho_{polymer}$, is ~1 g/cc. Calculations based on (4.8) give $\boldsymbol{f_p/W_p = 1.2}$ for organo-clay and $\boldsymbol{f_p/W_p = 0.8}$ for 5.1-wt % nylon/clay (XRD of both shown in Figure 4.2). The fact that the conversion ratio f_p/W_p varies with differing clay particle structure, and can be larger than 1.0 contradicts corresponding data in the literature (recall that f_p/W_p = 0.4 for clay/nylon has been used in Section 3.1.2, following Beall (Beall, 2000)). Therefore in the next chapter, to compare modeling results with experimental data, special attention will be given to this issue of converting from weight fraction to volume fraction; instead of simply quoting from the literature, Eqn. 4.8 will be used to make direct connections with XRD experiments performed on the test samples.

4.3. Effective Elastic Properties

The stiffness of a layer of montmorillonite sheet comprising a 'pure' clay particle has been obtained from molecular dynamics simulations. Manovitch and Rutledge (2002) calculated the elastic constants of a single silicate sheet using different simulation

protocols. Using d_s = 0.615 nm, they estimated the stiffness of a single sheet ($E_{1,sheet}$), to be ~400 GPa.

However, the longitudinal stiffness of a multi-layer stack ($E_{1,stack}$), as illustrated in Figure 4.3, depends on the silicate layer fraction χ. Using a simple Voigt model, $E_{1,stack}$ can be estimated as

$$E_{1,stack} = \chi E_{sheet} + (1-\chi)E_{gallery}, \tag{4.10}$$

where χ is the silicate fraction defined in (4.1) and $E_{gallery}$ is the stiffness of the gallery substance. Assuming $E_{gallery} << E_{sheet}$, Eqn. 4.10 can be approximated by

$$E_{1,stack} \cong \chi E_{sheet}. \tag{4.11}$$

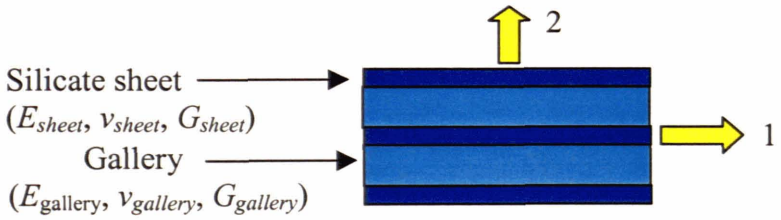

Figure 4.7 Schematic of a lamina with two phases: silicate sheet and gallery.

Although the particle has been treated as an isotropic material so far, it is more realistic to model it with transverse isotropy. In fact, considering the multi-layer clay particle as a lamina (Figure 4.7), the overall elastic constants E_1, E_2, ν_{12}, and G_{12} can be estimated from simple upper and lower bound approximations as

$$E_{1,stack} = \chi E_{sheet} + (1-\chi)E_{gallery} \tag{4.11}$$

$$E_{2,stack} = \frac{E_{sheet}E_{gallery}}{(1-\chi)E_{sheet} + \chi E_{gallery}} \tag{4.12}$$

$$\nu_{12,stack} = \chi \nu_{12,sheet} + (1-\chi)\nu_{12,gallery} \tag{4.13}$$

$$G_{12,stack} = \frac{G_{12,sheet} G_{12,gallery}}{(1-\chi) G_{12,sheet} + \chi G_{12,gallery}} \tag{4.14}$$

Note that the above solutions are all approximations based on 1-D analysis. While (4.11), (4.12) and (4.14) give reasonably accurate predictions, (4.12) is only a lower bound for E_2. The fact that the clay particle is much stiffer than the polymer places a high lateral constraint on the contraction of the polymer that would occur in the 1-direction if loaded in the 2-direction. Taking into account the lateral contraction effect on E_2, the transverse effective stiffness is actually

$$E_{2,stack} = \frac{E_{sheet} E_{gallery}}{(1-2\alpha v_{gallery})(1-\chi) E_{sheet} + (1-2\alpha v_{gallery}) \chi E_{gallery}}, \text{ with}$$

$$\alpha = \frac{E_{sheet} v_{gallery} - E_{gallery} v_{sheet}}{(1-v_{gallery}) E_{sheet} + (1-v_{sheet}) E_{gallery}}.$$

The effective shear modulus G_{12} and transverse stiffness E_2 of the stack are severely reduced by the low stiffness and shear capacity of the gallery material (4.12 and 4.14). The anisotropic properties of the clay particle and the effect of lowered particle shear modulus on the load transfer efficiency are under current study.

To summarize, we defined a clay particle parameter χ (Eqn. 4.1, the silicate layer fraction) which is determined by characteristic clay crystallite parameters $d_{(001)}$, N and d_s; the important effective properties of the clay particle are then expressed in terms of χ (L/t in (Eqn. 4.4), ρ_{stack} in (Eqn. 4.8), f_p/W_p in (Eqn. 4.9) and $E_{1,stack}$ in (Eqn. 4.11)). With the above preparations, we are now ready to compare simulation results with tensile experiment data, which is the role of the following chapter.

Chapter 5

Axial Tensile Experiment

5.1. Experiment Description

Uniaxial tensile tests are conducted on injection-molded MXD6/clay nanocomposite specimens with a Model-5582 Instron at room temperature and a strain rate of ~0.05/s; Dog-bone-shaped plate tensile specimens with a gage length of 12.7 mm and a thickness of 3 mm were prepared according to *ASTM D638*. For each weight fraction of the nanoclay, 4 to 6 tests were performed. During each of the tests, an extensometer was used to measure the axial strain; the elastic tensile modulus was obtained from the initial slope of the true stress-strain curve.

5.2. Material Characterization

Eastman Chemical provided injection-molded MXD6 nylon/clay nanocomposites with various clay weight fractions: 0%, 1.1%, 3.13%, 3.67%, 4.17%, and 5.27%. The chemical structure of the polymer matrix is primarily MXD6-6007 polyamide, a high barrier polymer produced by Mitsubishi Gas and Chemical Company. The layered montmorillonite (MMT) clay used for these materials is the I.34MN organoclay available from Nanocor Inc.

A TEM micrograph of a sample with 5.1-wt % clay is shown in Figure 5.1 (a). Figure 5.1 (b) shows the TEM of the same material after processed at a screw RPM of 150 and T = 250°C. The injection-molded sample (a) has an intercalated morphology and exhibits a

preferential clay orientation that coincides with the flow direction. The melt-processed sample (b) exhibits higher degree of exfoliation and better particle alignment.

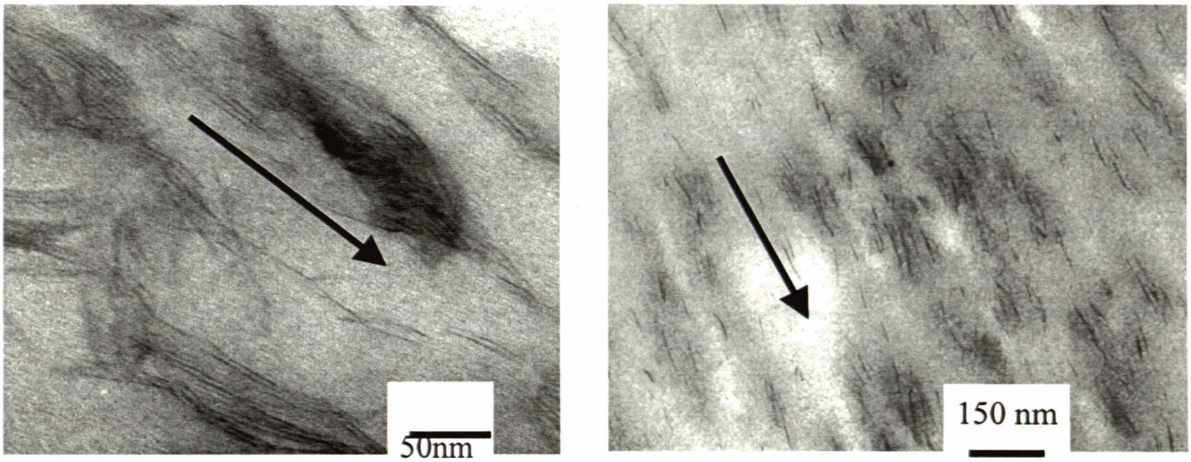

(a) (b)

Figure 5.1 (a) TEM of injection-molded MXD6/clay nanocomposite (5.1 wt % clay); (b) TEM of the same material after processing at a screw RPM of 150 and T = 250°C. Arrows indicate flow directions. (Lee and McKinley, 2002)

Wide-angle X-ray diffraction (WAXD) experiments were performed for the MMT I.34MN organoclay and the injection-molded nanocomposites with various clay contents. XRD is used to monitor the position (2θ), full width at half maximum (*fwhm*), and intensity of the (001) basal reflection corresponding to the repeat distance perpendicular to the layers. The average interlayer spacing ($d_{(001)}$) and the average clay particle thickness (t) can be determined using the Bragg equation ($d_{(001)} = \lambda / 2\sin\theta$) and the Scherrer equation ($t = 0.9\lambda / b\cos\theta$, b is the *fwhm*) respectively. However, characterization of the clay structure in the above manner bares some uncertainty since both the peak position and the intensity will be affected by the presence of internal layer disorder as well as numerous experimental factors (Vaia, 2000).

Figure 5.2 shows the XRD patterns of organo-clay and 3.13-wt % nylon/clay nanocomposite (Lee and McKinley, 2002). Characteristic parameters determined from the peak position and the *fwhm* are given in Table 5.1. XRD patterns of nylon/clay nanocomposites with various clay weight fractions are shown in Figure 5.3. The fact that the intensity increases linearly with clay content implies an average clay crystallite structure independent of clay fraction.

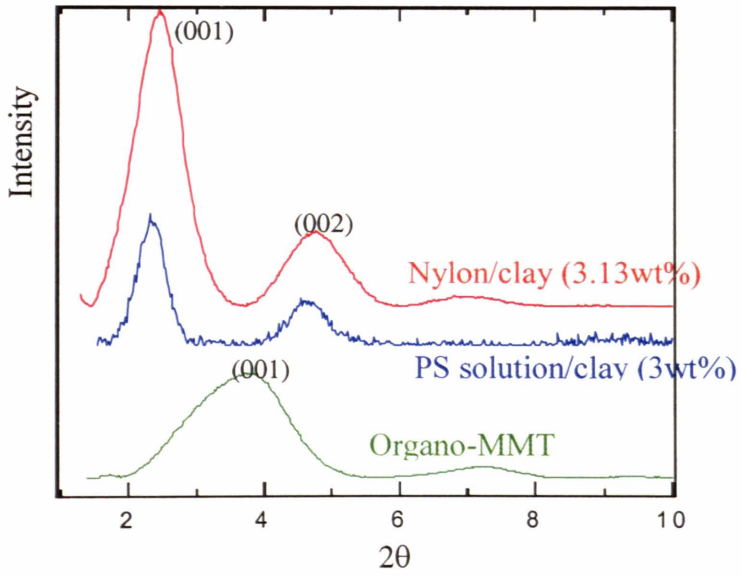

Figure 5.2 X-ray diffraction patterns for: MXD6/clay (3.13 wt%), PS solution/clay (3 wt%), and montmorrillonite (MMT). (Lee and McKinley, 2002)

Table 5.1: Structural characterization from XRD patterns in Figure 4.2 (Lee and McKinley, 2002).

Material	$d_{(001)}$ (nm)	t (nm)	N
Organo-MMT	2.4	8.74	~ 4
MXD6/MMT	4.1	10.3	~ 3
PS soln/MMT	3.8	15.1	~ 4

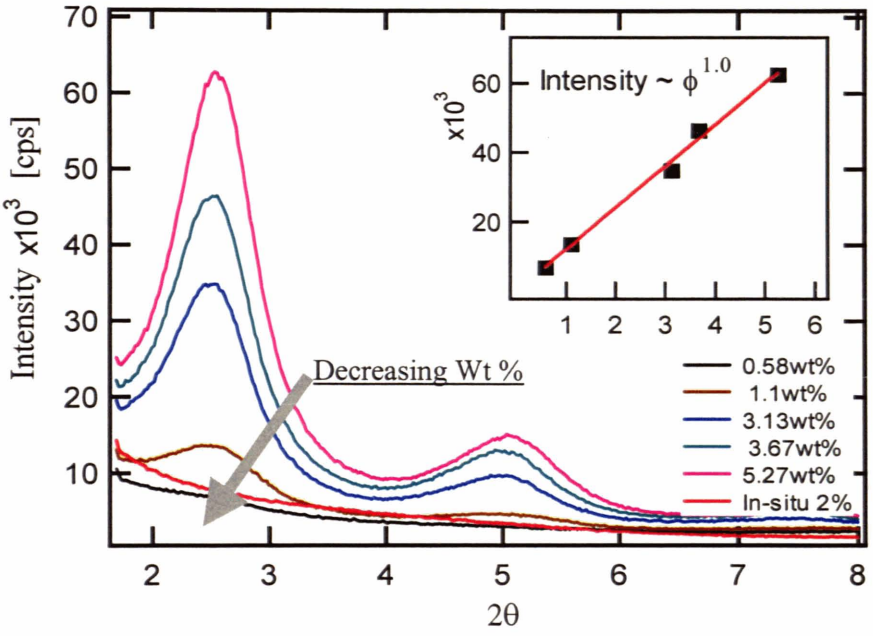

Figure 5.3 XRD patterns of MXD6/clay nanocomposites for various clay weight fraction: 0.58%, 1.10%, 3.13%, 3.67% and 5.27% (Lee and McKinley, 2002) with ϕ denoting clay weight fraction.

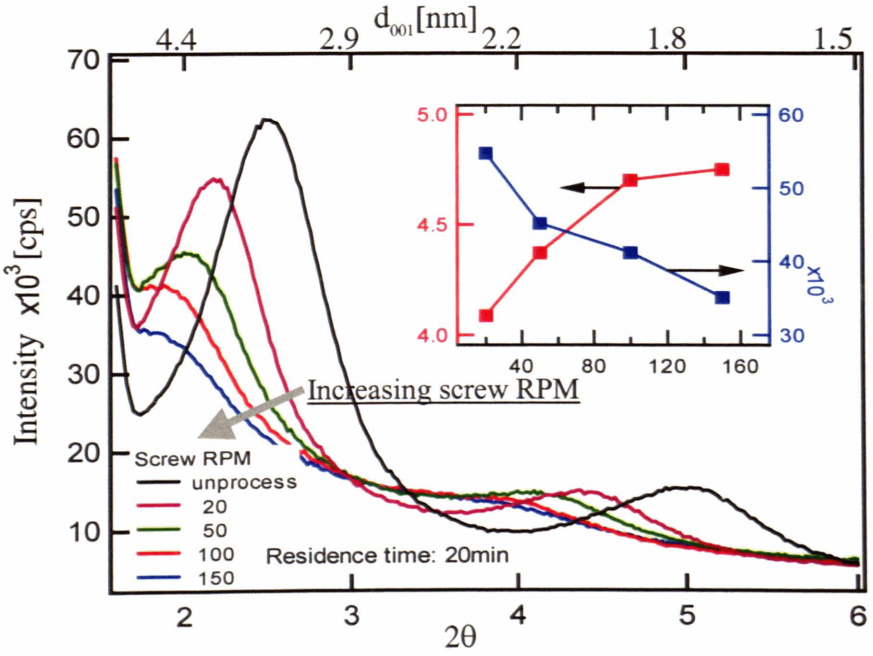

Figure 5.4 XRD patterns of 5.1-wt % nylon/clay nanocomposites after processed at various screw RPM (Lee and McKinley, 2002).

Figure 5.4 shows the XRD patterns of 5.1-wt % MXD6/clay nanocomposites after processed at various screw RPMs (Lee and McKinley, 2002). Decreasing intensity and peak position indicate the simultaneous occurrence of interlayer swelling and delamination, which is verified by the TEM image shown in Figure 5.1(b).

5.3. Determination of Model Parameters

Our 2-D RVEs with perfect particle alignment and randomly dispersed particle locations are employed to model the test samples from a micro/nano scale and to predict their macroscopic mechanical response.

In Chapter 3, the continuum model parameters (f_p, L/t, E_p/E_m) have been studied separately in order to understand the effects of each of them has on the macroscopic stiffness of the nanocomposite. However, as shown in Chapter 4, the effective particle properties L/t (Eqn. 4.4), ρ_{stack} (Eqn. 4.8) and E_{stack} (Eqn. 4.10) for a given material are intrinsically inter-connected through the parameter χ, which has the physical meaning of the volume fraction of silicate sheets in an intercalated clay particle. Each continuum-scale particle modeling parameter can be expressed in terms of the internal clay structure parameters $d_{(001)}$ and N.

- **Aspect ratio *L/t***

The MMT 1.34MN organoclay sheets have a typical lateral dimension of L = 200 nanometers, which is verified in the TEM images shown in Figures 3.1 and 4.1. As a first approximation, we ignore the variation in particle sizes and assume a uniform aspect ratio.

Taking L to be 200 nm and d_s to be 0.615 nm, the aspect ratio becomes

$$\frac{L}{t}=\left(\frac{L}{Nd_s}\right)\chi=\left(\frac{200}{0.615N}\right)\chi=\frac{325.2}{N}\chi \tag{5.1}$$

- **Clay volume fraction f_p**

Since the clay weight fraction (W_p) is typically the given material parameter, conversion from weight fractio, W_p, to volume fraction, f_p, is needed. For a nanocomposite of unit mass and a given clay weight fraction W_p, the volume fraction can be determined using the effective clay density ρ_{stack} (equation 4.8) and the polymer density $\rho_{polymer}$

$$f_p=\frac{V_{clay}}{V_{clay}+V_{polymer}}=\left(\frac{W_p}{\rho_{stack}}\right)\Big/\left(\frac{W_p}{\rho_{stack}}+\frac{1-W_p}{\rho_{polymer}}\right). \tag{5.2}$$

Taking (4.8) into (5.2) and assuming $\rho_{polymer}$ to be 1 g/cc, we have

$$f_p=\frac{W_p}{4\chi\left[1-(1-1/4\chi)W_p\right]}\cong\frac{W_p}{4\chi}\ \text{for}\ W_p<<1; \tag{5.3}$$

therefore

$$\frac{f_p}{W_p}\cong\frac{1}{4\chi}\ \text{for}\ W_p<<1. \tag{5.4}$$

- **Particle/matrix stiffness ratio E_p/E_m**

The matrix tensile modulus is obtained from the tensile test results on pure MXD6 samples (Wt % ≈ 0) and found to be $E_m \approx 4\text{GPa}$. On the other hand, the effective particle modulus has been written in terms of the silicate modulus, E_{sheet}, and the silicate layer fraction, χ (Eqn. 4.10). Taking E_{sheet} to be the in-plane modulus computed in the molecular dynamics simulation, 400 GPa, we have

$$\frac{E_p}{E_m}=\frac{E_{stack}}{E_m}=\frac{400\chi}{4}=100\chi. \tag{5.5}$$

The dependence of L/t, f_p/W_p, and E_p/E_m on the internal clay structural parameters $d_{(001)}$ and N, through their influence on the silicate layer fraction χ, are depicted in Figures 5.5, 5.6, and 5.7, respectively. An increase in either N or L/t will lead to an increase in f_p/W_p and decreases in L/t and E_p/E_m. While the impact of the interlayer spacing, $d_{(001)}$, is rather small (especially on L/t and E_p/E_m) for the chosen range, the number of layers, N, shows a distinct influence on all three effective particle properties. In particular, the values of these properties experience a significant jump when N increase from 1 to 2, which coincides with the morphological transition from exfoliation to intercalation.

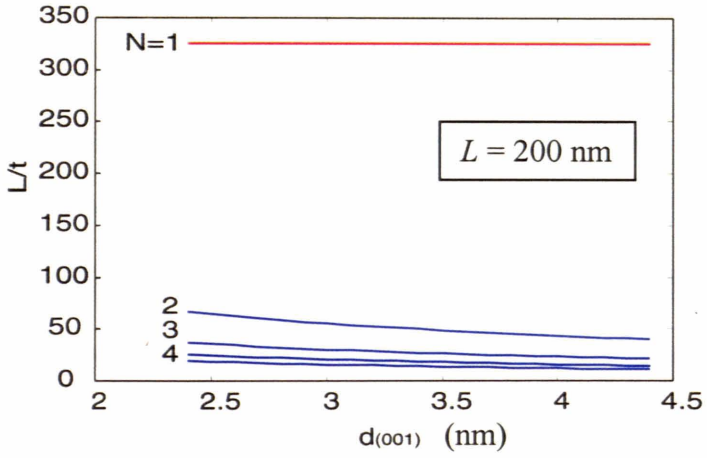

Figure 5.5 Dependence of L/t on $d_{(001)}$ and N.

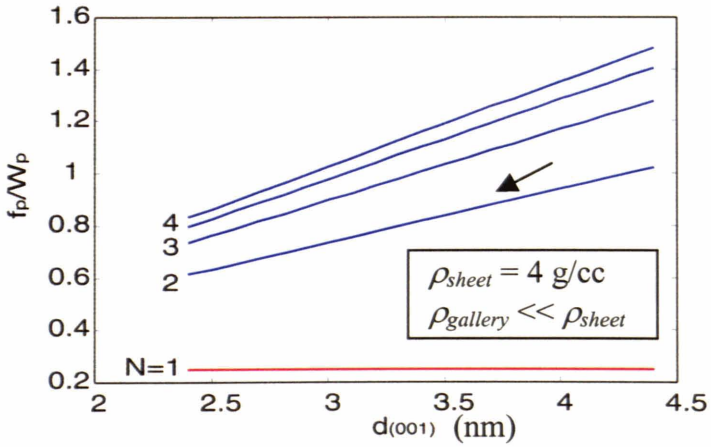

Figure 5.6 Dependence of f_p/W_p on $d_{(001)}$ and N.

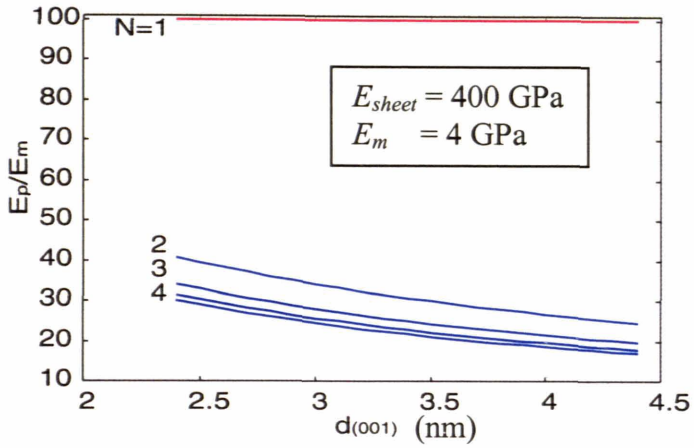

Figure 5.7 Dependence of E_p/E_m on $d_{(001)}$ and N.

5.4. Experimental Data and Simulation Results

With the characteristic clay structural parameters extracted from the XRD patterns and TEM micrographs of the experiment samples (Table 5.1) and the model parameters expressed in terms of the clay structural parameters (Eqs. 5.1, 5.4, 5.5), we are now ready to predict the macroscopic mechanical properties of the tested nanocomposites.

Before fitting experimental data with some particular values of $d_{(001)}$ and N, it will be interesting to see how the effective stiffness is affected by these nano-scale parameters through their influence on the model parameters. For purposes of illustration, the Mori-Tanaka-type micromechanics model is used to show the trends. Figure 5.7 shows the dependence of E_{11} on $d_{(001)}$ and N for a fixed clay content (5.1-wt %). While E_{11} appears almost unaffected by $d_{(001)}$, it is rather sensitive to N due to the big impact of N on L/t, E_p/E_m and f_p/W_p, as shown in Figures 5.5 to 5.7. Although f_p is smaller for a given W_p when $N = 1$, the corresponding negative effect on E_{11} is counteracted by extremely large L/t and E_p/E_m. In Figure 5.8, E_{11} is plotted as a function of clay weight fraction and the

clay structural parameter N for a fixed interlayer spacing of $d_{(001)}$ = 4.1 nm. E_{11} drops dramatically with increasing N, suggesting that complete exfoliation is desired for best stiffness reinforcement.

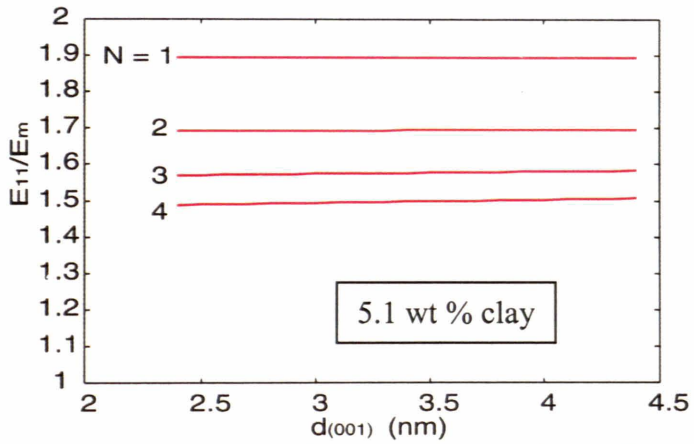

Figure 5.8 Dependence of macroscopic stiffness E_{11} on clay structural parameters $d_{(001)}$ and N (5.1-wt % clay); Mori-Tanaka-type micromechanics model is used to predict E_{11}.

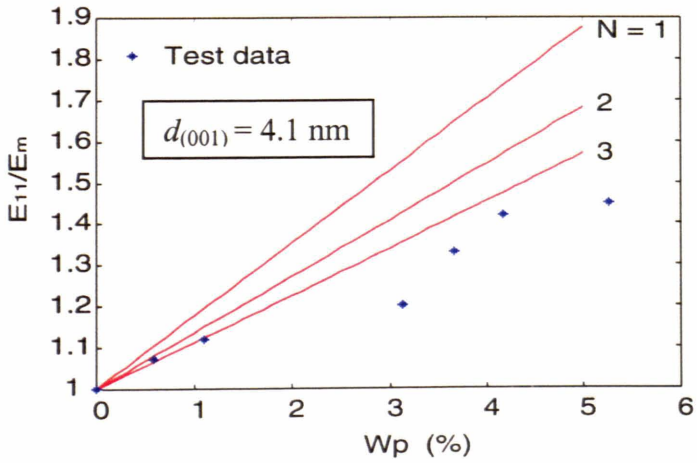

Figure 5.9 Dependence of macroscopic stiffness E_{11} on clay weight fraction and clay structural parameter N ($d_{(001)}$ = 4.1 nm); Mori-Tanaka-type micromechanics model is used to predict E_{11}.

We compare the experimental data with both our simulation results and the prediction from the Halpin-Tsai equation and the Tandon-Weng closed-form solution based on the

Mori-Tanaka models. Both the composite theories and our FE model share the same input variables: the particle volume fraction f_p, the particle aspect ratio L/t, and the ratio of particle/matrix stiffness E_p/E_m. Taking $d_{(001)}$ = 4.1 nm and N = 3 from Table 5.1, we are able to obtain L/t = 23, f_p/W_p = 1.20, and E_p/E_m = 21. Note that these parameters are specially calculated for an intercalated multi-layer clay structure, thereby differ from what are expected from the conventional perspective. For instance, f_p/W_p = 1.20 > 1 even though in bulk the clay is denser than the polymer (recall that Beall has used f_p/W_p=0.4 for nylon/clay (Beall, 2000)); E_p/E_m = 21 even though the modulus of a single silicate layer is 400 GPa and the modulus of the polymer is 4 GPa (i.e. E_{sheet}/E_m = 100, but E_p/E_m=21). Prediction results for the nanocomposite modulus are depicted in Figure 5.10. Figure 5.10 shows that the simulation results using these effective particle properties are in good accordance with the experimental data.

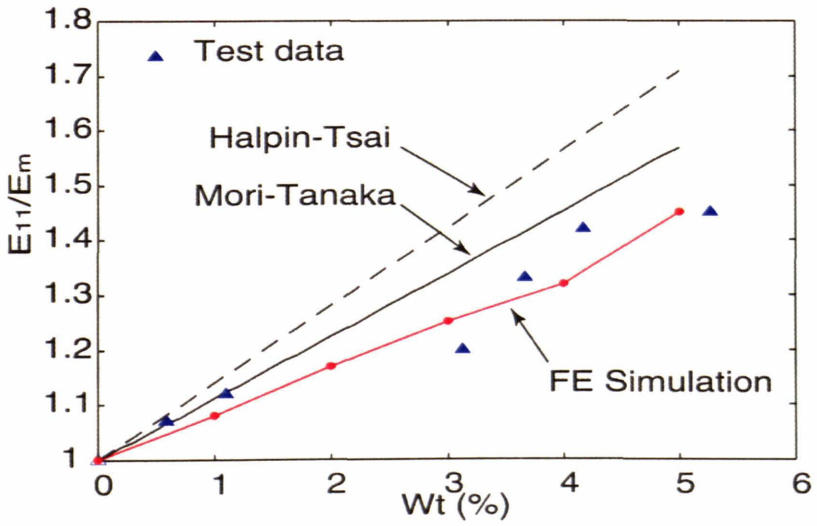

Figure 5.10 Prediction of the effective longitudinal modulus. (L/t = 23, E_p/E_m = 21, f_p/W_p = 1.20).

It has also been of our interest to see the effect of processing on the overall mechanical properties of the nanocomposite (TEM in Fig 5.1(b) and XRD in Fig 5.4 both indicate a

better exfoliated morphology). Although tensile specimens of the processed material were not yet available, we can predict the dependence of the nanocomposite modulus on structural information that we have extracted from the TEM images and the XRD patterns. Based on Fig 5.1(b) and Fig 5.4, an estimation of $d_{(001)} \approx 4.5$ nm and $N \approx 2$ can be made for the material processed at a screw RPM of 150. Using Eqs. 5.1, 5.4 and 5.5, corresponding effective particle properties can be calculated as: $L/t = 39$, $E_p/E_m = 24$, and $f_p/W_p = 1.04$. Figure 5.11 compares the predictions of the modulus of the MXD6/clay nanocomposite (Fig 5.1(a)) and the same material after processing at a screw RPM of 150 (Fig 5.1(b)); the modulus corresponding to a completely exfoliated morphology is depicted as well in order to demonstrate the upper limit of the possible effect of nanoclay on the overall composite modulus for this material system. The characteristic parameters of the materials compared in Figure 5.11 are summarized in Table 5.2.

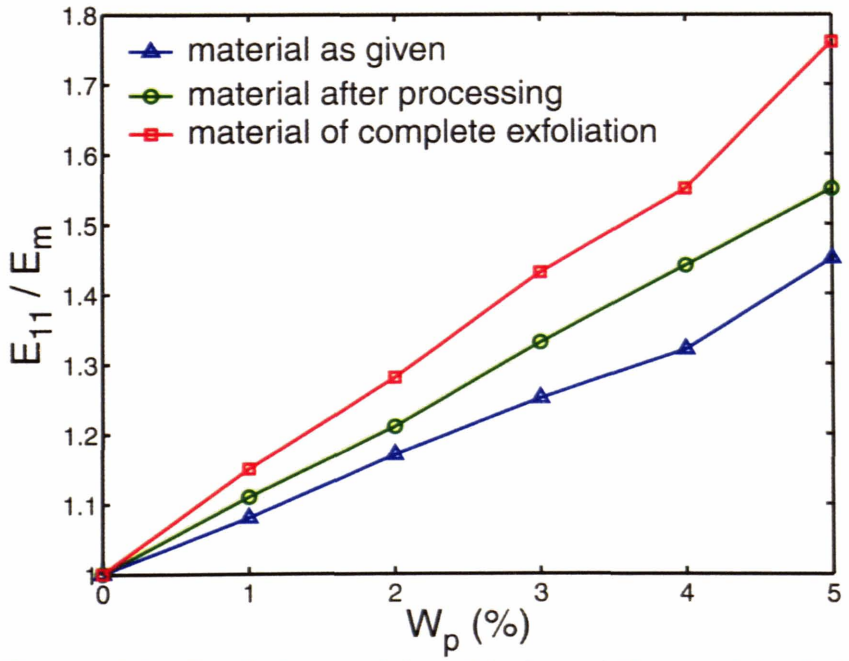

Figure 5.11 Predictions of the effective stiffness of the MXD6/clay nanocomposites before and after melt processing.

Table 5.2: Characteristic parameters of MXD6/clay nanocomposites before/after melt processing.

Material	$d_{(001)}$ (nm)	N	L/t	f_p/W_p	E_p/E_m
MXD6/clay (as given)	4.1	~3	23	1.20	21
After processing	4.5	~2	39	1.04	24
Completely exfoliated		1	**325**	**0.25**	**100**

Figure 5.11 shows notable increase in E_{11} associated with increasing degree of exfoliation, which is attributed to the increased particle aspect ratio and particle modulus. Note that the extremely large L/t and E_p/E_m when $N = 1$ did not bring about a dramatic jump in E_{11} due to the significantly reduced conversion ratio f_p/W_p. It should also be noted that the particles are assumed to remain planar in the modeling, however TEM images show that fully exfoliated single silicate layers and two-layer particles have a greater tendency to be curved compared to particles with more layers; this increased bending compliance will further reduce the efficiency of fully exfoliated particles in the enhancement of composite modulus. Thereby complete exfoliation may not be the optimal choice as long as the overall stiffness is concerned.

Chapter 6

Results Under Other Modes of Loading

In our idealized model of the polymer-layered silicate nanocomposite, where the randomly dispersed platelet particles have perfect alignment (i.e., all particles are aligned in the axial direction), the composite can be treated as a transversely isotropic material, with the plane of isotropy parallel to the particle plane. Figure 6.1 shows a schematic of a 3D RVE of such structure together with our simplified 2D plane strain model.

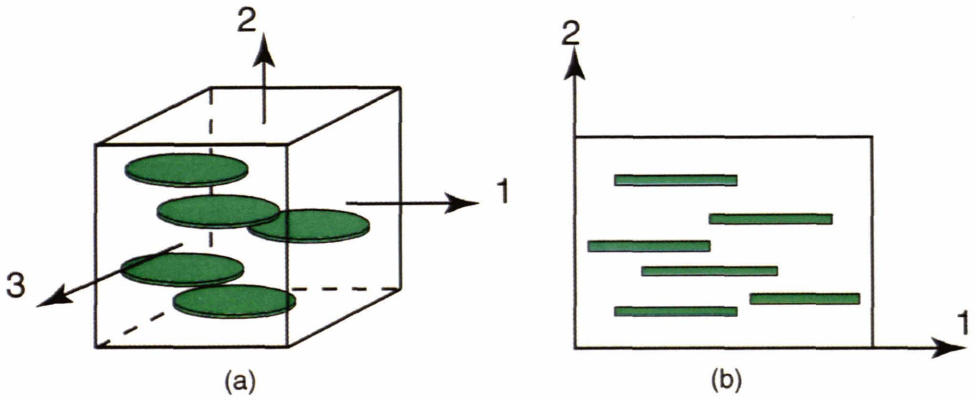

Figure 6.1 Schematic of 3D RVE and 2D RVE

Assume the 1-3 plane in Figure 6.1 to be the plane of isotropy, transverse isotropy requires

$$E_{11} = E_{33},\ \nu_{13} = \nu_{31},\ \nu_{21} = \nu_{23},\ \nu_{12} = \nu_{32},\ G_{12} = G_{23}. \tag{6.1}$$

The in-plane shear modulus G_{13} can be obtained from E_{11} and ν_{13}

$$G_{13} = E_p/2(1+\nu_{13}). \tag{6.2}$$

The two Poisson's ratio ν_{12} and ν_{21} are generally different and are related by

$$\frac{\nu_{12}}{E_{11}} = \frac{\nu_{21}}{E_{22}}. \tag{6.3}$$

Due to the symmetry of the fourth-order elastic modulus tensor, there are only five independent elastic constants: E_{11}, E_{22}, ν_{12}, G_{12}, and G_{13}. However, our 2D plane strain model, illustrated in Figure 6.1 (b), cannot predict the in-plane shear modulus G_{13}. Thus in this chapter, we only study the effective transverse modulus E_{22}, the two Poisson's ratio ν_{12} and ν_{21}, and the transverse shear modulus G_{12}.

Note that the simulation results of E_{22} are normalized with respect to the plane strain Young's modulus of the matrix; while the results of the two Poisson ratios are n normalized with respect to the plane strain Poisson ratio of the matrix. Relationships between the plane strain moduli and the actual moduli of transversely isotropic materials are given in Appendix D.

6.1. Prediction of Effective Transverse Modulus

The effective transverse modulus of a system with random particle dispersion is computed by applying a macroscopic strain ε_{22} to the RVE and proper averaging over the σ_{22} stress field. The periodic boundary conditions are given in section 2.3.2.1, with axial loading perpendicular to the particle planes instead of parallel to them. The effective transverse modulus E_{22} is a function of various morphological and material factors

$$E_{22} / E_m = E_{22} / E_m(f_p, L/t, E_p / E_m, \nu_m, \nu_p, \textit{particle distribution}).$$

Owing to the short reinforcing length in the 2-direction, the overall transverse stiffness of the composite is not enhanced as much by the nano-scale inclusions as the longitudinal overall stiffness is. However, studies on the dependence of E_{22} on each of the geometrical

or material parameters show similar trends exhibited by E_{11}, only at a much smaller magnitude of enhancement.

6.1.1. Effect of particle volume faction, aspect ratio and particle/matrix stiffness ratio

The effective transverse stiffness E_{22} is plotted as a function of the particle volume fraction, particle aspect ratio, and the particle/matrix stiffness ratio respectively in Figure 6.1, 6.2, and 6.3. An increase in any of these factors results in an increase in the overall transverse stiffness. The nonlinear dependence of E_{22} on each of these factors is clearly demonstrated as well. While studying these curves, it is important to bear in mind that the influences of these parameters have been exaggerated by the scales (2.5% particles with an aspect ratio of 100 merely bring about a 14% increase in E_{22}).

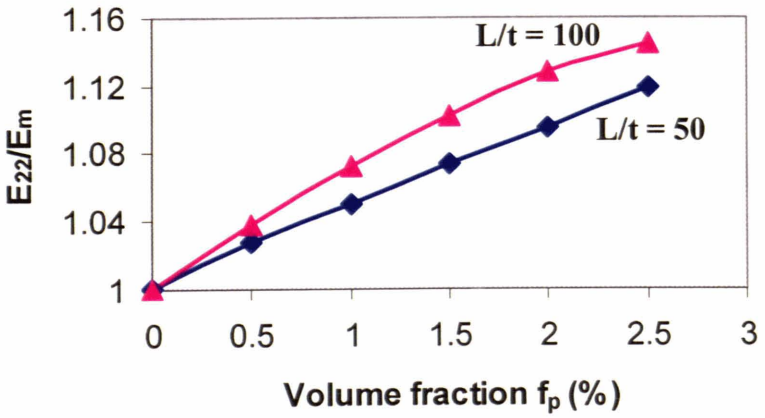

Figure 6.2 Dependence on clay volume fraction ($E_p/E_m = 100$, $v_p = 0.2$, $v_m = 0.35$)

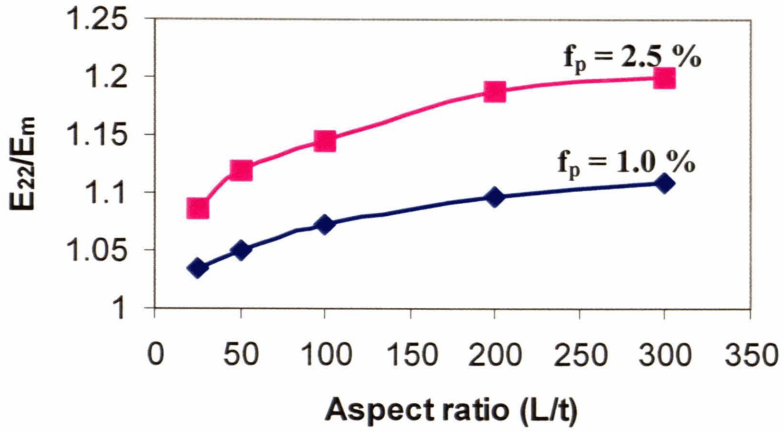

Figure 6.3 Dependence on particle aspect ratio ($E_p/E_m = 100$, $v_p = 0.2$, $v_m = 0.35$)

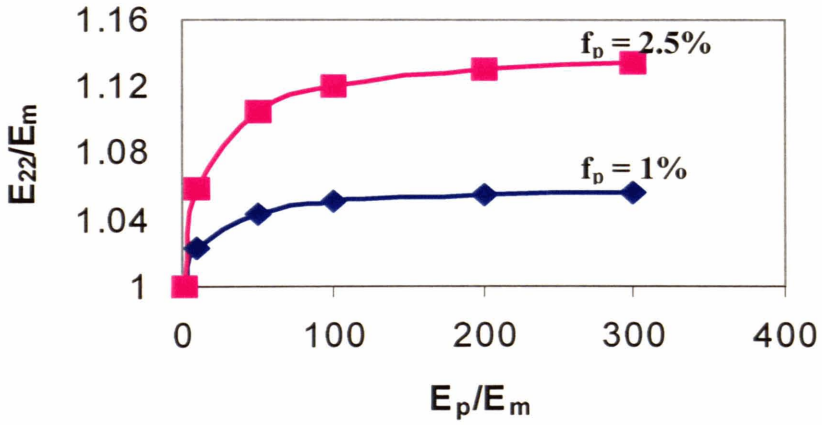

Figure 6.4 Dependence on the particle/matrix stiffness ratio (L/t = 50, v_p = 0.2, v_m = 0.35);

6.1.2. Reinforcing Mechanism

Studies on both the longitudinal and the transverse overall stiffness indicate that materials with high particle volume fraction, high aspect ratio, or high ratio of particle/matrix stiffness are desirable for more efficient reinforcement in both directions. However, the enhancement in E_{22} is far less dramatic than E_{11}, and the stiffness enhancement mechanisms corresponding to each of them are rather different. For particles with high

aspect ratio (large length and small thickness), while the normal stress in the particle can build up along the particle length under longitudinal loading, there is hardly any distance along the particle thickness for the normal stress to grow up. Thus the load transfer mechanism responsible for the enhancement of the longitudinal stiffness does not apply here. Indeed, from equilibrium, the σ_{22} stress in the particle is equal to that in the matrix. We will come to see through the following discussion that the strain shielding in the matrix becomes a key mechanism in the case of transverse reinforcement.

A simple model that predicts the overall transverse modulus is the lower bound model, which describes the extreme case of continuous particle reinforcement. By assuming uniform stress σ_{22}, it is easy to obtain the following equation

$$\frac{1}{E_{22}} = \frac{f_p}{E_p} + \frac{1-f_p}{E_m}, \text{ or}$$

$$\frac{E_{22}}{E_m} = \frac{1}{1-f_p\left[1-\frac{1}{(E_p/E_m)}\right]}. \tag{6.4}$$

Eq. 6.4 predicts the increase of the effective transverse modulus with increase in particle volume fraction or particle/matrix stiffness ratio (the dependence of E_{22}/E_m on f_p and E_p/E_m predicted by the lower bound are plotted in Figure 6.10 and Figure 6.12, respectively). However, the simulation results also demonstrate an increase in E_{22} with increase in the particle aspect ratio (Figure 6.2, Figure 6.3). Now that the shear-lag load transfer mechanism of the axial loading no longer applies, there is no obvious interpretation for such effect of the particle aspect ratio on the transverse stiffness.

In order to study the role of particle aspect ratio on transverse reinforcement, a series of simulations are conducted on staggered array structures with various L/t and fixed f_p and

E_p/E_m, as shown in Figure 6.5. Note that the ratio of a/L is kept the same ($a/L = 2$) for all four structures so as to reduce possible disturbance from the shape of the cell. The simulation results of these structures are plotted in Figure 6.6.

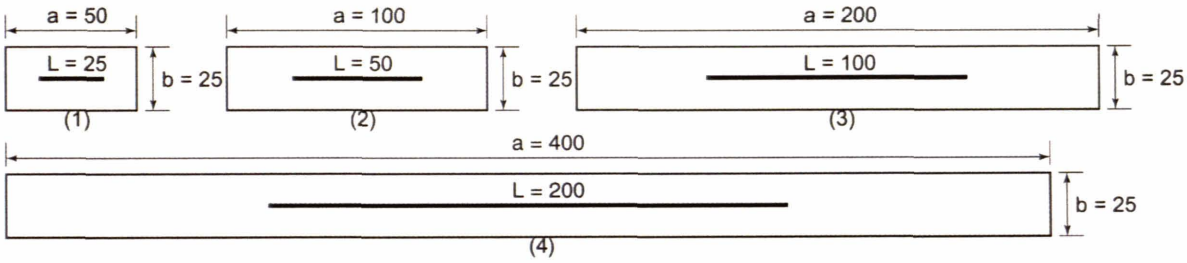

Figure 6.5 Unit cell of "staggered" array ($f_p = 2\%$, $a/L = 2$, particle thickness $t = 1$). (1) L/t = 25; (2) L/t = 50; (3) L/t = 100; (4) L/t = 200.

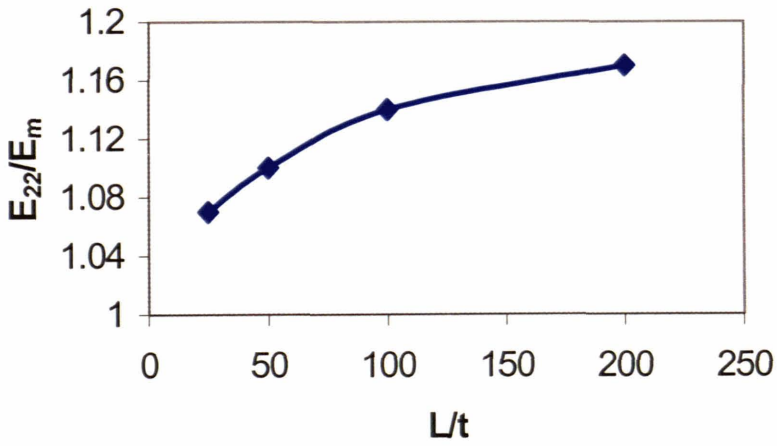

Figure 6.6 Transverse stiffness of the staggered array structures shown in Figure 6.5

Recall that the average stiffness can be viewed as a mapping between the average strain and average stress (equation 1.6); it is crucial to find out how the average stress σ_{22} over the whole RVE is affected by the aspect ratio of the particle. Since the overall average stress is merely a combination of the average particle stress and average matrix stress

(equation 1.4), we will examine the impact of particle aspect ratio on the distribution of σ_{22} both in the matrix and in the particle (the matrix stress becomes important since σ_{22} is continuous in the composite and σ_{22} in the particle is not larger than in the matrix).

The distributions of σ_{22} in particles with various aspect ratios are shown in Figure 6.7 (all under the same amount of applied macroscopic strain). Although the stress concentration at the ends of the particle increases dramatically with increase in particle length, the average σ_{22} in the particle only exhibits slight increase which makes an almost negligible contribution to the overall average transverse stress, due to the small volume fraction of the particle. Thus it is reasonable to assume that the impact of particle aspect ratio on E_{22} mainly comes from the increase in σ_{22} in the matrix with increasing particle aspect ratio. This assumption is well proved by the contrast between the contour of σ_{22} in the matrix of a structure with an aspect ratio of 50 and that of another one with an aspect ratio of 100, as shown in Figure 6.8 (both under a 0.005 macroscopic transverse strain). It is clear that larger particle aspect ratio induces higher transverse stress in the matrix. To understand the cause of the impact of particle aspect ratio on the matrix stress, a study on the strain state of the matrix is necessary. In an isotropic material, the constitutive equation can be written as

$$\sigma_{22} = \frac{(1-v)E\varepsilon_{22}}{(1+v)(1-2v)} + \frac{vE\varepsilon_{11}}{(1+v)(1-2v)} + \frac{vE\varepsilon_{33}}{(1+v)(1-2v)}, \tag{6.5}$$

where E and v are Young's modulus and Poisson ratio, respectively.

Since plane strain model is used in the simulation, the term involving ε_{33} can be omitted. Note that ε_{11} in the matrix is negative, (6.5) can be rewritten as

$$\sigma_{22} = A\varepsilon_{22} - B|\varepsilon_{11}|, \tag{6.6}$$

where A, and B are positive material constants. Either an increase in ε_{22} or a decrease in the absolute value of ε_{11} will result in an increase in σ_{22}. With the macroscopic transverse strain kept fixed, ε_{22} in the matrix won't change much when the particle aspect ratio varies. However, $|\varepsilon_{11}|$ is relatively sensitive to the particle aspect ratio. Under transverse loading, the transverse stress σ_{22} is continuous, ε_{22} is much smaller in the particle than in the matrix due to the larger stiffness of the particle, thus the particle will not contract as much as the matrix does. The matrix surrounding the particle is constrained from contracting due to compatibility requirement, i.e., $|\varepsilon_{11}|$ in the matrix is **constrained** by the particle.

Figure 6.9 shows the contour of ε_{11} in the matrix of a structure with an aspect ratio of 50 and that of another one with an aspect ratio of 100 (the contours of σ_{22} of the same structures have been shown in Figure 6.8). To make the constraining effect clearer, the maximum contour value is set to be $-\varepsilon_{22}\nu_m$, where ε_{22} is the macroscopic transverse strain and ν_m is the Poisson's ratio of the matrix. When the particle is longer, larger areas in the matrix are **constrained** by the particle from contracting in the direction perpendicular to the loading direction. According to (6.6), such constraining in $|\varepsilon_{11}|$ in the matrix results in an increase in σ_{22} in the matrix and consequently an increase in the overall average σ_{22}.

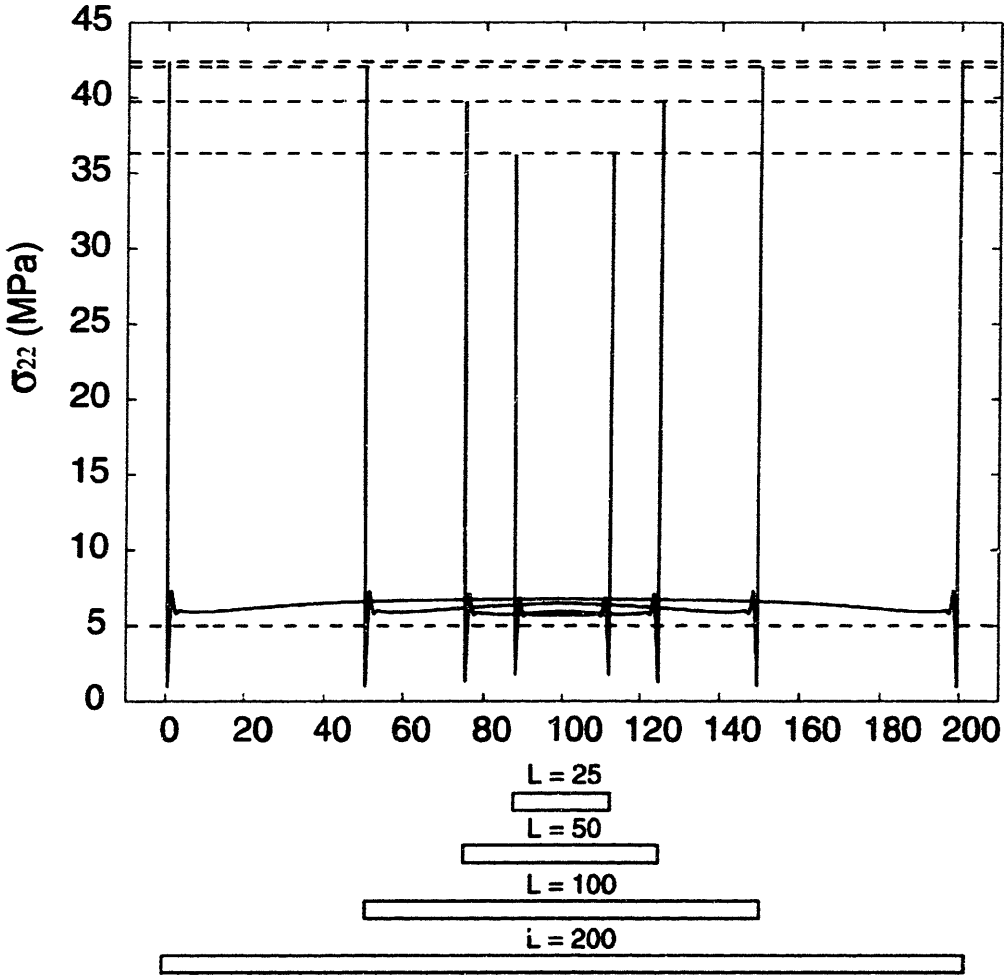

Figure 6.7 Distribution of σ_{22} in the particle under transverse tensile loading with particle aspect ratio 25, 50, 100, and 200.

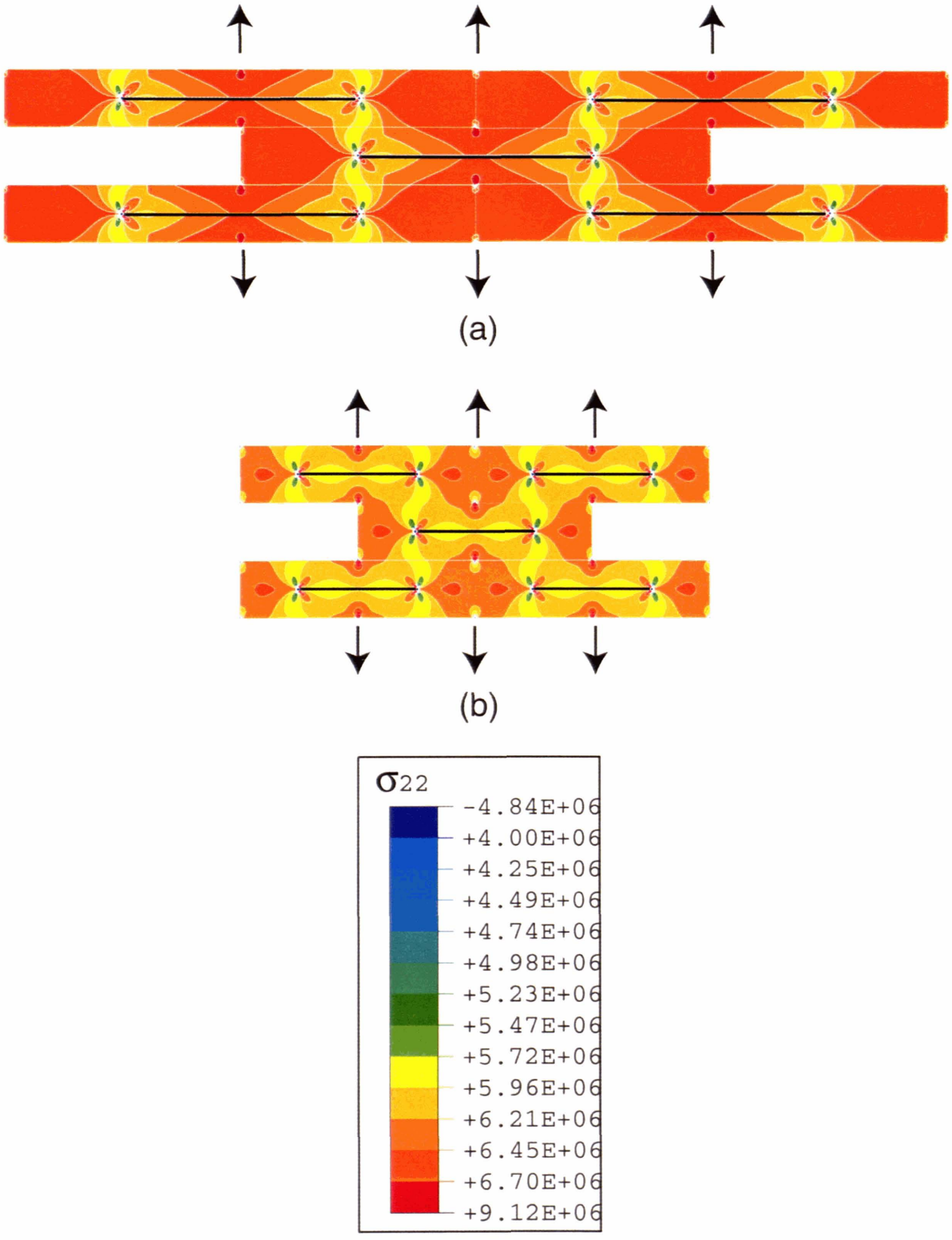

Figure 6.8 Contour of σ_{22} in the matrix under transverse tensile loading (macroscopic strain ε_{22} = 0.005): (a) $L \times t$ = 100×1, $a \times b$ = 50×25, f_p = 2%; (b) $L \times t$ = 50×1, $a \times b$ = 100×25, f_p = 2%.

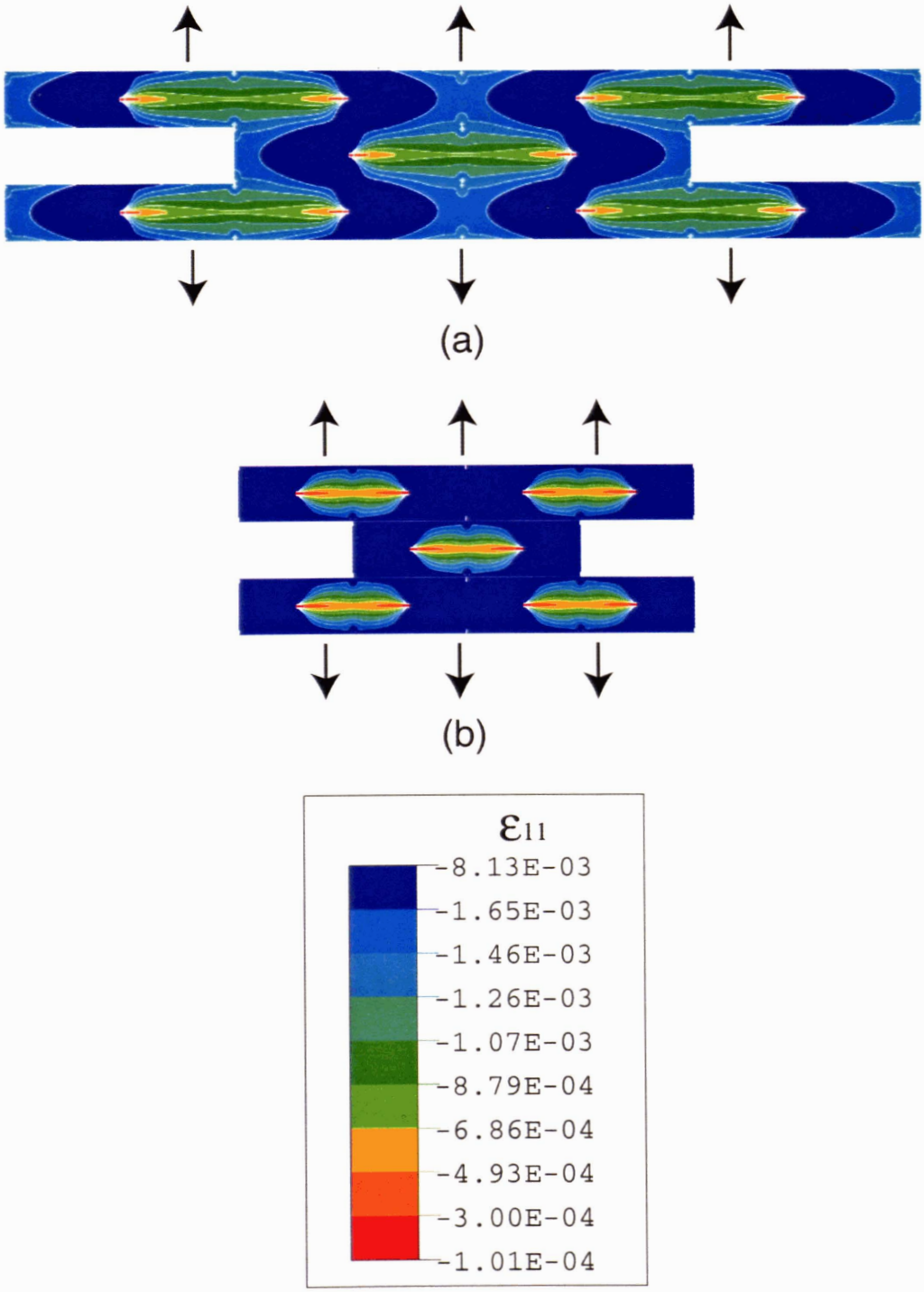

Figure 6.9 Contour of ε_{11} under transverse tensile loading (macroscopic strain ε_{22} = 0.005): (a) $L \times t = 100 \times 1$, $a \times b = 50 \times 25$, $f_p = 2\%$; (b) $L \times t = 50 \times 1$, $a \times b = 100 \times 25$, $f_p = 2\%$.

6.1.3. Comparison with theoretical predictions

The simulation results are compared with predictions of the Halpin-Tsai equations and the Mori-Tanaka models. Figure 6.10, 6.11, and 6.12 plot the results as function of particle volume fraction, particle aspect ratio, and particle/matrix stiffness ratio, respectively.

In general the Mori-Tanaka models overestimate E_{22} and Halpin-Tsai equations underestimate E_{22}. More specifically, the Mori-Tanaka model is able to predict similar influence of the various factors on E_{22} as is exhibited by simulation results; while the Halpin-Tsai equations are insensitive to particle aspect ratio.

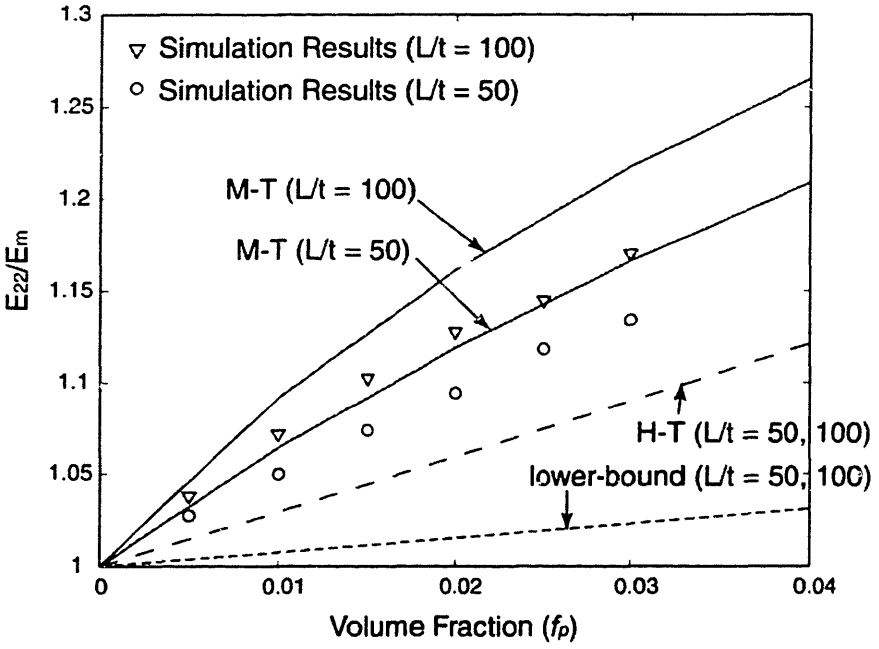

Figure 6.10 Comparison between simulation results and theoretical approaches (M-T denotes Mori-Tanaka, H-T denotes Halpin-Tsai): sensitivity to particle volume fraction and aspect ratio (E_f/E_m = 100, v_p = 0.2, v_m = 0.35).

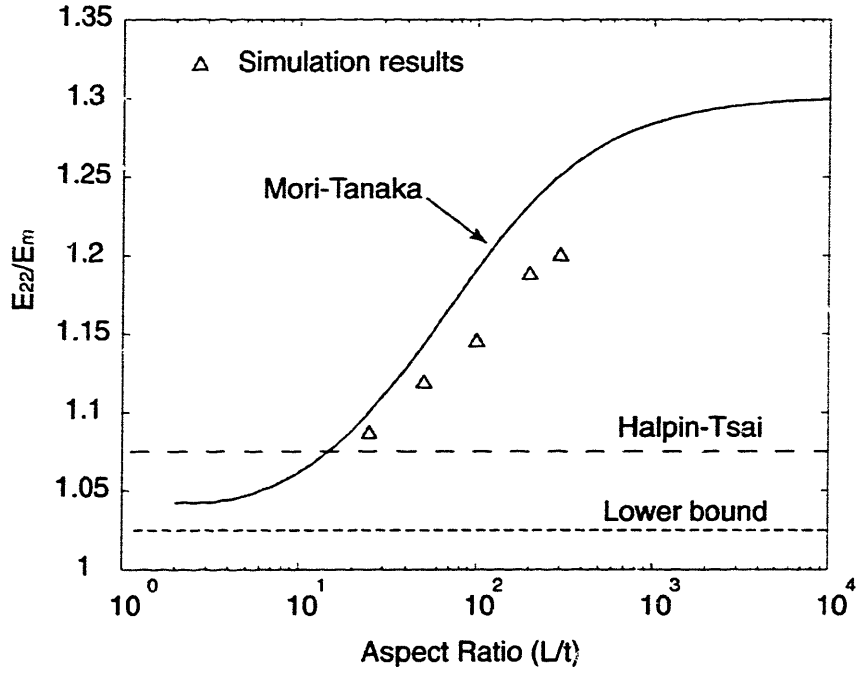

Figure 6.11 Comparison between simulation results and theoretical approaches: sensitivity to particle aspect ratio ($f_p = 2.5\%$, $E_p/E_m = 100$, $v_p = 0.2$, $v_m = 0.35$).

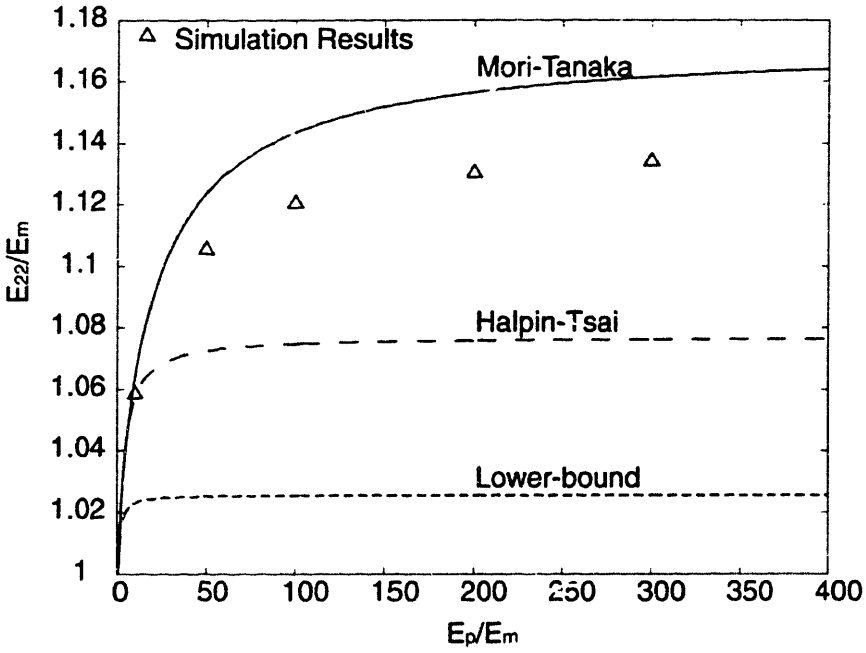

Figure 6.12 Comparison between simulation results and theoretical approaches: sensitivity to the ratio of particle/matrix stiffness ($f_p = 2.5\%$, $L/t = 50$, $v_p = 0.2$, $v_m = 0.35$).

6.2. Prediction of Effective Transverse Poisson's Ratio

In this section we will focus on the two Poisson ratios v_{12} and v_{21}. While v_{12} has the physical interpretation of the Poisson's ratio that characterize the transverse strain in the direction normal to the plane of isotropy resulting from stress in the plane of isotropy, v_{21} characterize the strain in the plane of isotropy resulting from stress normal to it. The relationship between them is given in (5.3).

Denote the Poisson's ratio of the matrix and the particle as v_m and v_p, v_p generally smaller than v_m. Since the particle's dimension is large in direction one and small in direction 2, it is reasonable to expect that v_{12} of the composite remains almost the same as v_m, while the effective v_{21} is reduced by the inclusion of the particles to a certain extent.

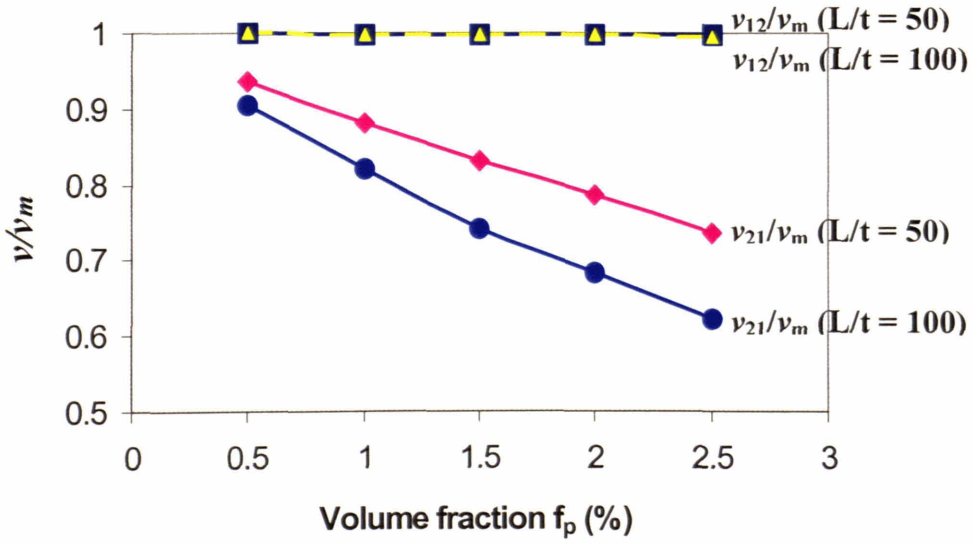

Figure 6.13 Dependence of v_{12} and v_{21} on particle content and particle aspect ratio

Figure 6.13 shows the normalized v_{12} and v_{21} as function of particle volume fraction and particle aspect ratio. As expected, the impact of the inclusion of nano-particles on v_{12} is

almost negligible; however, v_{21} exhibit a rather significant decrease with increase in particle content. Furthermore, this decrease in v_{21} is enhanced by increasing particle aspect ratio.

Comparison between simulation results and the predictions using Halpin-Tsai equations and Mori-Tanaka models is shown in Figure 6.14. Both models are able to reflect the influence of particle aspect ratio and to capture the nonlinear dependence of v_{21} on the particle content. The predictions of Mori-Tanaka models are in good agreement with the simulation results at small volume fraction; however, predictions from both models deviate from the simulation results at larger f_p, with underestimation of the impact of the inclusions by Mori-Tanaka and overestimation of it by Halpin-Tsai.

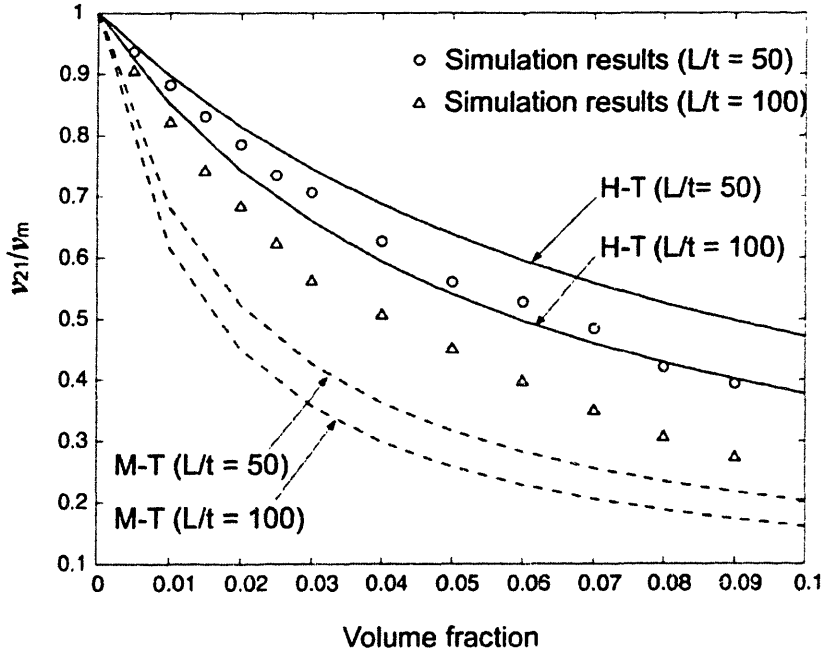

Figure 6.14 Comparison between simulation results and predictions of composite theories with H-T denoting Halpin-Tsai and M-T denoting Mori-Tanaka

6.3. Prediction of Effective Transverse Shear Modulus

At Low filler loading, the improvement of G_{12} over the shear modulus of the homopolymer, G_m, is very small. For the completeness of our study on the anisotropic elastic properties of polymer/clay nanocomposite, we include the prediction of G_{12} as well.

Figure 6.16 shows the dependence of G_{12} on particle volume fraction and aspect ratio. While the clay content is small (less than 6%), the increase in G_{12} over G_m is less than 10%. Although larger particle aspect ratio tends to result in slightly smaller G_{12}, the influence of L/t is almost negligible.

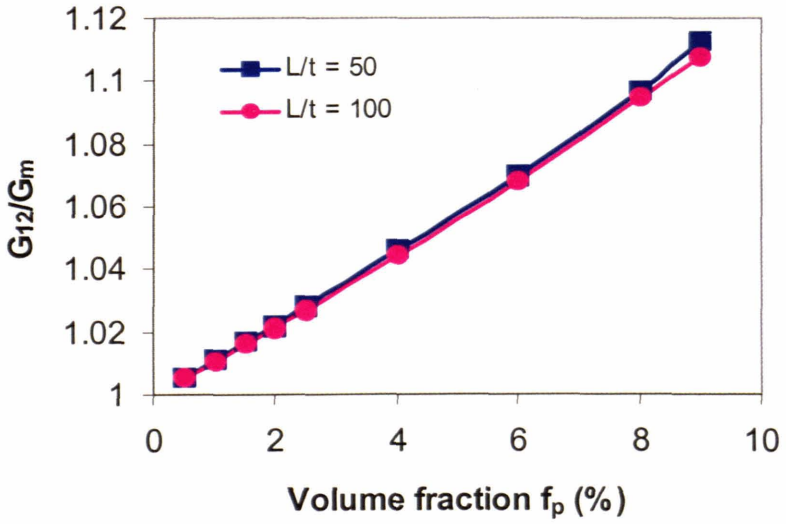

Figure 6.15 Dependence of G_{12} on particle volume fraction and particle aspect ratio ($G_p/G_m = 112.5$).

The simulation results are compared with the predictions using the Halpin-Tsai equations and the Mori-Tanaka models, as shown in Figure 6.16. While the Halpin-Tsai equation

overestimate G_{12}, the Mori-Tanaka model gives predictions in good accordance with the simulation results.

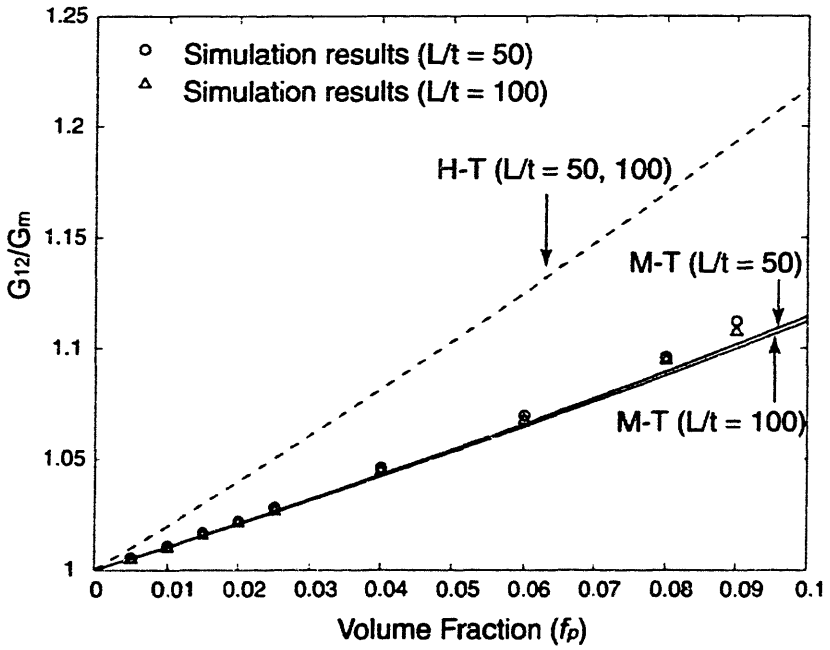

Figure 6.16 Comparison between simulation results and predictions of composite theories with H-T denoting Halpin-Tsai and M-T denoting Mori-Tanaka (G_p/G_m = 112.5).

Chapter 7

Conclusions and Future Work

Micromechanical models of various representative volume elements (RVEs) of the underlying structure of the polymer nano-clay composite are constructed. These models are characterized by clay volume fraction and micro/nano scale morphological features such as clay aspect ratio (length/thickness, L/t), clay distribution (random vs. regular patterns) and clay platelet orientation distribution. Anisotropic macroscopic moduli of these RVEs are predicted as a function of these geometrical parameters as well as material parameters through FEM simulations. The effective properties of the intercalated clay particle are estimated in terms of the internal clay structural parameters: the silicate layer properties, the interlayer spacing, and the number of layers. Results of micromechanics modeling based directly on the nanoscale clay structure are compared with theoretical predictions and tensile experimental data. Preliminary conclusions are summarized as the following:

- The predictions based on the simplified two-dimensional continuum models are rather consistent with experimental observations, suggesting that the composite level explanations may explain the stiffness enhancement mechanism of polymer nanocomposites to a large degree.
- The predicted macroscopic moduli of the nanocomposite are strongly influenced by each individual model parameters (clay aspect ratio, clay volume fraction, the mechanical properties of the clay and the matrix polymer). However, these

parameters are essentially correlated through the internal clay structure characterizing the morphology of the nanocomposite. Properties jumps accompany the morphological transition from intercalation to exfoliation.

- Studies of the local stress/strain fields show that the stiffness enhancement comes through the efficient load transfer mechanism in the high aspect ratio fillers and also through the strain shielding effect in the matrix.

Future work will include:

- Understanding of the inter-silicate gallery matter (composition and important properties);
- Modeling the clay particle as an anisotropic material;
- Understanding the clay/matrix polymer interface morphology and exploring its possible influence on the macroscopic mechanical properties;
- Expanding the model parameters to represent a wider range of morphology, including distribution of particle orientation and particle structure;
- Study thermal expansion properties of the nanocomposite;
- Generating fully three-dimensional models and studying inelastic material behavior under moderate/large strain.

Appendix A

Components of the Eshelby Tensor

The fourth-order Eshelby tensor $\boldsymbol{H}$ of spheroidal inclusion with three axes a, b and c (b = c) depends on the inclusion aspect ratio α (α = a/b = a/c) and the matrix elastic constants.

For a **fiber-like** spheroidal inclusion with its major axis a in direction 1 ($a > b = c$, $\alpha >$ 1), the non-zero components of $\boldsymbol{H}$ are given as

$$H_{1111} = \frac{1}{2(1-v_m)}\left\{1-2v_m+\frac{3\alpha^2-1}{\alpha^2-1}-\left[1-2v_m+\frac{3\alpha^2}{\alpha^2-1}\right]g\right\},$$

$$H_{2222} = H_{3333} = \frac{3}{8(1-v_m)}\frac{\alpha^2}{(\alpha^2-1)}+\frac{1}{4(1-v_m)}\left[1-2v_m-\frac{9}{4(\alpha^2-1)}\right]g,$$

$$H_{2233} = H_{3322} = \frac{1}{4(1-v_m)}\left\{\frac{\alpha^2}{2(\alpha^2-1)}-\left[1-2v_m+\frac{3}{4(\alpha^2-1)}\right]g\right\},$$

$$H_{2211} = H_{3311} = -\frac{1}{2(1-v_m)}\frac{\alpha^2}{(\alpha^2-1)}+\frac{1}{4(1-v_m)}\left\{\frac{3\alpha^2}{\alpha^2-1}-(1-2v_m)\right\}g,$$

$$H_{1122} = H_{1133} = -\frac{1}{2(1-v_m)}\left[1-2v_m+\frac{1}{\alpha^2-1}\right]+\frac{1}{2(1-v_m)}\left[1-2v_m+\frac{3}{2(\alpha^2-1)}\right]g,$$

$$H_{2323} = H_{3232} = \frac{1}{4(1-v_m)}\left\{\frac{\alpha^2}{2(\alpha^2-1)}+\left[1-2v_m-\frac{3}{4(\alpha^2-1)}\right]g\right\},$$

$$H_{1212} = H_{1313} = \frac{1}{4(1-v_m)}\left\{1-2v_m-\frac{\alpha^2+1}{\alpha^2-1}-\frac{1}{2}\left[1-2v_m-\frac{3(\alpha^2+1)}{\alpha^2-1}\right]g\right\},$$

where v_m is Poisson's ratio of the matrix, and g is calculated by

$$g = \frac{\alpha}{(\alpha^2 - 1)^{3/2}} \left\{ \alpha (\alpha^2 - 1)^{1/2} - \cosh^{-1} \alpha \right\}.$$

If the inclusion is a **disc-like** spheroid with its minor axis in direction 1 ($a < b = c$, $\alpha <$ 1), the expressions of H_{ijkl} are similar to those for the case of a fiber-like inclusion, with g replaced by g':

$$g' = \frac{\alpha}{(1 - \alpha^2)^{3/2}} \left\{ \cos^{-1} \alpha - \alpha (1 - \alpha^2)^{1/2} \right\}.$$

For a **spherical** inclusion ($\alpha = 1$), the expressions of H_{ijkl} are reduced to:

$$H_{1111} = H_{2222} = H_{3333} = \frac{7 - 5v_m}{15(1 - v_m)},$$

$$H_{1122} = H_{2233} = H_{3311} = \frac{5v_m - 1}{15(1 - v_m)},$$

$$H_{1212} = H_{2323} = H_{3131} = \frac{4 - 5v_m}{15(1 - v_m)}.$$

Appendix B

Calculation of Effective Elastic Moduli for Transversely Isotropic Materials Using Dilute Eshelby Model

The general approach to obtain the effective stiffness of a composite with axially aligned ellipsoidal inclusions at dilute concentration is summarized in Section 1.2.2. The fourth-order stiffness tensor $\boldsymbol{C}$ is written in terms of matrix and particle stiffness, matrix compliance, particle volume fraction, and the Eshelby tensor, which depends only on the particle aspect ratio and dimensionless matrix elastic constants (Eq. 1.18). Russel (1973) gave analytical predictions of the five independent elastic moduli (longitudinal Young's modulus, longitudinal Poisson's ratio, plane strain bulk modulus, longitudinal shear modulus and transverse shear modulus) for transversely isotropic materials by solving boundary value problems using the dilute Eshelby model.

The three boundary value problems considered necessary to determine the elastic moduli are: radially symmetric triaxial strain, transverse shear, and longitudinal shear.

- **Boundary conditions set by Russel to determine each of the elastic modulus**

1. Longitudinal Young's modulus E_{11}

$$\bar{\sigma}_{11} \neq 0, \bar{\sigma}_{22} = \bar{\sigma}_{33} = 0$$

$$E_{11} = \frac{\bar{\sigma}_{11}}{\bar{\varepsilon}_{11}}$$

2. Poisson's ratio v_{12}

$$\bar{\sigma}_{11} \neq 0, \bar{\sigma}_{22} = \bar{\sigma}_{33} = 0$$

$$v_{12} = v_{13} = -\frac{\bar{\varepsilon}_{22}}{\bar{\varepsilon}_{11}} = -\frac{\bar{\varepsilon}_{33}}{\bar{\varepsilon}_{11}}$$

3. Plane strain bulk modulus k'

$$\varepsilon_{11} = 0, \varepsilon_{22} = \varepsilon_{33} \neq 0$$

$$k' = \frac{\bar{\sigma}_{22}}{2\bar{\varepsilon}_{22}} = \frac{\bar{\sigma}_{33}}{2\bar{\varepsilon}_{33}}$$

4. Transverse shear modulus G_{23}

$$\bar{\varepsilon}_{23} = \bar{\varepsilon}_{32} \neq 0$$

$$G_{23} = \frac{1}{2}\frac{\bar{\sigma}_{23}}{\bar{\varepsilon}_{23}}$$

5. Longitudinal shear modulus G_{12}

$$\bar{\varepsilon}_{13} = \bar{\varepsilon}_{12} \neq 0$$

$$G_{12} = \frac{1}{2}\frac{\bar{\sigma}_{12}}{\bar{\varepsilon}_{12}}$$

- **Russel's Analytical solutions of the five elastic constants**

$$E_{11} = E_m\left(1 + f_p\alpha_1\right) \quad with \quad \alpha_1 = -A_1 + 2v_m A_2 \tag{B.1}$$

$$v_{12} = v_m - f_p\alpha_2 \quad with \quad \alpha_2 = 2A_3 + v_m\left(A_1 - A_4\right) - 2v_m^2 A_2\Big) \tag{B.2}$$

$$k' = k'_m\left(1 - f_p\alpha_3\right) \quad with \quad k'_m = \frac{E_m}{2(1+v_m)(1-2v_m)}, \alpha_3 = A_4 + 2v_m A_2 \tag{B.3}$$

$$G_{23} = G_m\left(1 + f_p\alpha_4\right) \quad with \quad G_m = \frac{E_m}{2(1+v_m)}, \alpha_4 = \frac{\frac{\mu^p}{\mu^m} - 1}{1 + 2\left(\frac{\mu^p}{\mu^m} - 1\right)H_{2323}} \tag{B.4}$$

$$G_{12} = G_m\left(1 + f_p\alpha_5\right) \quad with \quad \alpha_5 = \frac{\frac{\mu^p}{\mu^m} - 1}{1 + 2\left(\frac{\mu^p}{\mu^m} - 1\right)H_{1212}} \tag{B.5}$$

where H_{ijkl} are components of the Eshelby's tensor given in Appendix A, and A_i are coefficients depending on matrix/particle elastic constants and the Eshelby's tensor,

$$A_1 = (b_{11}a_{22} - b_{12}a_{12})/D$$
$$A_2 = (b_{12}a_{22} - a_{12}b_{22})/(2D)$$
$$A_3 = (a_{11}b_{21} - b_{11}a_{21})/D$$
$$A_4 = (a_{11}b_{22} - a_{21}b_{12})/D$$
$$D = a_{11}a_{22} - a_{12}a_{21}$$

with a_{ij} and b_{ij} given as

$$a_{11} = \Delta\lambda H_{mm11} + 2\Delta\mu H_{1111} + \lambda_m + 2\mu_m;$$
$$a_{12} = 2\Delta\lambda H_{mm22} + 4\Delta\mu H_{1122} + 2\lambda_m;$$
$$a_{21} = \Delta\lambda H_{mm11} + 2\Delta\mu H_{2211} + \lambda_m;$$
$$a_{22} = 2\Delta\lambda H_{mm22} + 2\Delta\mu(H_{2222} + H_{2233}) + 2(\lambda + \mu);$$

$$\begin{bmatrix} b_{11} & b_{12} \\ b_{21} & b_{22} \end{bmatrix} = \begin{bmatrix} -\Delta\lambda - 2\Delta\mu & -2\Delta\lambda \\ -\Delta\lambda & -2\Delta\lambda - 2\Delta\mu \end{bmatrix};$$

$$\Delta\lambda = \lambda^p - \lambda^m, \quad \Delta\mu = \mu^p - \mu^m;$$

where λ and μ are the Lame constants.

- **Derivation of other elastic constants using Russel's results**

Eqs. (B.1) to (B.5) give the complete set of elastic constants for transversely isotropic materials. The other engineering constants, such as E_{22}, can be obtained from these given constants and expressed as a function of f_p in the following fashion

$$P = P_m\left(1 + f_p\alpha + o(f_p^2)\right), \tag{B.6}$$

where P is certain property of the composite, P_m is the corresponding property of the matrix, and α is a coefficient depending on the geometry of the inclusions as well as the matrix/particle properties.

The transverse Young's modulus E_{22}, a quantity of common interest, is derived in the form of (B.6)

$$\begin{aligned} &E_{22} = E_m\left(1 + f_p\alpha_6\right) \quad with \\ &\alpha_6 = v_m^2\alpha_1 + 2v_m\alpha_2 + \frac{1}{2}(3v_m - 1)\alpha_3 + \frac{1}{2}(1 + v_m + 2v_m^2)\alpha_4 \end{aligned} \tag{B.7}$$

where α_i (i = 1,..., 4) are coefficients given in (B.1) to (B.5).

The approach to obtain (B.7) is the following:

First rewrite the plane strain bulk modulus k'

$$k' = \frac{E_{22}}{2(1 - v_{23} - 2v_{12}v_{21})} \tag{B.8}$$

Replace v_{23} and v_{21} in (B.6) by ($E_{22}/2G_{23}$ –1) and ($v_{12}E_{22}/E_{11}$), respectively, we have

$$E_{22} = \frac{2}{1/2k' + 1/2G_{23} + 2v_{12}^2/E_{11}} \tag{B.9}$$

E_{22} can be solved from (B.9) by replacing E_{11}, v_{12}, k', and G_{23} with (B.1) ~ (B.4),

$$E_{22} = E_{22}(f_p) = \frac{B_1\left\{1 + \beta_1 f_p + o(f_p^2)\right\}}{B_2\left\{1 + \beta_2 f_p + o(f_p^2)\right\}}, \tag{B.10}$$

where

$$B_1 = \frac{E_m^3}{(1+v_m)^2(1-2v_m)}$$

$$B_2 = \frac{E_m^2}{(1+v_m)^2(1-2v_m)}$$

$$\beta_1 = \alpha_4 - \alpha_1 - \alpha_3$$

$$\beta_2 = (-1+v_m^2)\alpha_1 - 2v_m\alpha_2 - (1/2)(1+3v_m)\alpha_3 + (1/2)(1-v_m-2v_m^2)\alpha_4$$

Eq. (B.7) is nothing but the Taylor series of (B.10) expanded about $f_p = 0$,

$$\begin{aligned} E_{22} &= \frac{B_1}{B_2}\left\{1+\beta_1 f_p + o(f_p^2)\right\}\left\{1-\beta_2 f_p + o(f_p^2)\right\} \\ &= E_m\left\{1+(\beta_1-\beta_2)f_p + o(f_p^2)\right\} \end{aligned} \qquad \text{(B.11)}$$

Define $\alpha_6 \equiv (\beta_1 - \beta_2)$ and omit $o(f_p^2)$ for $f_p << 1$; we then have

$$E_{22} = E_m\left(1+f_p\alpha_6\right),$$

which is exactly (B.7).

Appendix C

Comparison between effective stiffness predicted by Dilute Eshelby model and Mori-Tanaka model

The dilute Eshelby model applies only to low filler concentration. To find the applicable range of this model, we consider a composite with axially aligned disc-like spheroidal inclusions, with their minor axes aligned along 1-direction, as illustrated in Figure C.1. Predictions of the effective Young's modulus E_{22} ($E_{22} = E_{33} > E_{11}$) of such a material using the dilute model (analytical solution of E_{22} given in (B.7)) are compared with results predicted by the Mori-Tanaka model (analytical solution of E_{22} given in (1.21)).

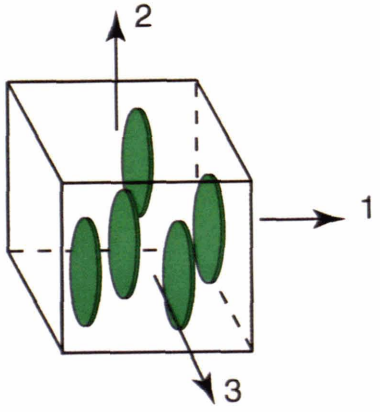

Figure C.1 Schematic of disc-like ellipsoidal inclusions axially aligned along 1-direction

Figures C.2, C.3 and C.4 plot the effective longitudinal stiffness as function of particle volume fraction, particle aspect ratio, and particle/matrix stiffness ratio, respectively. The following observations regarding the validity of the dilute Eshelby model are made:

- In general, for composite with high particle/matrix stiffness difference, the prediction from the dilute model is in good agreement with the Mori-Tanaka result at low volume fraction (up to f^*~1%); the discrepancy between them increases with increase of particle volume fraction (Figure C.2).
- The value of f^*, up to which the dilute model is applicable, is affected by particle aspect ratio; the larger L/t is, the smaller f^* is (Figure C.2, C.3).
- Even at a slightly higher volume fraction (~3%), the prediction of the dilute model is accurate enough provided that the difference between the particle and matrix stiffness is small (say, E_p/E_m<50) (Figure C.4).

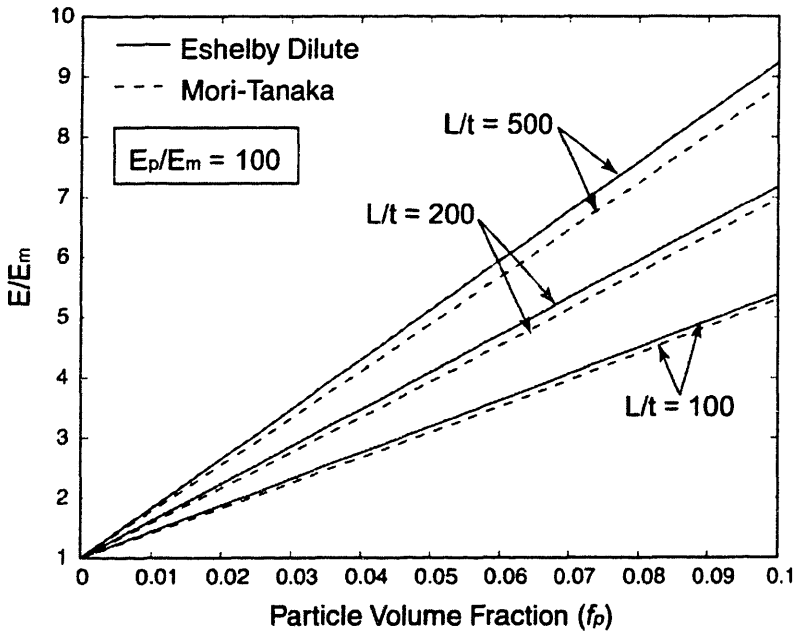

Figure C.2 Prediction of effective E_{22} ($E_{22} = E_{33} > E_{11}$) of disc-like ellipsoidal particles with aspect ratio L/t = 500, 200 and 100 (E_p/E_m = 100, v_m = 0.35, v_p = 0.20)

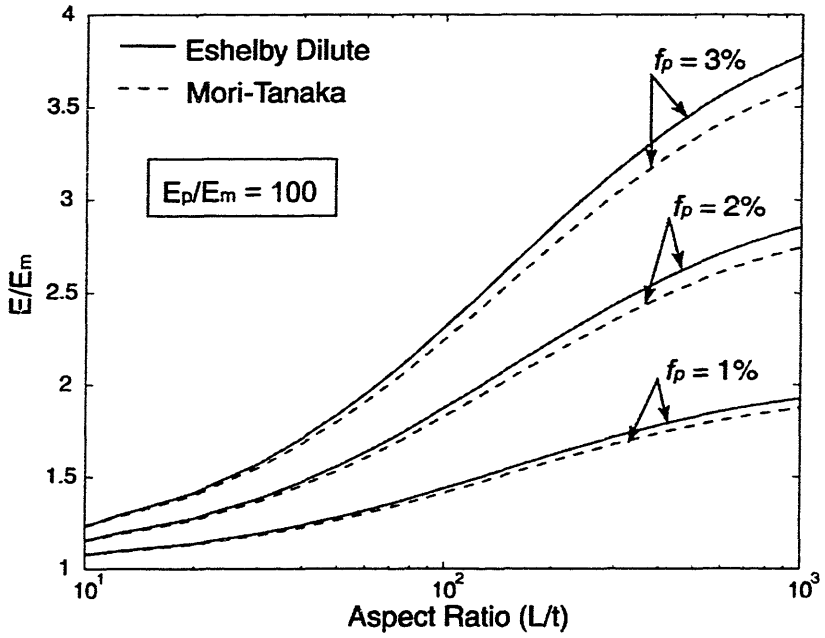

Figure C.3 Prediction of effective E_{22} ($E_{22} = E_{33} > E_{11}$) of disc-like ellipsoidal particles with particle volume fraction f = 3%, 2% and 1% ($E_p/E_m = 100$, $v_m = 0.35$, $v_p = 0.20$)

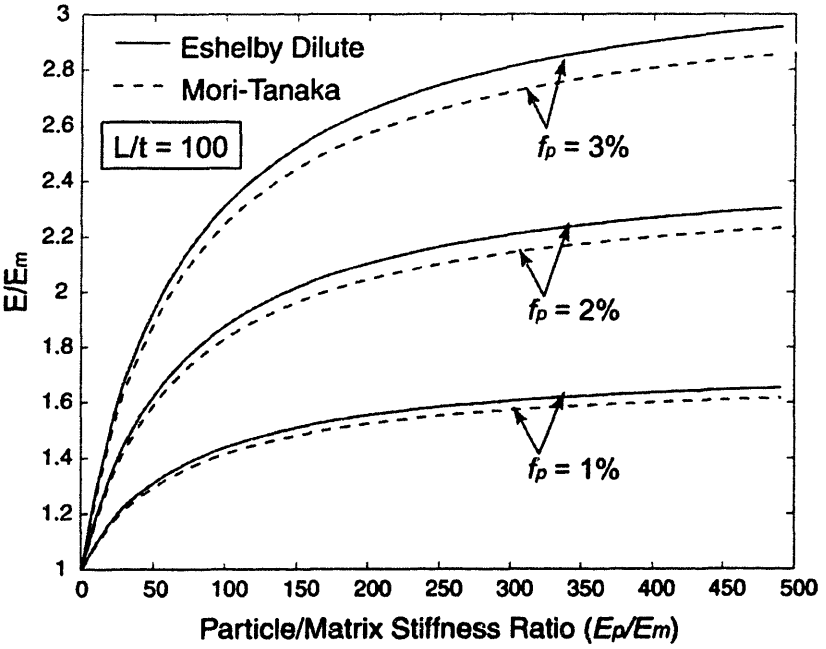

Figure C.4 Prediction of effective E_{22} ($E_{22} = E_{33} > E_{11}$) of disc-like ellipsoidal particles with particle volume fraction f = 3%, 2% and 1% ($L/t = 100$, $v_m = 0.35$, $v_p = 0.20$)

A composite with spherical inclusions is examined as well. Predictions of the effective stiffness of such composite using the dilute model and the Mori-Tanaka model are compared in Figure C.5. In general, for spherical inclusions, the dilute model is applicable for a wider range (up to $f^* \sim 3\%$); again, smaller E_p/E_m helps to increase the value of f^*.

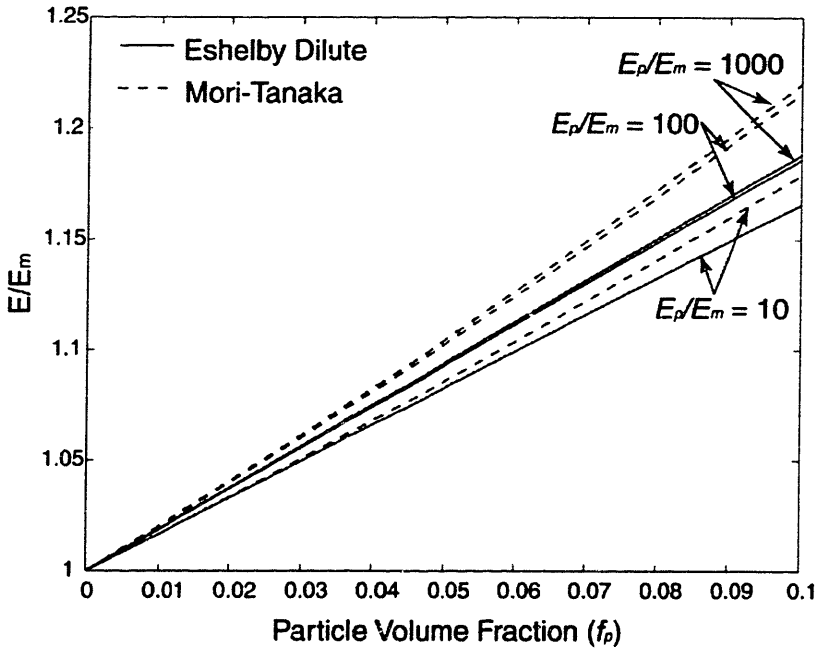

Figure C.5 Dependence of E on f_p for a composite of spherical inclusions with varying particle/matrix stiffness ratio E_p/E_m ($\nu_m = 0.35$, $\nu_p = 0.20$).

Appendix D

Plane Strain Moduli of Transversely Isotropic Material

The plane strain moduli obtained through applying appropriate loading conditions to a RVE under plane strain constraint are generally different from the actual moduli. The relationship between them is derived in the following for transversely isotropic/isotropic materials.

- **Constitutive relations**

The generalized Hooke's law for an orthotropic material is written as

$$\begin{Bmatrix} \sigma_{11} \\ \sigma_{22} \\ \sigma_{33} \\ \tau_{23} \\ \tau_{31} \\ \tau_{12} \end{Bmatrix} = \begin{bmatrix} C_{11} & C_{12} & C_{13} & 0 & 0 & 0 \\ C_{12} & C_{22} & C_{23} & 0 & 0 & 0 \\ C_{13} & C_{23} & C_{33} & 0 & 0 & 0 \\ 0 & 0 & 0 & C_{44} & 0 & 0 \\ 0 & 0 & 0 & 0 & C_{55} & 0 \\ 0 & 0 & 0 & 0 & 0 & C_{66} \end{bmatrix} \begin{Bmatrix} \varepsilon_{11} \\ \varepsilon_{22} \\ \varepsilon_{33} \\ \gamma_{23} \\ \gamma_{31} \\ \gamma_{12} \end{Bmatrix}, \tag{D.1}$$

where the engineering strain components are defined as

$$\begin{aligned} &\varepsilon_{11} = \frac{\partial u_1}{\partial X_1}, \quad \varepsilon_{22} = \frac{\partial u_2}{\partial X_2}, \quad \varepsilon_{11} = \frac{\partial u_3}{\partial X_3} \\ &\gamma_{23} = \frac{\partial u_2}{\partial X_3} + \frac{\partial u_3}{\partial X_2}, \quad \gamma_{31} = \frac{\partial u_3}{\partial X_1} + \frac{\partial u_1}{\partial X_3}, \quad \gamma_{12} = \frac{\partial u_1}{\partial X_2} + \frac{\partial u_2}{\partial X_1} \end{aligned} \tag{D.2}$$

The stiffness matrix, C_{ij}, for a transversely isotropic material with 1-3 plane as the isotropy plane can be expressed in terms of the engineering elastic constants

$$C_{11} = \frac{1 - v_{12}v_{21}}{E_1 E_2 \Delta}$$

$$C_{12} = \frac{v_{12}(1 + v_{13})}{E_1^2 \Delta}$$

$$C_{13} = \frac{v_{13} + v_{12}v_{21}}{E_1 E_2 \Delta}$$

$$C_{22} = \frac{1 - v_{13}^2}{E_1^2 \Delta} \quad , \tag{D.3}$$

$$C_{33} = \frac{v_{21}(1 + v_{13})}{E_1 E_2 \Delta}$$

$$C_{44} = C_{66} = G_{12}$$

$$C_{55} = G_{13}$$

where

$$\Delta = \frac{1 - 2v_{12}v_{21} - v_{13}^2 - 2v_{21}v_{12}v_{13}}{E_1^2 E_2}.$$

- **Stress components under plane strain condition**

Plane strain condition requires

$$\varepsilon_{33} = \gamma_{23} = \gamma_{31} = 0. \tag{D.4}$$

Taking (D.4) into (D.1), we have

$$\sigma_{11} = C_{11}\varepsilon_{11} + C_{12}\varepsilon_{22}; \tag{D.5}$$

$$\sigma_{22} = C_{12}\varepsilon_{11} + C_{22}\varepsilon_{22}; \tag{D.6}$$

$$\tau_{12} = C_{66}\gamma_{12}. \tag{D.7}$$

- **Plane strain longitudinal Young's modulus E_{11}^* and Poisson ratio v_{12}^***

Axial tension: $\sigma_{11} \neq 0, \quad \sigma_{22} = 0$.

With the axial stress boundary condition, we have

$$\sigma_{22} = C_{12}\varepsilon_{11} + C_{22}\varepsilon_{22} = 0 \quad \Rightarrow \varepsilon_{22} = -\frac{C_{12}}{C_{22}}\varepsilon_{11}. \tag{D.8}$$

Substitute ε_{22} in (D.5) with (D.8) to obtain:

$$\sigma_{11} = \left(C_{11} - \frac{C_{12}^2}{C_{22}} \right) \varepsilon_{11} . \tag{D.9}$$

The plane strain longitudinal Young's modulus and Poisson ratio can be obtained with (D.8), (D.9), and the expressions of C_{ij} given in (D.3)

$$E_{11}^* = \frac{\sigma_{11}}{\varepsilon_{11}} = C_{11} - \frac{C_{12}^2}{C_{22}} = \frac{E_{11}}{1 - \nu_{13}^2} ; \tag{D.10}$$

$$\nu_{12}^* = -\frac{\varepsilon_{22}}{\varepsilon_{11}} = \frac{C_{12}}{C_{22}} = \frac{\nu_{12}}{1 - \nu_{13}} . \tag{D.11}$$

If the material is isotropic, i.e., $E_{11} = E_{22} = E$, $\nu_{12} = \nu_{21} = \nu_{13} = \nu$, (D.10) and (D.11) can be further simplified as

$$E^* = \frac{E}{1 - \nu^2} ; \tag{D.12}$$

$$\nu^* = \frac{\nu}{1 - \nu} . \tag{D.13}$$

- **Plane strain transverse Young's modulus E_{22}^* and Poisson ratio ν_{21}^***

Axial tension: $\sigma_{22} \neq 0, \quad \sigma_{11} = 0$

With the axial stress boundary condition, we have

$$\sigma_{11} = C_{11}\varepsilon_{11} + C_{12}\varepsilon_{22} = 0 \quad \Rightarrow \varepsilon_{11} = -\frac{C_{12}}{C_{11}} \varepsilon_{22} . \tag{D.14}$$

Substitute ε_{11} in (D.6) with (D.14),

$$\sigma_{22} = \left(C_{22} - \frac{C_{12}^2}{C_{11}} \right) \varepsilon_{22} . \tag{D.15}$$

The plane strain longitudinal Young's modulus and Poisson ratio can be obtained with (D.14), (D.15), and the expressions of C_{ij} given in (D.3)

$$E_{22}^{*} = \frac{\sigma_{22}}{\varepsilon_{22}} = C_{22} - \frac{C_{12}^2}{C_{11}} = \frac{E_{22}}{1 - v_{12}v_{21}}; \tag{D.16}$$

$$v_{21}^{*} = -\frac{\varepsilon_{11}}{\varepsilon_{22}} = \frac{C_{12}}{C_{11}} = \frac{v_{21}(1 + v_{13})}{1 - v_{12}v_{21}}. \tag{D.17}$$

- **Longitudinal shear modulus**

Note that shear stress τ_{12} given in (D.7) is actually not affected by the fact that plane strain conditions (D.4) are imposed, thus G_{12}, calculated from $G_{12} = \tau_{12}/\gamma_{12}$, is the actual longitudinal shear modulus.

REFERENCES

Kojima, Y., Usuki, A., Kawasumi, M., Okada, A., Fukushima, Y., Kurauchi, T. and Kamigaito, O. (1993a) Synthesis of nylon 6-clay hybrid *J. Mater. Res.* **8**(5), 1179-1184.

Kojima, Y., Usuki, A., Kawasumi, M., Okada, A., Fukushima, Y., Kurauchi, T. and Kamigaito, O. (1993b) Mechanical properties of nylon 6-clay hybrid *J. Mater. Res.* **8**(5), 1185-1189.

Yano, K., Usuki, A., Okada, A., Kurauchi, T. and Kamigaito, O. (1993) Synthesis and properties of polymide clay hybrid *J. Polym. Sci., Part A, Polym. Chem.* **31**, 2493-2498

Messersmith, P. B. and Giannelis, E. P. (1994) Synthesis and characterization of layered silicate-epoxy nanocomposites *Chem. Mater.* **6**, 1719-1725

Messersmith, P. B. and Giannelis, E. P. (1995) Synthesis and barrier properties of poly(epsilon-caprolactone)-layered silicate nanocomposites *J. Polym. Sci., Part A, Polym. Chem.* **33**, 1047-1057

Gilman, J. W. (1999) Flammability and thermal stability studies of polymer layered-silicatre (clay) nanocomposites *Appl. Clay Sci.* **15**, 31-49

Vaia, R. A., Price. G., Ruth, P. N., Nguyen, H. T. and Lichtenhan, J. (1999) Polymer/layered silicate nanocomposites as high performance ablative materials *Appl. Clay Sci.* **15**, 67-92

Vaia, R. A. (2000) Structural characterization of polymer-layered silicate nanocomposites. *Polymer-clay nanocomposites* ed. Pinnavaia, T. J. and Beall, G. W., pp. 229-265.

Nam, P. H., Maiti, P., Okamoto, M., Kotaka, T., Hasegawa, N. and Usuki, A. (2001) A hierarchical structure and properties of intercalated polypropylene/clay nanocomposites. *Polymer* **42**, 9633-9640.

Kim, G. M., Lee, D. H., Hoffmann, B., Kressler, J., Stoppelmann, G. (2001) Influence of nanofillers on the deformation process in layered silicate/polyamide-12 nanocomposites. *Polymer* **42**, 1095-1100.

Kojima, Y., Usuki, A., Kawasumi, M., Okada, A., Kurauchi, T., Kamigaito, O. and Kaji, K. (1995) Novel preferred orientation in injection-molded nylon 6-clay hybrid. *J. Polym. Sci., Part B, Polym. Phys.* **33**, 1039-1045.

Tucker, C. L. and Liang, E. (1999) Stiffness predictions for unidirectional short-fiber composites: review and evaluation. *Compos. Sci. Technol.* **59**, 655-671.

Eshelby, J. D. (1957) The determination of the elastic field of an ellipsoidal inclusion and related problems. *Proc. Roy. Soc. A* **241**, 376-396.

Mori, T. and Tanaka, K. (1973) Average stress in matrix and average elastic energy of materials with misfitting inclusions. *Acta Metall.* **21**, 571-574.

Tandon, G. P. and Weng, G. J. (1984) The effect of aspect ratio of inclusions on the elastic properties of unidirectionally aligned composites. *Polym. Compos.* **5**, 327-333.

Ashton, J. E., Halpin, J. C. and Petit, P. H. (1969) Primer on composite materials: analysis. Technomic, Stamford, Conn.

Halpin, J. C. (1969) Stiffness and expansion estimates for oriented short fiber composites. *J. Compos. Mater.* **3**, 732-734.

Halpin, J. C. and Kardos, J. L. (1976) The Halpin-Tsai equations: a review. *Polym. Eng. Sci.* **16**, 344-352.

Russel, W. B. (1973) On the effective moduli of composite materials: effect o fiber length and geometry at dilute concentrations. *J. Appl. Math. Phys. (ZAMP)* **24**, 581-600.

Hill, R. (1964) Theory of mechanical properties of fiber-strengthened materials: I elastic behavior. *J. Mech. Phys. Solids* **12**, 199-212.

Hermans, J. J. (1967) The elastic properties of fiber reinforced materials when the fibers are aligned. *Proc. K. Ned. Akad. Wet., Ser. B* **65**, 1-9

Danielsson, M., Parks, D. M. and Boyce, M. C. (2002) Three-dimensional micromechanical modeling of voided polymeric materials. *J. Mech. Phys. Solids* **50**, 351-379.

Maine, F. W. and Shepherd, P. D. (1974) Mica reinforced plastics: a review. *Composites*, September, 193-200.

Fujiwara, S. and Sakamoto, T. (1976) Japanese Pat. JP-A-51-109998.